# Evaluation of Seismic Behavior of Coupling Beams with Various Types of Steel Fiber Reinforced Concrete

**Ángel L. Pérez-Irizarry**
**Gustavo J. Parra-Montesinos**

Department of Civil and Environmental Engineering
University of Wisconsin – Madison

A research project sponsored by the Charles Pankow Foundation, Bekaert Corporation, ACI Concrete Research Council, and the American Society of Concrete Contractors

December 2016

# Acknowledgements

The writers would like to acknowledge the financial support provided by the Charles Pankow Foundation, main sponsor of this research project, as well as that provided by Bekaert Corporation, ACI Concrete Research Council, and the American Society of Concrete Contractors. ArcelorMittal is also acknowledged for their donation of fibers used in some of the coupling beam specimens. The writers would also like to acknowledge Erico Corp. for their assistance with the procurement of materials for the construction of the test setup.

The writers would also like to thanks the support and suggestions provided by the project Industry Champion, Cary Kopczynski (Cary Kopczynski & Co.) and by members of the project Advisory Board, David Fields (Magnusson Klemencic Associates), Andrew Taylor (KPFF), Joe Ferzli (Cary Kopczynski & Co.), Chris Plue (Webcor), James K. Wight (University of Michigan), Russell Soeters (Conco Concrete Companies), and Mike Dolder (Mayes Testing Engineers). The useful comments provided by Rémy Lequesne (University of Kansas) and Luis Fargier-Gabaldón (Universidad de los Andes, Venezuela) are also greatly appreciated.

Special thanks are due to the staff of the Wisconsin Structures and Materials Testing Laboratory, namely William Lang and Jacob Zeuske, for their advice and guidance in the laboratory, as well as for their help in the instrumentation and testing of the specimens. The writers would like to also thank the students who were involved during the various stages of the project for their much-valued help, in particular Daniela Rincón-Morassutti, Vasily Dudnik, Peter Weatherer, and Le Pham.

## Table of Content


**1 INTRODUCTION ..... 1**

**2 EXPERIMENTAL PROGRAM ..... 4**

2.1 OVERVIEW ..... 4

2.2 COUPLING BEAM TEST SPECIMENS ..... 4

*2.2.1 Coupling Beam Reinforcement Design ..... 6*

*2.2.2 Mixing of FRC and Coupling Beam Specimen Construction ..... 10*

*2.2.3 Test Setup Description ..... 14*

*2.2.4 Instrumentation Used ..... 17*

*2.2.5 Test Protocol (Displacement History) ..... 20*

*2.2.6 Drift Calculation and Adjustment for End Block Rotations ..... 21*

*2.2.7 Calculation of Coupling Beam Shear Distortions ..... 21*

*2.2.8 Calculation of Coupling Beam Curvatures ..... 25*

2.3 FRC MATERIAL TESTING ..... 26

*2.3.1 Bending Tests (Notched Beam) ..... 27*

*2.3.2 Bending Tests (Un-notched Beams) ..... 28*

*2.3.3 Direct Tension Tests ..... 30*

*2.3.4 Compression Cylinder Tests ..... 33*

**3 MATERIAL TEST RESULTS ..... 35**

3.1 FLEXURAL TEST RESULTS OF FRC NOTCHED BEAMS ..... 35

3.2 FLEXURAL TEST RESULTS OF FRC UN-NOTCHED BEAMS ..... 46

3.3 FRC TENSILE TEST RESULTS ..... 57

3.4 RELATIONSHIP BETWEEN TENSILE AND FLEXURAL BEHAVIOR ..... 63

3.5 COMPRESSION CYLINDER TESTS ..... 65

3.6 STEEL REINFORCEMENT TENSILE TESTS ..... 67

**4 COUPLING BEAM TEST RESULTS ..... 71**

4.1 OVERALL BEHAVIOR ..... 71

*4.1.1 Coupling Beam Specimen CB1 ..... 72*

*4.1.2 Coupling Beam Specimen CB2 ..... 75*

*4.1.3 Coupling Beam Specimen CB3 ..... 77*

*4.1.4 Coupling Beam Specimen CB4 ..... 78*

*4.1.5 Coupling Beam Specimen CB5 ..... 81*

*4.1.6 Coupling Beam Specimen CB6 ..... 84*

*4.1.7 Coupling Beam Specimen CB7 ..... 86*

*4.1.8 Coupling Beam Specimen CB8 ..... 88*

4.2 ESTIMATION OF FLEXURAL STRENGTH ..... 90

4.3 ROTATIONS AND SHEAR DISTORTIONS IN PLASTIC HINGE REGION ..... 93

4.4 DRIFT COMPONENTS ANALYSIS ..... 96

4.5 REINFORCEMENT STRAINS ..... 102

*4.5.1 Transverse Reinforcement ..... 102*

*4.5.2 Longitudinal and Dowel Reinforcement ..... 105*

4.6 LINK BETWEEN MATERIAL PROPERTIES AND STRUCTURAL PERFORMANCE OF COUPLING BEAMS ..... 108

**5 SUMMARY AND CONCLUSIONS ..... 111**

5.1 SUMMARY ..... 111

5.2 CONCLUSIONS ..... 111

**6 REFERENCES ..... 114**

**7 APPENDIX A ..... 116**

# 1 Introduction

The behavior of coupled structural walls during strong earthquakes is greatly influenced by the strength, stiffness and energy dissipation capacity of coupling beams. Given their low span-to-depth ratio (typically less than 3) and expected high shear stress demand (often greater than $6\sqrt{f_c'}$ [psi], where $f'_c$ is the concrete compressive strength), the design and construction of these coupling beams have long represented a challenge to structural engineers and contractors.

Current design practice for coupling beams in regions of high seismicity is primarily based on results from research conducted in the late 1960s and early 1970s in New Zealand (Paulay 1971; Paulay and Binney, 1974; Paulay and Santhakumar, 1976). The design generally incudes the use of diagonal bars in sufficient amount such as to resist the entire design shear force. Further, transverse reinforcement similar to that used in potential plastic hinge regions of columns of special moment resisting frames is required to provide confinement either to the diagonal reinforcing bars or to the entire coupling beam core. As shown in Figure 1.1, this design is difficult to construct, given the intricate reinforcement detailing involved and the need to "thread" diagonal bars through heavily congested wall boundary regions.

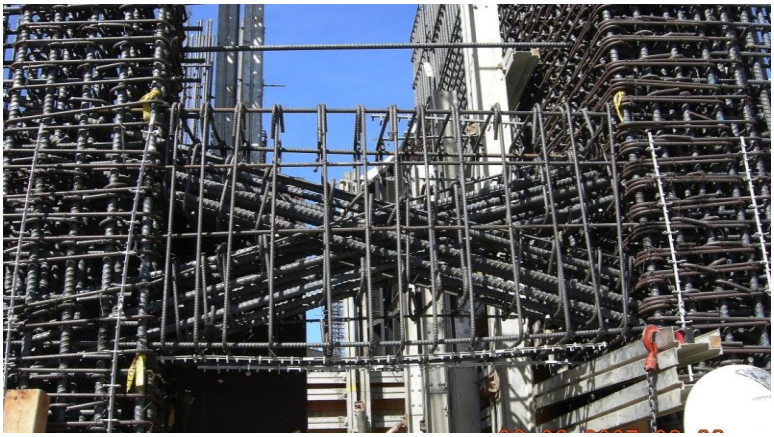

**Figure 1.1: Typical Reinforcement Detailing in a Diagonally Reinforced Coupling Beam (Courtesy of Rémy Lequesne)**

As an alternative to the reinforcement detailing discussed above, the use of fiber reinforcement has been extensively investigated in order to evaluate its potential to substantially simplify the

design of coupling beams (Canbolat, Parra-Montesinos and Wight, 2005; Lequesne, 2011; Setkit, 2012; Lequesne, Parra-Montesinos and Wight, 2013; Parra-Montesinos et al., 2014). As part of this effort, one design has been recommended for use in relatively slender coupling beams (span-to-depth ratios greater than or equal to 2.2). This design consists of the use of longitudinal and transverse reinforcement only (i.e., no diagonal bars), with column-type special confinement at the beam ends over a length half the beam depth from the wall faces. This reinforcement design, when used in combination with 1.2 in. long and 0.015 in. diameter hooked steel fibers with a nominal tensile strength of 330 ksi, has been shown to lead to drift capacities of at least 5.0% in coupling beams subjected to shear stress levels comparable to the maximum limit allowed in ACI 318-14 (ACI Committee 318, 2014) for diagonally reinforced coupling beams ($10\sqrt{f_c'}$ [psi]). The significant simplifications in reinforcement detailing achieved through the use of this fiber reinforced concrete has led to the recent implementation of this design in two high-rise building projects in the State of Washington (Parra-Montesinos et al., 2014; Kopczynski and Whiteley, 2016). Figure 1.2 shows the casting of a fiber reinforced concrete coupling beam in *The Martin* building in Seattle, WA.

**Figure 1.2: Casting of Fiber Reinforced Concrete Coupling Beam in *The Martin* Building, Seattle, WA**

The wide implementation of a fiber reinforced concrete coupling beam design in the United States and elsewhere requires, among other things, the specification of performance criteria for fiber reinforced concrete such that the design is not tied to the use of a particular type of fiber at a given amount. Ideally, structural designers and contractors should be able to specify material performance criteria that would "ensure" a minimum level of seismic performance (e.g., minimum drift capacity for a given expected shear stress) from the coupling beams. Towards this end, an experimental research program was conducted in order to evaluate the seismic performance of coupling beams constructed with various types of steel fibers and in different dosages.

Eight fiber reinforced concrete (FRC) coupling beams were tested under large displacement reversals. Also, four-point bending tests, direct tension tests and compression tests were conducted on the various FRCs investigated for evaluation of material performance. Based on the results from this research and those reported elsewhere (Parra-Montesinos et al., 2014), recommendations are given that tie material performance with coupling beam drift and expected shear stress demand so that a simplified reinforcement detailing can be used as an alternative to the current diagonally reinforced coupling beam design specified in the 2014 ACI Building Code (ACI Committee 318, 2014).

# 2 Experimental Program

## 2.1 Overview

Past experimental research (Setkit, 2012; Parra-Montesinos et al., 2014), showed that the use of tensile strain hardening fiber reinforced concrete (FRC) in coupling beams with span-to-depth ratio of 2.2 or greater allowed the elimination of diagonal reinforcement while ensuring adequate shear strength and drift capacity. Only a single strain-hardening FRC was investigated, however, which featured 1.18 in. long, 0.015 in. diameter hooked steel fibers with a tensile strength of 330 ksi at a 1.5% fiber volume fraction ($V_f$). There is therefore a need to evaluate the possibility of using lower fiber dosages or other fiber types, based on the expected coupling beam drift and shear stress demands.

The experimental study reported herein was aimed at 1) evaluating the performance under large displacement reversals of coupling beams without diagonal reinforcement constructed with various FRCs (fiber type and dosage); 2) evaluating the bending, tensile and compressive behavior of the various FRCs investigated; and 3) establishing a link between the mechanical properties of FRC and the structural performance of the FRC coupling beams.

## 2.2 Coupling Beam Test Specimens

Eight coupling beam specimens were tested under lateral displacement reversals. Each coupling beam specimen consisted of a precast, rectangular coupling beam connected to two large rectangular blocks that simulated the end regions of two walls being coupled. Main variables investigated were: 1) coupling beam span-to-depth ratio, $l_n/h$ (3.0 and 2.0), 2) peak shear stress demand ($6 - 12\sqrt{f'_c}$ [psi]), and 3) type of fiber reinforced concrete (i.e., fiber type and dosage).

The FRCs considered in this experimental work had, on average, a compressive strength of approximately 9000 psi (62 MPa). Three different fibers were evaluated, HE 55/35, RC 55/30 BG, and RC 80/30 BP fibers, with a nominal tensile strength of 174 ksi, 195 ksi and 330 ksi, respectively. HE 55/35 fibers were manufactured by ArcelorMittal and both RC 55/30 BG and

RC 80/30 BP fibers were manufactured by Bekaert Corporation. Figure 2.1 shows the geometry of the three fibers investigated.

Along with the casting of each coupling beam specimen, several material samples were cast from the same concrete batches to evaluate the flexural, tensile and compressive behavior of these FRCs. A total of six different FRCs were investigated depending on the beam span-to-depth ratio and expected shear stress demand, as shown in Table 2.1. In general, coupling beams constructed with the FRCs expected to show the best performance were designed for higher shear stress demands (approximately $8 - 12\sqrt{f'_c}$ [psi]). Coupling beams constructed with lower performing FRCs, on the other hand, were designed for shear stresses approximately $6 - 8\sqrt{f'_c}$ (psi). Also, materials expected to perform the best were used in the coupling beams with $l_n/h$ = 2.0 given the more important role played by shear in these beams compared to those with $l_n/h$ = 3.0.

**Table 2.1: FRC Used in Each Coupling Beam Specimen**

| Coupling Beam Specimen | $l_n/h$ | Fiber Type | $V_f$ | Target shear stress ($\sqrt{f'_c}$, psi) |
|---|---|---|---|---|
| CB1 | 3.0 | HE 55/35 | 1.25% | 12 |
| CB2 | 3.0 | HE 55/35 | 1.25% | 8-10 |
| CB3 | 3.0 | RC 55/30 BG | 1.25% | 8-10 |
| CB4 | 3.0 | RC 55/30 BG | 1.00% | 6-8 |
| CB5 | 3.0 | RC 80/30 BP | 1.00% | 6-8 |
| CB6 | 2.0 | HE 55/35 | 1.50% | 8-10 |
| CB7 | 2.0 | RC 80/30 BP | 1.50% | 8-10 |
| CB8 | 2.0 | RC 80/30 BP | 1.50% | 8-10 |

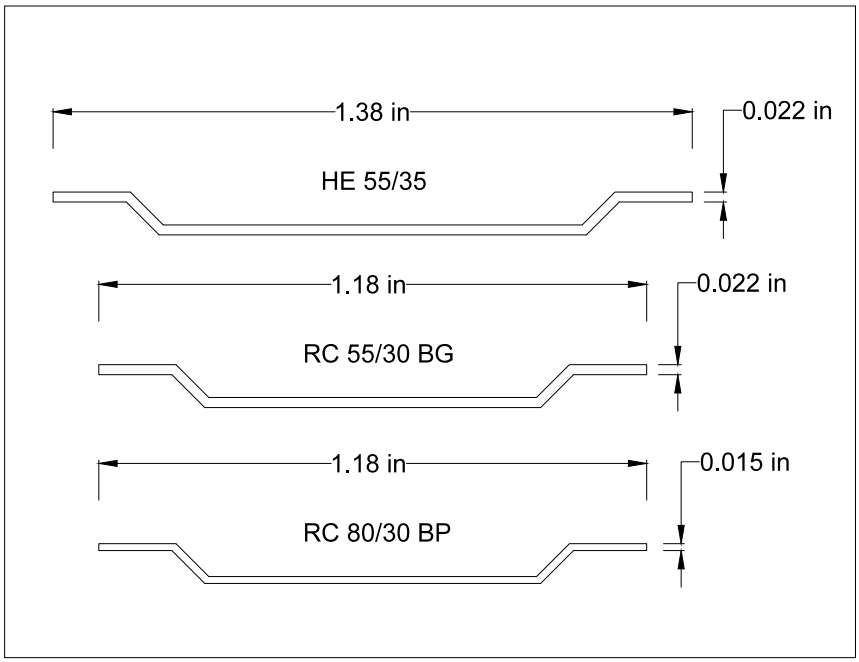


**Figure 2.1: Steel Fiber Reinforcement**

### 2.2.1 Coupling Beam Reinforcement Design

The coupling beam specimens investigated in this experimental work had a span-to-depth ratio ($l_n/h$) of either 2.0 or 3.0. ACI 318-14 provides two alternatives for the design of coupling beams with span-to depth ratios greater than or equal to 2.0 and less than 4.0. Coupling beams that fall in this range, $2.0 \leq l_n/h < 4.0$, can be designed either as beams of special moment resisting frames per Section 18.6 of ACI 318-14 or as diagonally reinforced coupling beams following ACI 318-14 Section 18.10.7.2. The coupling beam specimens of this experimental work were not designed following either of the two alternatives in ACI 318-14.

Because of the enhanced ductility, shear strength and confinement capability exhibited by FRCs, as well as results from previous investigations (Setkit, 2012; Parra-Montesinos et al., 2014), a simplified reinforcement detailing without any diagonal reinforcement was used in all coupling beam specimens. The first step in the design process consisted of selecting the target shear demand, $V_u$. Based on the selected shear demand, the moment demand, $M_u$, was calculated as $M_u = (V_u\, l_n)/2$, where $l_n$ is the clear span length of the coupling beam.

The shear strength of the coupling beams was assumed to be the result of contributions from the FRC, referred to herein as $V_c$, and the transverse steel, $V_s$, (truss mechanism). Results from previous research on coupling beams constructed using a tensile strain-hardening FRC suggest a shear stress of $5\sqrt{f'_c}$ (psi) as an upper limit for the FRC contribution to the overall shear capacity of the coupling beams (Lequesne, 2011). The coupling beams tested in this study, except for one case, were designed so that the shear "demand" on the FRC would not exceed this limit. Calculated $V_c$ demands for each test specimen based on the peak applied shear and measured yield strength of the transverse steel are discussed in Section 4.5.1.

For each specimen, two different transverse steel designs were provided, one for the plastic hinge regions, and the other for the region outside of the plastic hinges. For design purposes, and based on previous work (Lequesne et. al, 2013), the plastic hinge regions were assumed to extend half the overall beam depth from each end. The spacing $s$ of the transverse steel outside the plastic hinge regions, selected to consist of single #3 hoops, was determined so that,

$$s \leq \frac{A_v\, f_{yt}\, d}{V_s} \tag{1}$$

where $A_v$ is the area of one transverse steel hoop (0.22 in.$^2$), $f_{yt}$ is the yield strength of the transverse steel (taken as 60 ksi for design purposes), and $d$ is effective depth of the coupling beam. For simplicity, a single value of $d$ of 15.5 in. was used, which corresponded to approximately 85% of the overall beam depth.

The transverse reinforcement in the plastic hinge regions was detailed following, as practicably as possible, the provisions for columns of special moment resisting frames of Chapter 18 of the ACI 318-14, particularly the provisions shown in the Table 18.7.5.4. This was done to provide large confinement in the plastic hinge regions, given the combination of large inelastic rotation and shear stress reversals. The provisions of Table 18.7.5.4 resulted in a 1.8 in. spacing for double hoops made of #4 bars. Because of the constructability issues that would be created by such a small spacing, the spacing of #4 hoops was selected to be 2.5 in. This spacing satisfied the confinement provisions only in the direction parallel to the width of the coupling beams. This detailing, however, was deemed appropriate considering that the fiber reinforcement would also contribute to the confinement of the concrete core.

Once the transverse reinforcement design was completed, the longitudinal reinforcement was selected such that the expected flexural capacity of the coupling beam would be approximately equal to the previously calculated moment $M_u$. The coupling beams were therefore expected to exhibit a flexurally-dominated behavior. Because no fibers would cross the cold joint corresponding to the wall-to-coupling beam interface, U-shaped bars or dowels (two sets at each end) were provided to strengthen this section, prevent concentration of inelastic deformations and thus, a premature sliding shear failure. The extension of the legs of the dowels into the end blocks was sufficient to ensure full development of these bars. The extension into the coupling beam measured from the wall faces, on the other hand, varied depending on the specimen, being 14 bar diameters for Specimen CB1 and 9 bar diameters for Specimens CB2 through CB5 with $l_n/h = 3.0$, and 6 bar diameters for Specimen CB6 through CB8 with $l_n/h = 2.0$. It was expected that the bends and improved bond conditions provided by the FRC material would allow the development of these bars over such short lengths.

Two critical sections were considered for flexure, the wall-to-coupling beam interface and the section adjacent to the termination of intermediate dowel reinforcement. The moment capacity was taken as the maximum probable moment obtained from moment-curvature analyses assuming an axial force equal to 40% of the target shear demand, based on experimental observations by Lequesne (2011), and following the material model recommendations in Setkit (2012) for the higher performing FRCs. Figure 2.2 through Figure 2.6 show the reinforcement detailing used for each of the coupling beam specimens.

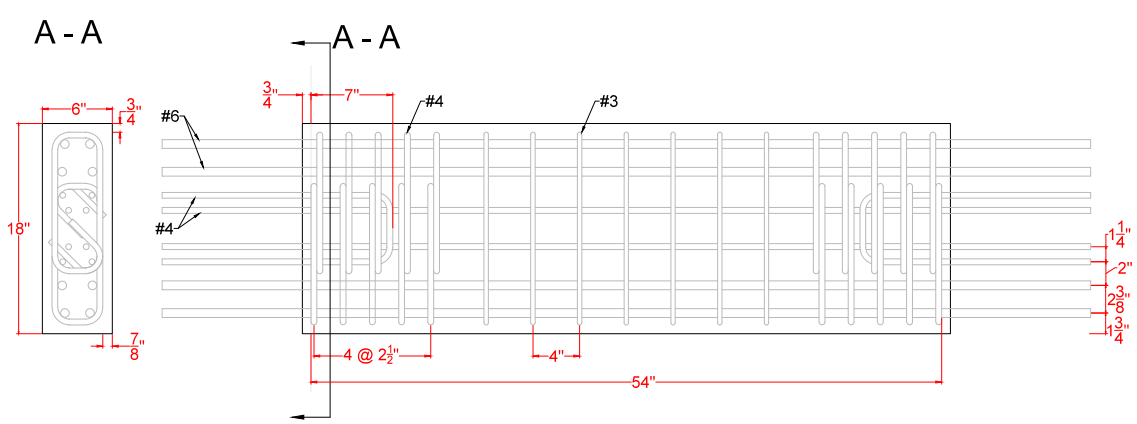


**Figure 2.2: Reinforcement Detailing of Coupling Beam CB1**

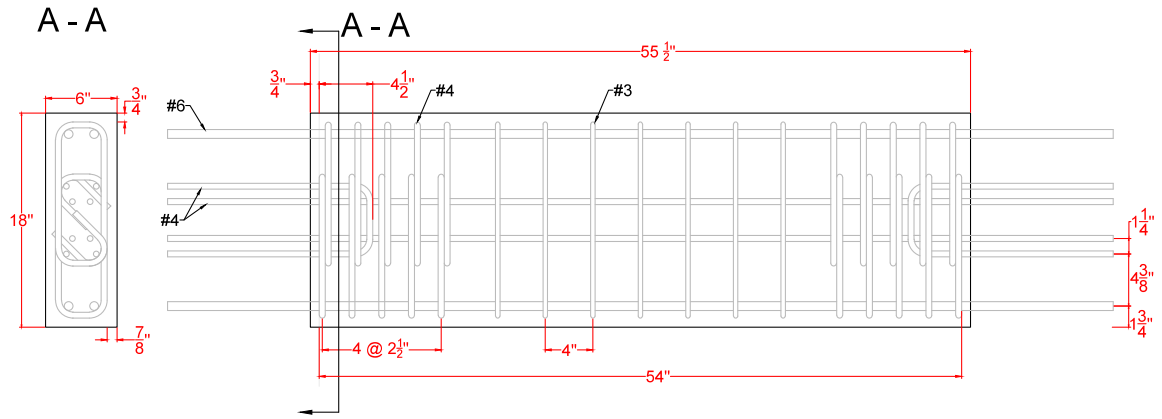


**Figure 2.3: Reinforcement Detailing of Coupling Beams CB2 and CB3**

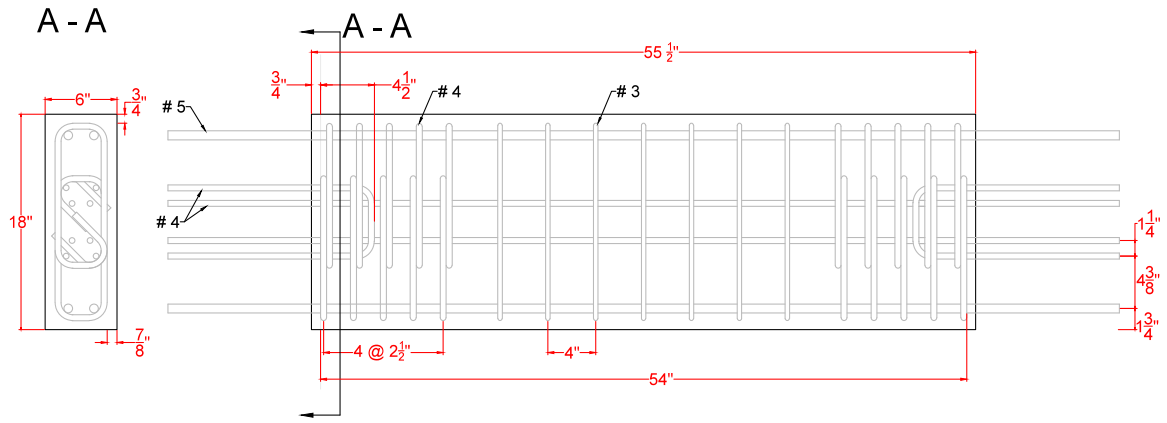


**Figure 2.4: Reinforcement Detailing of Coupling Beams CB4 and CB5**

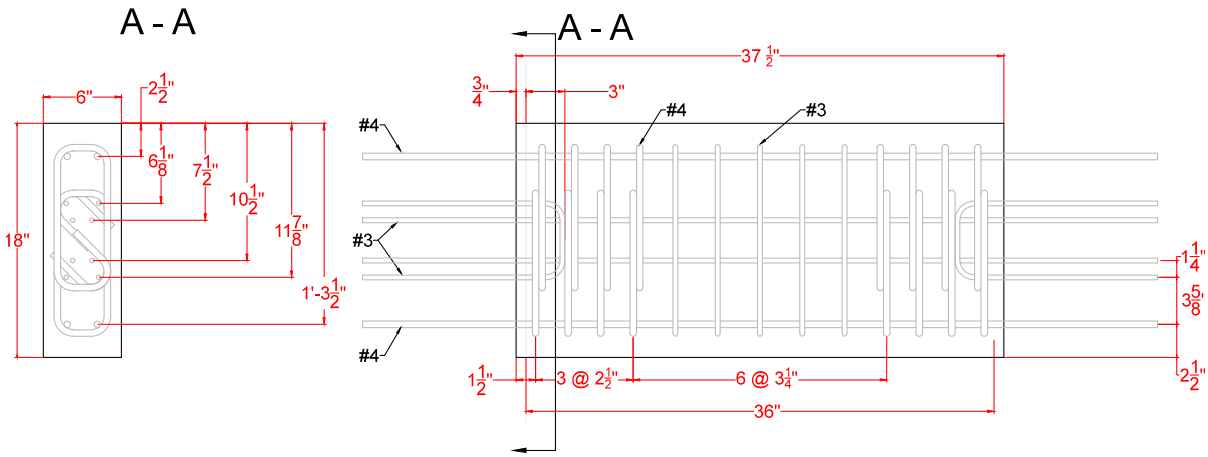


**Figure 2.5: Reinforcement Detailing of Coupling Beam CB6**

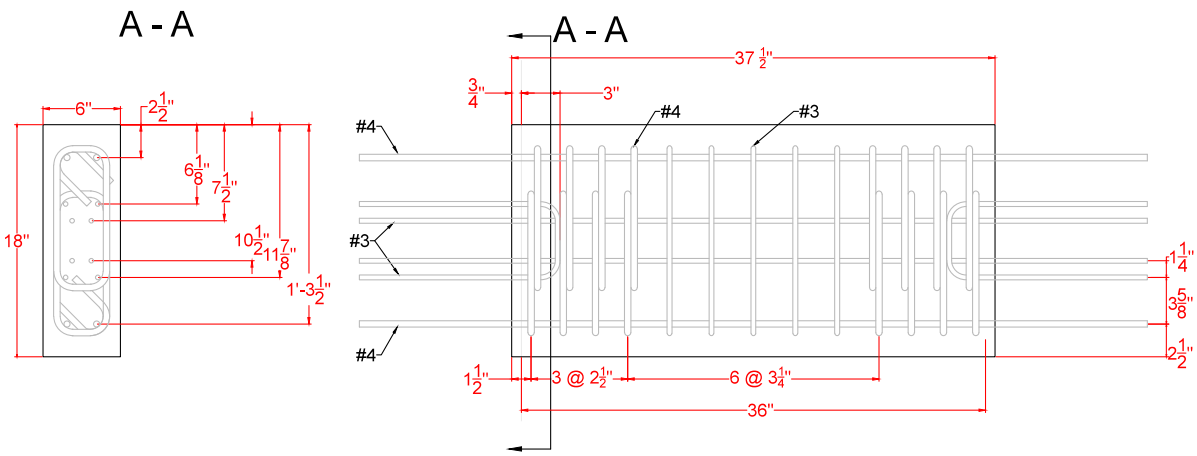


**Figure 2.6: Reinforcement Detailing of Coupling Beams CB7 and CB8**

As mentioned above, each coupling beam specimen was connected to two large blocks aimed at simulating the boundary regions of the walls being coupled. These end blocks were designed for the forces associated with a coupling beam shear of 150 kips, which is significantly larger than the maximum expected shear in any of the test coupling beams. Figure 2.7 shows a detailed drawing of the assembled reinforcement and a typical cross section of both end blocks. PVC pipes, used to insert through-bolts for connection to the strong floor or other test setup fixtures, are omitted from the drawings for clarity.

All of the steel reinforcement used in this project was cut and bent to specifications by a local supplier.

### 2.2.2 Mixing of FRC and Coupling Beam Specimen Construction

All of the FRCs used in the coupling beam specimens and material test samples were mixed and batched in the Wisconsin Structures and Materials Testing Laboratory (WSMTL). The materials needed for the FRCs were procured from local suppliers with the exception of the steel fibers. The FRCs studied in this project followed very similar proportions to one of the strain-hardening FRC mixtures that were previously investigated for coupling beam applications (Setkit, 2012). The main exception was that no viscosity modifying agents or super plasticizers were used for the mixtures investigated in this study. All the FRC mixtures used Portland cement Type I, and the coarse aggregate consisted of 3/8 in. maximum size crushed limestone. The sand

used was washed gravel sand known as Torpedo Sand, which is typically graded from mesh #200 to 3/16 in. Table 2.2 presents the target mixture proportions for the FRCs used in this project.

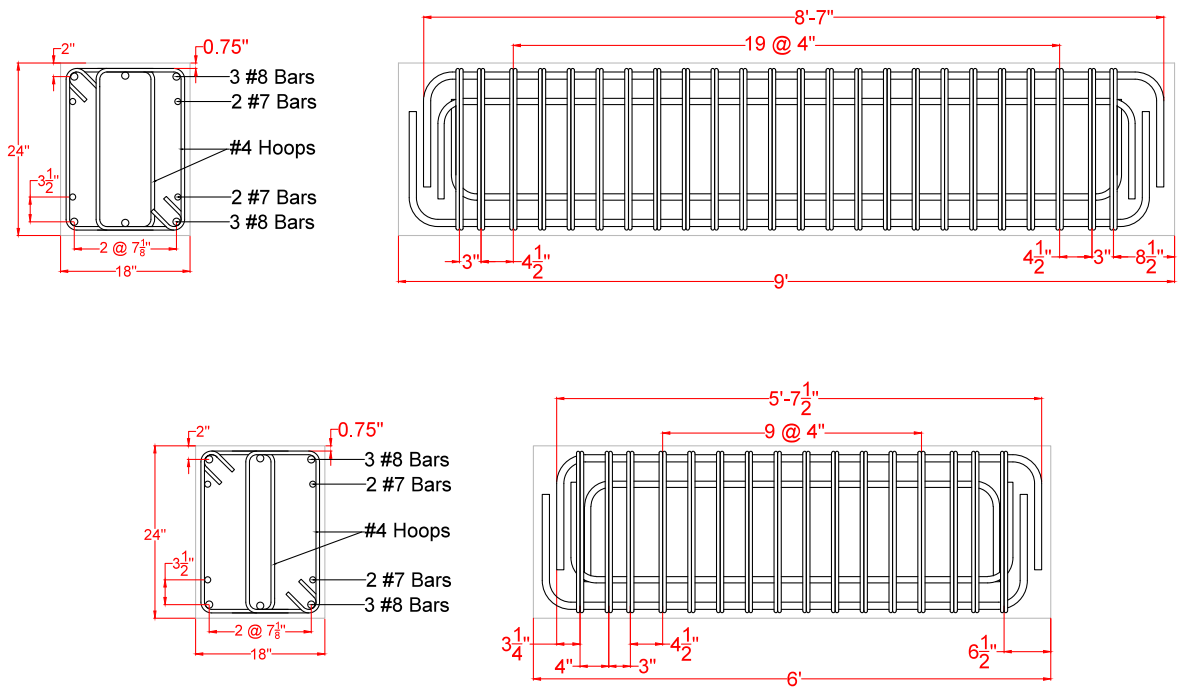


**Figure 2.7: Reinforcement for the End Blocks Simulating Wall Boundary Regions (above: top block; below: bottom block)**

**Table 2.2: FRC Proportions**

| Material | Proportions by Weight |
|---|---|
| Portland Cement | 1.2 |
| Class C Fly Ash | 0.3 |
| Torpedo Sand | 1.7 |
| Coarse Aggregate | 1.0 |
| Water | 0.6 |

Three FRC batches of approximately 3.5 $ft^3$ were mixed every time a coupling beam specimen was cast. Half of each coupling beam plus several material samples were cast with each of the first two batches of FRC, while the third batch was used to finish casting the remainder material

test samples. The concrete mixer, along with several materials sample forms and a coupling beam specimen ready for casting, can be seen in Figure 2.8.

The concrete was mixed using the following procedure:

- Fly ash, cement and sand were added into the concrete mixer and mixed until all three materials were mixed thoroughly and uniformly (approximately 4 minutes).
- Between 50 to 70% of the water was gradually added and mixed until a fairly workable mortar was achieved.
- The coarse aggregate was then added and mixed thoroughly for approximately 3 minutes. Additional water was added if the concrete consistency was deemed too dry.
- Fibers were added and mixed for approximately 3 minutes. The mixer was then stopped for 2-3 minutes to allow the glue binding the fibers to dissolve in the water. The concrete was mixed again for an additional 2-3 minutes to disperse the fibers throughout the fresh concrete.

**Figure 2.8: Mixing FRC and Coupling Beam Specimen Ready for Casting**

None of the aggregates were oven dried before mixing and their moisture content varied considerably. Therefore, adjustments due to moisture content of the aggregates were not possible. Because of this, often times the amount of water required by design was not entirely used. The decision of how much water to use was made by inspecting the fresh concrete until the workability of the mixture was deemed acceptable. Table 2.3 presents the average slump for the FRCs used in all eight coupling beam specimens.

**Table 2.3: Summary of the FRC used for each Coupling Beam Specimen**

| Coupling Beam Specimen | Fiber Type | $V_f$ | Slump (in.) |
|---|---|---|---|
| CB1 | HE 55/35 | 1.25% | 9.1 |
| CB2 | HE 55/35 | 1.25% | 7.8 |
| CB3 | RC 55/30 BG | 1.25% | 7.2 |
| CB4 | RC 55/30 BG | 1.00% | 7.0 |
| CB5 | RC 80/30 BP | 1.00% | 6.9 |
| CB6 | HE 55/35 | 1.50% | 4.6 |
| CB7 | RC 80/30 BP | 1.50% | 5.8 |
| CB8 | RC 80/30 BP | 1.50% | 5.4 |

Each coupling beam specimen was cast and covered with plastic until it was demolded a day or two after casting. In order to have a complete specimen the precast coupling beam was inserted into the forms for the end blocks, which had all the reinforcement already in place. Figure 2.9 shows the specimen being inserted into the forms for the end blocks in preparation for casting. Each coupling beam was embedded into the end blocks approximately 3/4 in. (i.e., until the concrete surface of the precast beam was in contact with the reinforcement cage of the end blocks). Once the beam was inserted into the forms, it was squared and leveled as best as possible and finally secured for casting the end blocks. The end blocks were cast using ready-mix concrete with a specified compressive strength of 5000 psi and a maximum aggregate size of 3/8 in., ordered from a local supplier. A set of end blocks being cast can be seen in Figure 2.10 and a finished coupling beam specimen is shown in Figure 2.11.

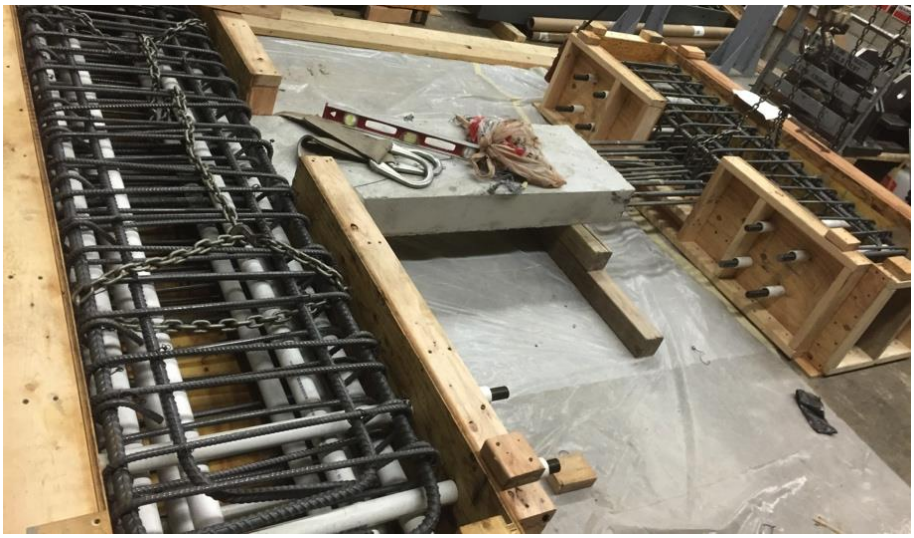

**Figure 2.9: Precast FRC Coupling Beam Being Inserted Into End Block Reinforcement and Forms**

**Figure 2.10: End Blocks Being Cast**

### 2.2.3 Test Setup Description

As discussed previously, each coupling beam specimen consisted of a rectangular section coupling beam connected to two stiff blocks simulating the edges of the structural walls being coupled. For testing convenience, the coupling beams were tested rotated 90° (vertical) from

their typical horizontal orientation. The test setup, shown in Figure 2.12, was designed based on the existing features and limitation of the laboratory.

**Figure 2.11: Finished Coupling Beam Specimen**

One of the two end blocks was anchored to the laboratory strong floor. Lateral displacements (and shear) were applied to the coupling beam through a horizontally-oriented 200-kip hydraulic actuator connected at one end to a reaction concrete block (see Figure 2.13) and at the other end to a stiff steel arm, in turn connected to the top block of the specimen. In order keep both end blocks parallel during testing, two vertical steel arms were used, connected at one end to the strong floor and at the other end to the top block. Each of these two arms was instrumented with a load cell. Besides keeping the two blocks as parallel as practicable, these links also provided restraint against axial expansion of the coupling beam caused by concrete cracking and reinforcement yielding during testing. In real buildings, restraint against axial expansion of the coupling beams is provided by the walls and floor slabs. Thus, ignoring this restraint during testing would prevent the evaluation of expansion-induced axial forces on coupling beam behavior.

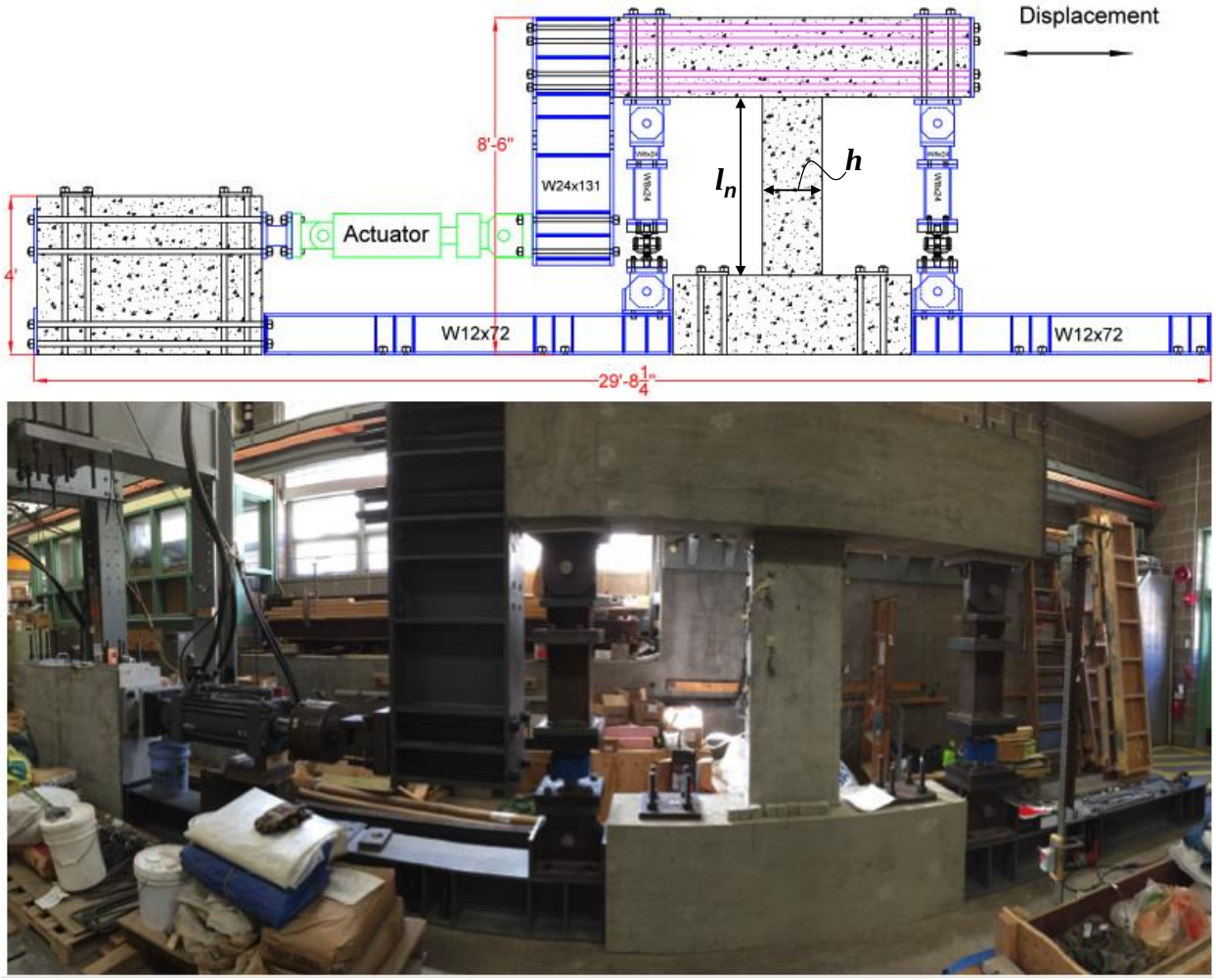


**Figure 2.12: Coupling Beam Test Setup**

**Figure 2.13: Hydraulic Actuator Connected to Concrete Reaction Block**

### 2.2.4 Instrumentation Used

Several instruments and sensors were used to monitor displacements, forces and deformations applied to or experienced by the coupling beam specimens. Displacements and forces applied by the hydraulic actuator were monitored through an LVDT and load cell attached to the actuator. Two horizontal string potentiometers, attached to the top and bottom specimen blocks, were used during the test to control the applied relative horizontal displacement between the top and bottom blocks. Relative block displacements, as well as deformations experienced by the coupling beams, were monitored through the use of a non-contact infrared-based system (NDI Measurement Sciences, 2011), where the position of markers attached to the specimen surface was continuously monitored during testing. The Optotrak Certus system by NDI Measurement Sciences allowed tracking the position of infrared markers in real time with a precision ranging from 0.004 to 0.01 in. The marker grid used for the coupling beams with $l_n/h$ of 3.0 and 2.0 are shown in Figure 2.14 and Figure 2.15 respectively.

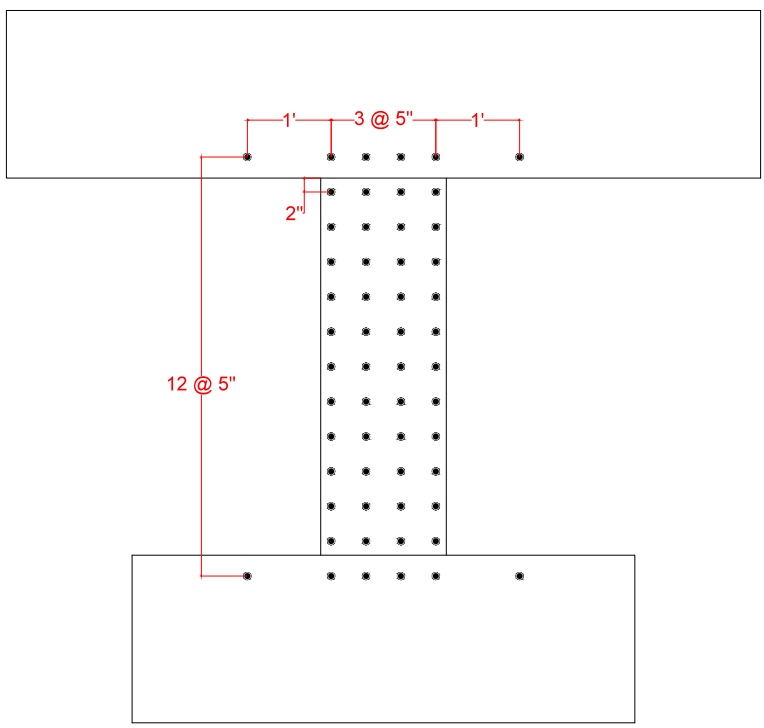


**Figure 2.14: Optotrak Marker Layout for Coupling Beams with $l_n/h = 3.0$**

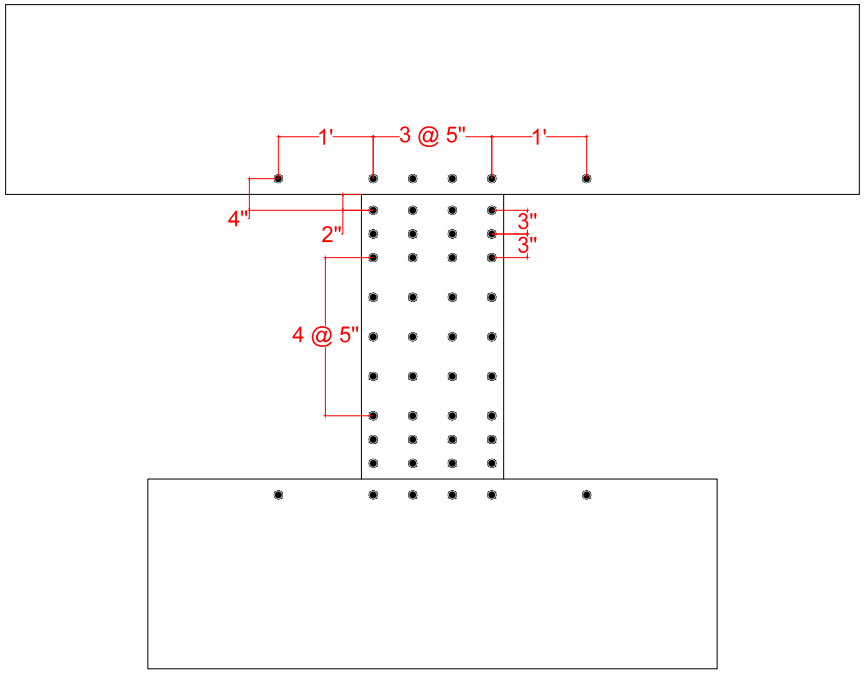


**Figure 2.15: Optotrak Marker Layout for Coupling Beams with $l_n/h = 2.0$**

In order to monitor the axial load developed in the coupling beams during testing, two 100-kip capacity load cells were installed in the vertical steel links that restrained the axial expansion of the coupling beams.

Strains at various locations in the steel reinforcement were also measured throughout the coupling beam tests. Strain gauges were installed in both longitudinal and transverse steel reinforcement and protected against moisture and other hazards with strain gauge coatings and electrical mastic tape. Strain gauges being installed and coated strain gauges are shown in Figure 2.16. The locations of the strain gauges on Specimens CB1, CB2 through CB5, and CB6 through CB8 are shown in Figure 2.17, Figure 2.18 and Figure 2.19, respectively. Strain gauges on longitudinal, transverse and dowel reinforcement are labeled as F (flexural), S (shear), and D (dowel), respectively.

**Figure 2.16: Strain Gauge Installation (Top) and Strain Gauges with Finished Coatings (Bottom)**

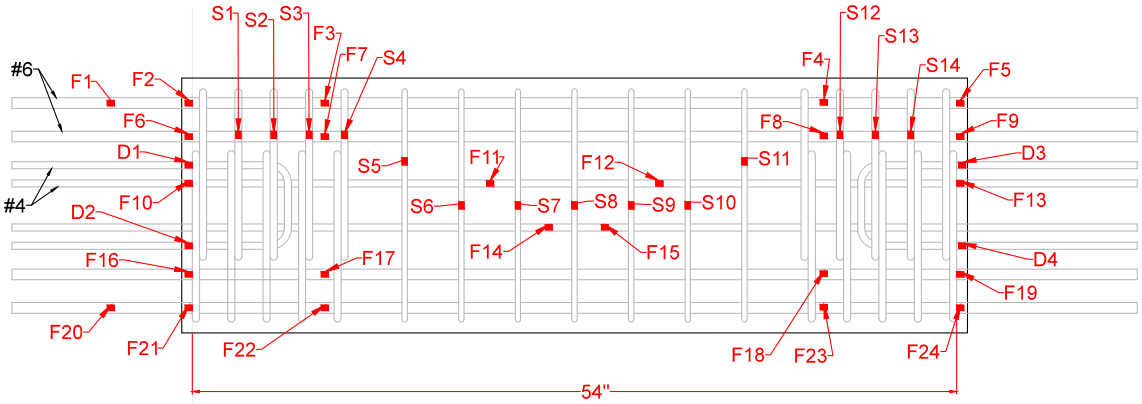


**Figure 2.17: Strain Gauge Locations and Identification (Coupling Beam CB1)**

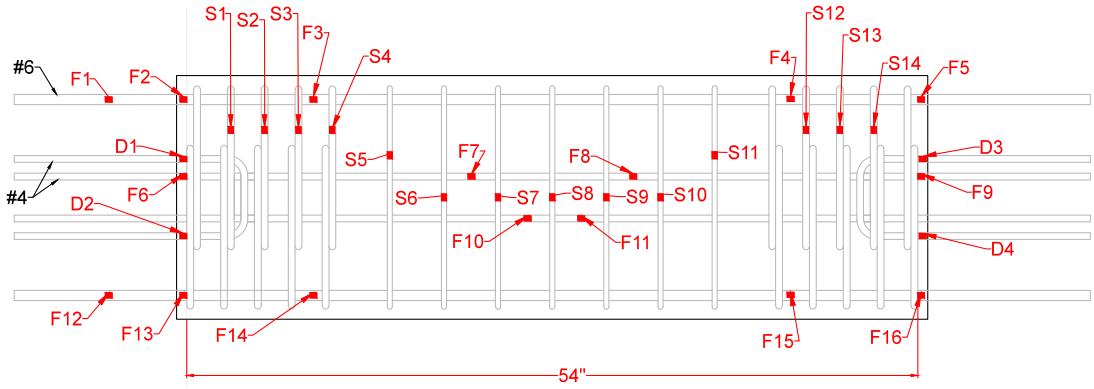


**Figure 2.18: Strain Gauges Locations and Identification (Coupling Beams CB2-CB5)**

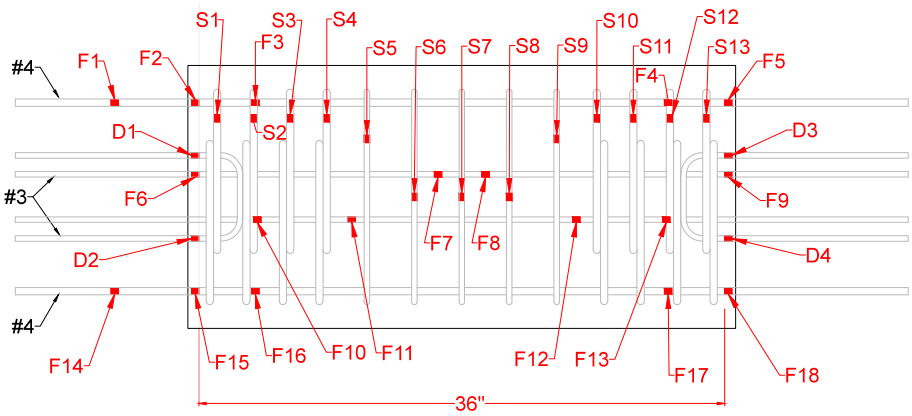


**Figure 2.19: Strain Gauges Locations and Identification (Coupling Beams CB6-CB8)**

### 2.2.5 Test Protocol (Displacement History)

The coupling beam tests consisted of applying cycles of lateral displacement reversals of increasing magnitude. This allowed the study of the behavior of the FRC coupling beams when subjected to reversed cyclic displacements similar to those that the coupling beam could experience during a large earthquake. The drift history applied to Coupling Beam CB1 is shown in Figure 2.20. The drift history applied to all other coupling beams, shown in Figure 2.21, was slightly different than that applied to Coupling Beam CB1 because the latter was deemed too severe. Coupling beam drift in Figure 2.20 and Figure 2.21 refers to the relative lateral displacement between the top and bottom blocks divided by the coupling beam clear span length,

$l_n$. The drift magnitude was incremented by 0.25% after each cycle up to 1.0% drift. This drift increment was then increased to 0.5% for the cycles up to 2.0% drift. From 2.0% onwards the drift increment was 1.0%. One cycle was applied to each drift level, except for the cycles to drift levels below 1.0%, which were applied twice. Positive loading direction refers to the actuator pulling the coupling beams while the negative direction refers to the actuator pushing the coupling beam.

### 2.2.6 Drift Calculation and Adjustment for End Block Rotations

Small rotations of the end blocks during testing led to minor differences between the target drift and the actual drift applied. Thus, the drifts reported correspond to the average chord rotation of the coupling beams, which accounted for any rotation of the end blocks. The exceptions are the drifts reported when referring to the application of a particular drift cycle during a test (e.g., drift cycles are referred to based on the target drift; 2.0%, 3.0%, etc.).

Figure 2.22 shows the deformed shaped of a coupling beam with the bottom and top blocks rotated by an angle $\alpha_B$ and $\alpha_T$, respectively. The corrected coupling beam drift was calculated as,

$$drift = \frac{\Delta}{l_n} + \frac{(\alpha_T + \alpha_B)}{2} \tag{2}$$

where $\Delta$ is the relative lateral displacement of the end blocks, $l_n$ is the clear span length of the coupling beam, and $\alpha_B$and $\alpha_T$ are the angle of rotation of the end blocks in radians and positive as shown in Figure 2.22.

### 2.2.7 Calculation of Coupling Beam Shear Distortions

In order to determine the deformations occurring throughout the length of each coupling beam specimen, the grid of Optotrak markers was divided into several marker strips. Each marker strip consisted of two adjacent rows of optical markers, which were used to determine the average shear distortion per strip. The marker layout and strips used for the coupling beam specimens with $l_n/h$ of 3.0 and 2.0 are shown in Figure 2.23 and Figure 2.24, respectively.

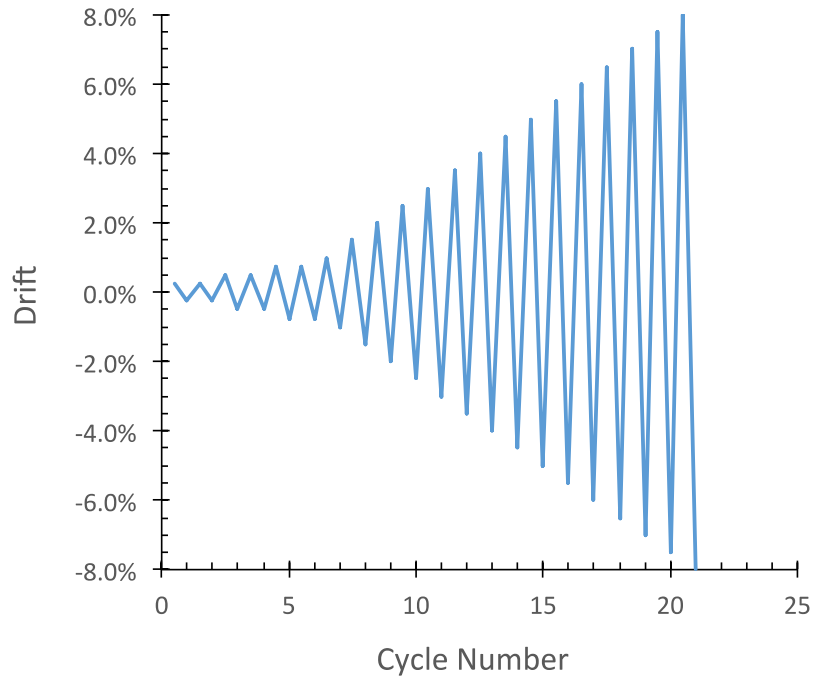


**Figure 2.20: Displacement History used for Specimen CB1**

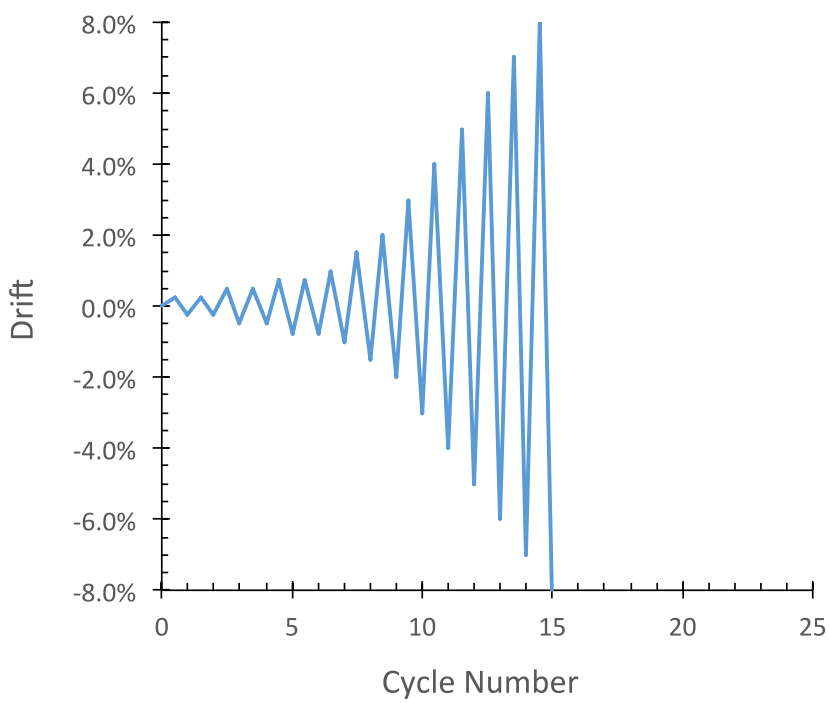


**Figure 2.21: Displacement History used for Specimens CB2 through CB8**

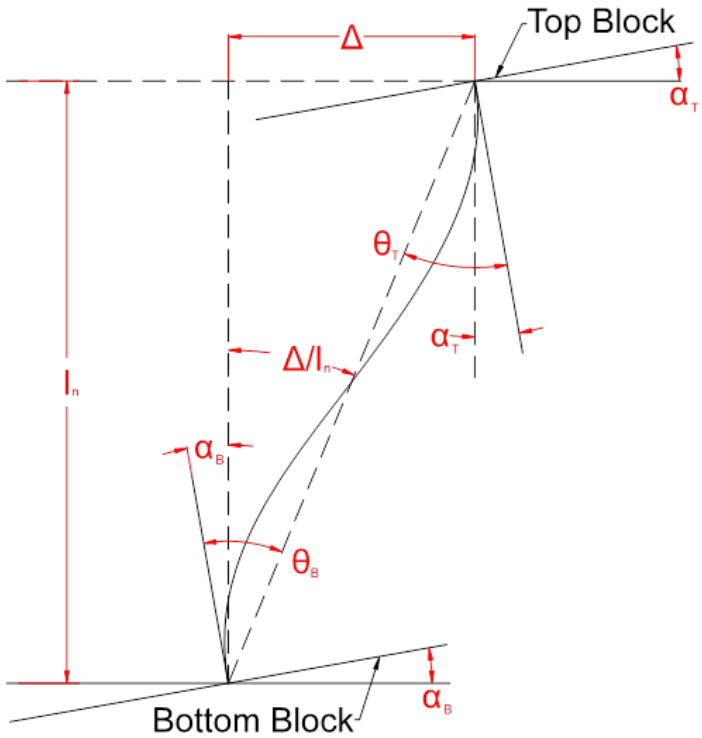


**Figure 2.22: Coupling Beam Deformed Shape for Drift Correction**

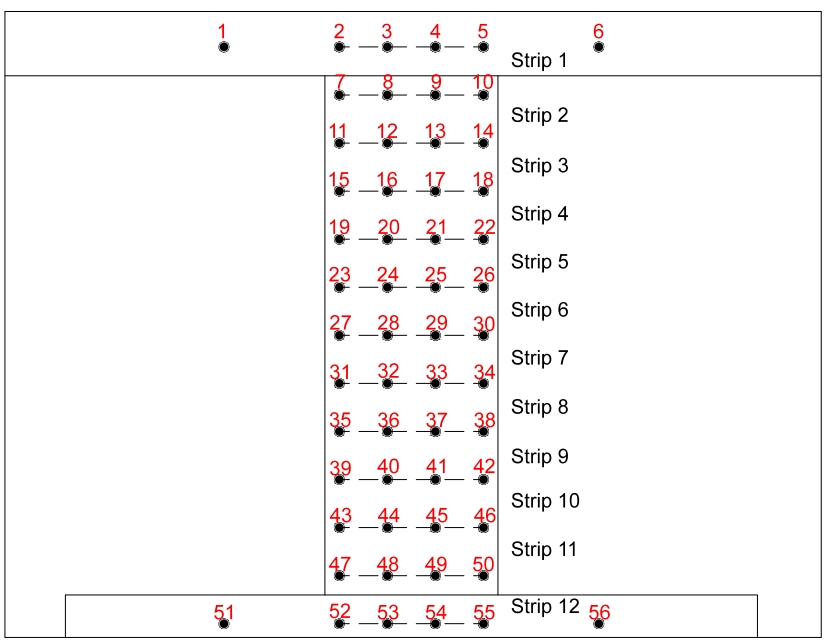


**Figure 2.23: Marker Strips for Coupling Beams with $l_n/h = 3.0$**

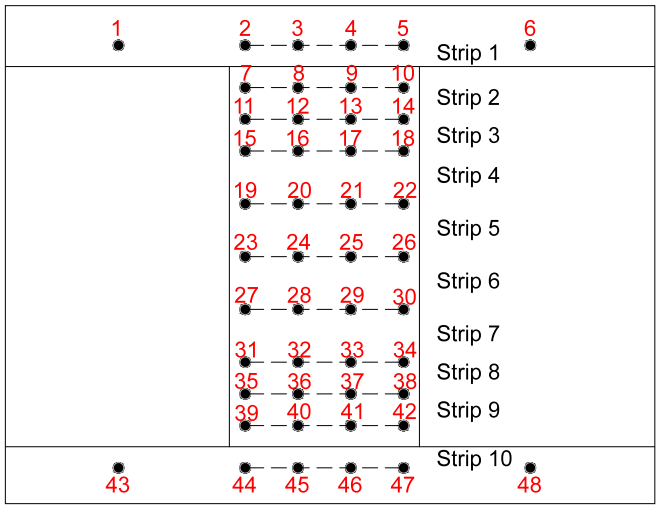


**Figure 2.24: Marker Strips for Coupling Beams with $l_n/h = 2.0$**

Each marker strip can be divided into three rectangular elements with an optical marker at each node. In order to calculate the average shear distortion for each strip, the average shear distortion $\gamma_n$ of each individual element in the strip was calculated. Figure 2.25 shows a typical element in a marker strip in its undeformed and deformed shape.

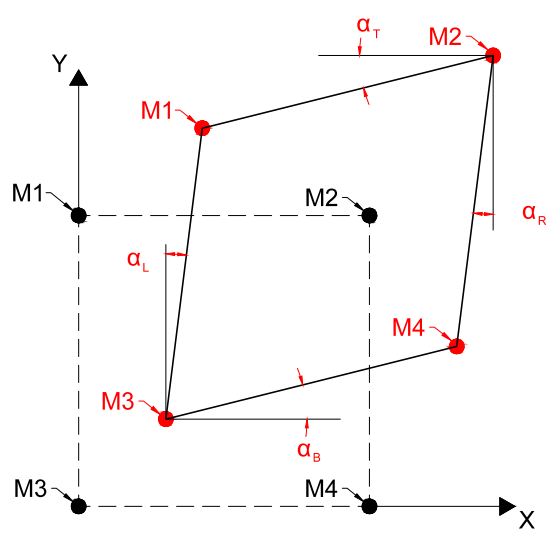


**Figure 2.25: Deformed Element for Illustration of Shear Distortion Calculations**

The shear distortion of each element throughout the coupling beam and the average shear distortion per strip were calculated for each time instant of data recorded. For illustration

purposes, consider the element shown in Figure 2.25, which is formed by markers M1 through M4. At any given time *t*, the coordinates of M1 through M4 define the shape of the $n^{th}$ element on the beam. The distortion angle $\gamma_n$ can be calculated as,

$$\gamma_n = \frac{(\alpha_T + \alpha_B)}{2} + \frac{(\alpha_L + \alpha_R)}{2} \tag{3}$$

where the angles $\alpha_T$, $\alpha_B$, $\alpha_L$, and $\alpha_R$ are as shown in Figure 2.25. The angles $\alpha_T$ and $\alpha_B$ must not be confused with the angles shown in Figure 2.22, used for the adjusted drift calculations. These angles are calculated based on the coordinates of each marker as,

$$\alpha_T = \frac{(Y_2 - Y_1)}{(X_2 - X_1)};\ \alpha_B = \frac{(Y_4 - Y_3)}{(X_4 - X_3)};\ \alpha_L = \frac{(X_1 - X_3)}{(Y_1 - Y_3)};\ \alpha_R = \frac{(X_2 - X_4)}{(Y_2 - Y_4)} \tag{4}$$

The average shear distortion of the $i^{th}$ strip, formed by elements $n$, $n+1$ and $n+2$, was then calculated as,

$$(\gamma_s)_i = \frac{(\gamma_n + \gamma_{n+1} + \gamma_{n+2})}{3} \tag{5}$$

### 2.2.8 Calculation of Coupling Beam Curvatures

The average curvature for each marker strip was calculated based on the coordinates of the markers located at the corners of the strip. Figure 2.26 shows the deformed shape of the $i^{th}$ strip of the coupling beam and the variables used to calculate the curvature on each strip along the beam length.

The markers identified as $TL_i$, $TR_i$, $BL_i$ and $BR_i$ in Figure 2.26 define the location of the four corners of the $i^{th}$ strip in the coupling beam. Based on their position data the average vertical strains at the left and right side of the strip were calculated and used to define the average curvature of the strip as follows,

$$\phi_i = \frac{(\varepsilon_{R_i} - \varepsilon_{L_i})}{L_{s_i}} = \frac{\left(Y_{TR_i} - Y_{BR_i}\right) - (Y_{TL_i} - Y_{BL_i})}{L_{s_i}\, h_{s_i}} \tag{6}$$

where $\varepsilon_R$ and $\varepsilon_L$ are the strains at the right and left side of the strip as shown in Figure 2.26, $L_s$ is the average length of the strip, $h_s$ is the average height of the strip, and $\phi_i$ is the curvature of the $i^{th}$ strip on the coupling beam at any given time $t$.

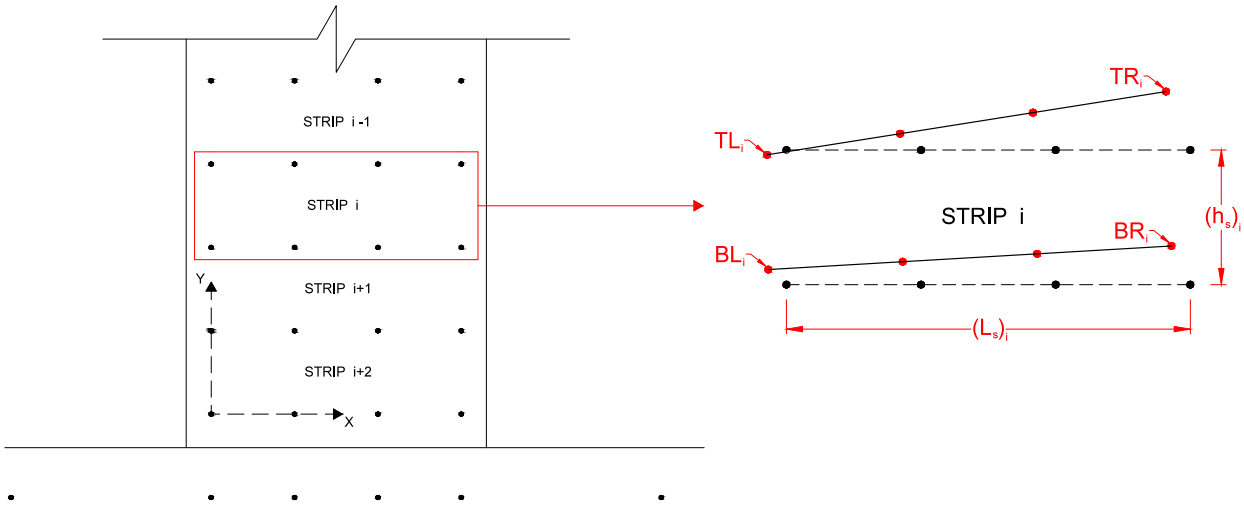


**Figure 2.26: Curvature Calculation Variables and Deformed Marker Strip**

## 2.3 FRC Material Testing

The behavior of the various FRCs investigated was evaluated through four types of tests: 1) four-point bending tests on notched beams, 2) four-point bending tests on un-notched beams, 3) direct tensile tests on notched specimens, and 4) cylinder compressive tests.

Table A1 in Appendix A shows a list of all material samples tested along with the test dates. Although it was desirable to perform all four types of tests for a given FRC material within a few days, this was not always possible, particularly for the FRC materials used in Specimens CB6 and CB7. All tests, however, were conducted at least 28 days after casting and thus, increases in strength over time beyond the earliest test date were expected to be minor (e.g., a 16% increase in compressive strength was measured over a period of 117 days for the FRC used in Specimen CB7). Therefore, changes in the correlation between bending, tension and compression test results due to differences between test dates were expected to be negligible and overshadowed by regular variabilities associated with concrete material tests.

### 2.3.1 Bending Tests (Notched Beam)

In order to evaluate the flexural performance of the various FRCs considered in this study, notched beam specimens were tested using an MTS load frame in a four-point loading configuration as shown in Figure 2.27. All the specimens were tested using a displacement control protocol with a displacement rate of 0.005 in./min based on the displacement of the hydraulic actuator. The notched beam specimens consisted of 6 by 6 by 20 in. elements with a notch 1.5 in. deep and approximately 1/8 in. wide saw-cut at mid-span. The Optotrak system was used to monitor beam deflections as well as crack openings throughout the tests. Figure 2.27 shows a schematic of the setup used for testing the notched beam specimens, along with the infrared marker layout.

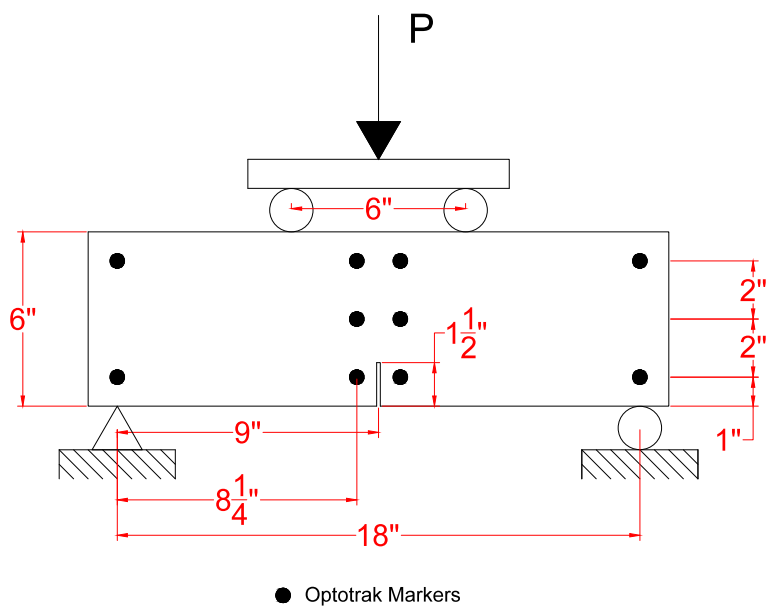


**Figure 2.27: Notched Beam Test Setup and Marker Layout**

The crack opening at the location of the notch end was estimated based on the marker position data. The crack opening of each notched beam specimen can be calculated using Equation 7, where $D_{Top}$ is the distance in inches from the bottom of the beam to the uppermost row of markers, $Nd$ is the notch depth in inches, $\theta_L$ and $\theta_R$ are the angle of rotation (rad) of the column of markers to the left and right of the notch respectively (taken as positive as shown in Figure 2.28), $\Delta X_{Top}$ is the distance between the two marker columns adjacent to the notch, at the top

row of markers, and $(w_{cr})_0$ is equal to $\Delta X_{Top}$ at the initial time $t_0$. Figure 2.28 illustrates the geometry and variables used to calculate the crack opening.

$$w_{cr} = \left(D_{Top} - Nd\right)\left(\theta_L + \theta_R\right) + \Delta X_{Top} - (w_{cr})_0 \tag{7}$$

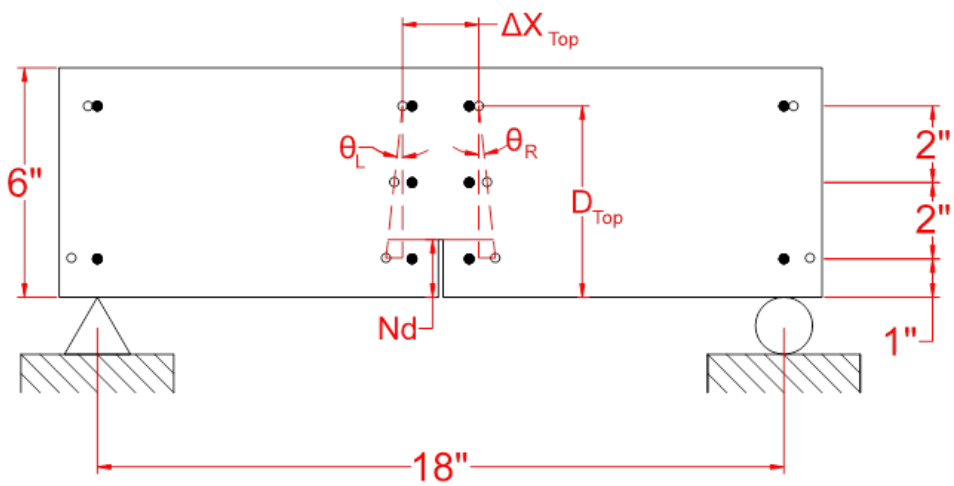


**Figure 2.28: Crack Opening Calculation Schematic**

### 2.3.2 Bending Tests (Un-notched Beams)

In addition to the notched beam specimens, un-notched beam specimens as specified in ASTM C1609-12 were tested to further assess the flexural behavior of the FRCs investigated. These beam specimens consisted of 6 by 6 by 20 in. elements that were tested using a four-point loading configuration with the same loading rate used for the notched beams (0.005 in./min). The Optotrak system was once again used to monitor deflections and crack openings in these beams. However, because the exact location of the origin of the crack is not known *a priori*, a larger marker grid was used compared to that used on the notched beams. Figure 2.29 shows the test configuration as well as the marker layout utilized for these beams.

In order to calculate the crack opening, the location at which the concrete first cracked was required. The start of the crack was estimated using a combination of inspection of the tested sample, change in distance between the markers in the bottom row, as well as the observed rotations on each column of markers. Once the approximate location of the crack was

determined, the rotations of the columns of markers closest to the crack were selected for calculation of crack opening. Figure 2.30 shows the markers in the undeformed and deformed beam shape, as well the variables used to calculate the crack opening of the beams.

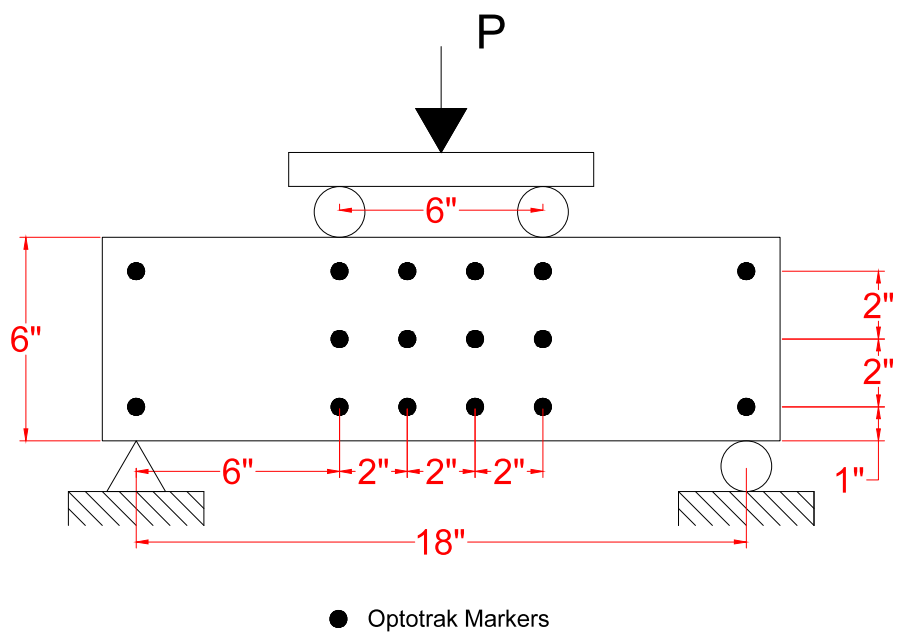


**Figure 2.29: Un-notched Beam Test Setup and Marker Layout**

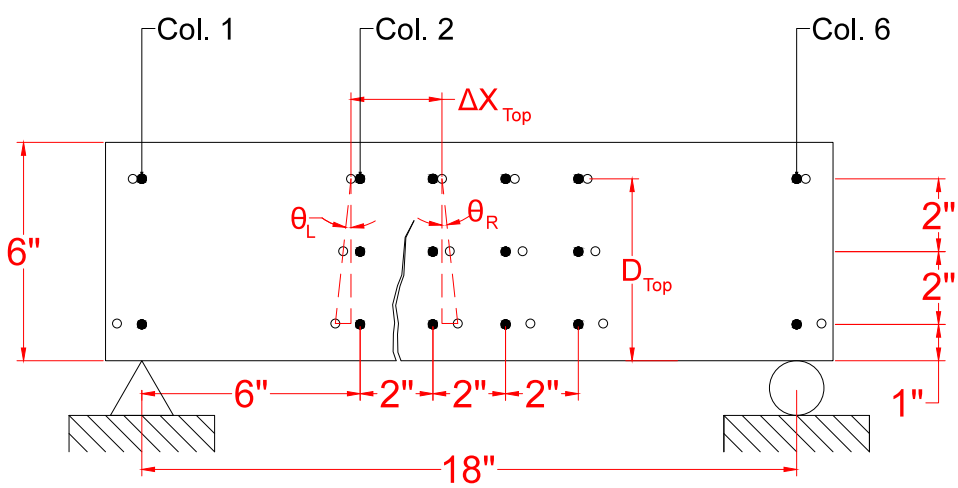


**Figure 2.30: Crack Opening Calculation Schematic (Un-notched Beams)**

The calculation of the crack opening is very similar to that for the notched beams. However, due to the varying location of the crack, the rotations and distance between markers used to calculate the crack opening varied for each specimen. That is, $\Delta X_{Top}$, $\theta_L$ and $\theta_R$ were calculated using the

columns of markers closest to the crack origin (see Figure 2.30). In some samples, one or both of the columns of markers closest to the crack origin would result in anomalous crack opening calculations due to markers falling off. Whenever this occurred the next closest column (or columns) of markers were used for the calculation of the crack opening. The crack opening for the beam samples was calculated according to Equation 8.

$$\mathrm{w_{cr}} = \left(D_{Top}\right)\left(\theta_L + \theta_R\right) + \Delta X_{Top} - \left(\Delta X_{Top}\right)_0 \tag{8}$$

### 2.3.3 Direct Tension Tests

The tension specimens consisted of a 6 by 6 by 14 in. concrete prism with a 5/8 in. diameter reinforcement bar along its longitudinal axis. The reinforcing bar was discontinuous at mid-length of the specimen, where a notch with a depth of 3/4 in. was saw-cut around the specimen to force the failure to occur at this location. The bar ends were clamped into an MTS hydraulic load frame and the specimen tested under displacement control at a rate of 0.002 in./min until the specimen cracked. After cracking, the displacement rate was increased to 0.02 in./min until the end of the test. Optotrak infrared markers were used to track the crack opening of the specimen throughout the test. A tension specimen and the optical marker layout are shown in Figure 2.31.

In order to estimate the crack opening in the specimens while taking into account any rotation on each side of the notch during testing, the data from the markers were used to define two planes (above and below the notch) corresponding to the sections where the markers were located. Three points in space were required to define these planes. Thus, in order to define the plane above the notch, the coordinates of marker 1 and marker 7 were used in conjunction with a third point defined by the average of the coordinates of markers 3 and 5. Similarly, the plane below the notch was calculated using markers 2, 4, 6 and 8. The plane is defined by Equation 9.

$$ax + by + cz = d \tag{9}$$

In order to calculate coefficients $a$, $b$ and $c$, two vectors on the plane must be known; for example, vectors $\overline{71}$ and $\overline{\mathrm{A1}}$ as shown in Figure 2.32. The vectors, coefficients and constant for

the plane above the notch were calculated according to Equations 10, 11 and 12 respectively. These calculations were performed for each time instant throughout the test allowing the definition of a plane for each time instant.

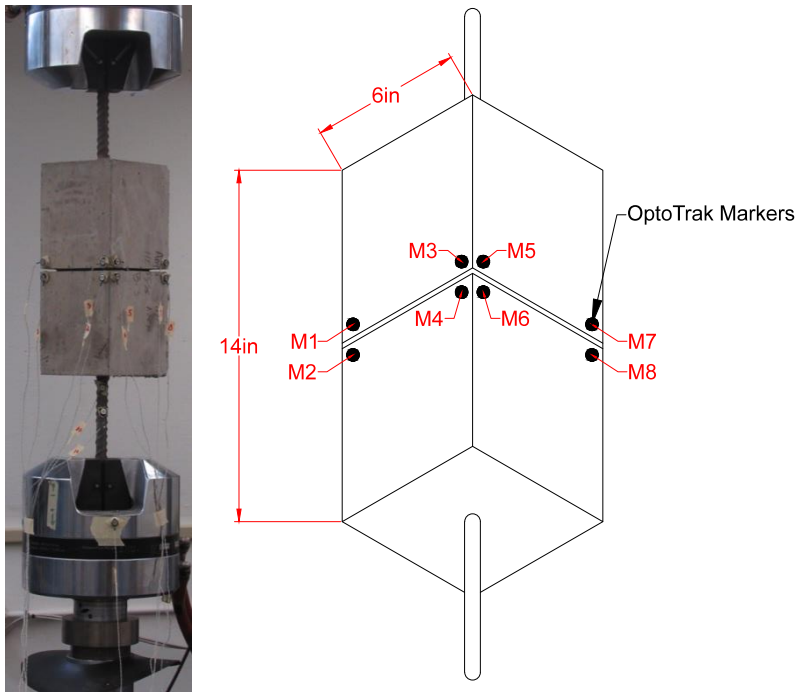


**Figure 2.31: Tension Specimen and Marker Layout**

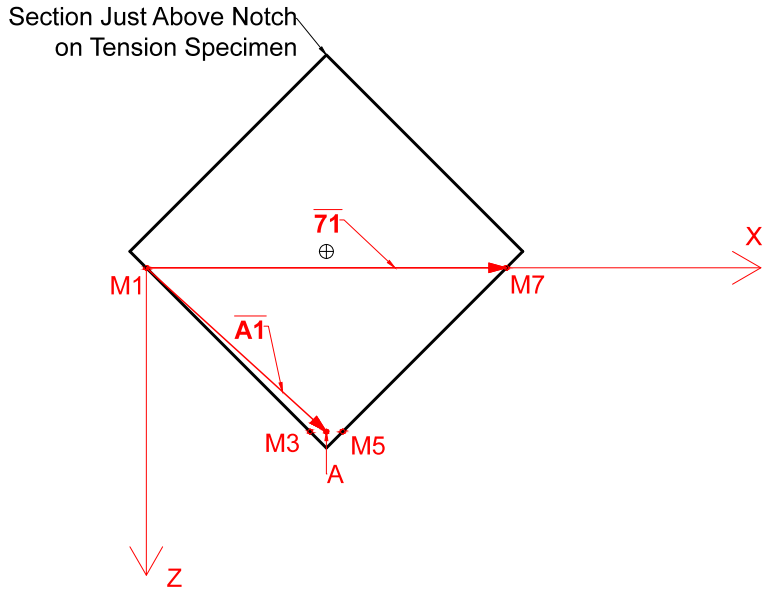


**Figure 2.32: Vectors Used in the Calculation of Crack Opening of the Tension Specimens**

$$\overline{71} = \begin{bmatrix} X_7 - X_1 \\ Y_7 - Y_1 \\ Z_7 - Z_1 \end{bmatrix}; \ \overline{\mathrm{A1}} = \begin{bmatrix} X_A - X_1 \\ Y_A - Y_1 \\ Z_A - Z_1 \end{bmatrix} \tag{10}$$

$$\overline{A1} \times \overline{71} = \begin{bmatrix} a_{\mathrm{Top}} \\ b_{\mathrm{Top}} \\ c_{\mathrm{Top}} \end{bmatrix} \tag{11}$$

$$d_{\mathrm{Top}} = \begin{bmatrix} a_{\mathrm{Top}} \\ b_{\mathrm{Top}} \\ c_{\mathrm{Top}} \end{bmatrix} \cdot \begin{bmatrix} X_1 \\ Y_1 \\ Z_1 \end{bmatrix} \tag{12}$$

The resulting plane equation is:

$$a_{\mathrm{Top}}x + b_{\mathrm{Top}}y + c_{\mathrm{Top}}z = d_{\mathrm{Top}} \tag{13}$$

Once the planes were defined, the coordinates of the centroid of the block were calculated for each time instant using the data from the markers. The X and Z coordinates of the centroid of the prism ($X_c$ and $Z_c$), assuming no twisting, were calculated as (see Figure 2.33):

$$X_c = \frac{\left(\sqrt{(X_3 - X_1)^2 \ + \ (Z_3 - Z_1)^2} + 0.50\ in\right)(X_3 - X_1)}{\sqrt{(X_3 - X_1)^2 \ + \ (Z_3 - Z_1)^2}} \tag{14}$$

$$Z_c = \frac{-0.50\ in\ (Z_3 - Z_1)}{\sqrt{(X_3 - X_1)^2 \ + \ (Z_3 - Z_1)^2}} \tag{15}$$

Once these coordinates were calculated they were used with the equations of the planes to obtain the $Y$ coordinate of the centroid above and below the notch, $Y_{Top}$ and $Y_{Bottom}$, respectively. The crack opening was then calculated as the difference between $Y_{Top}$ and $Y_{Bottom}$ for each time instant, minus the original difference at initial time $t_0$. The tensile responses of the tested samples for the FRCs used in the coupling beams are presented in Section 3.3.

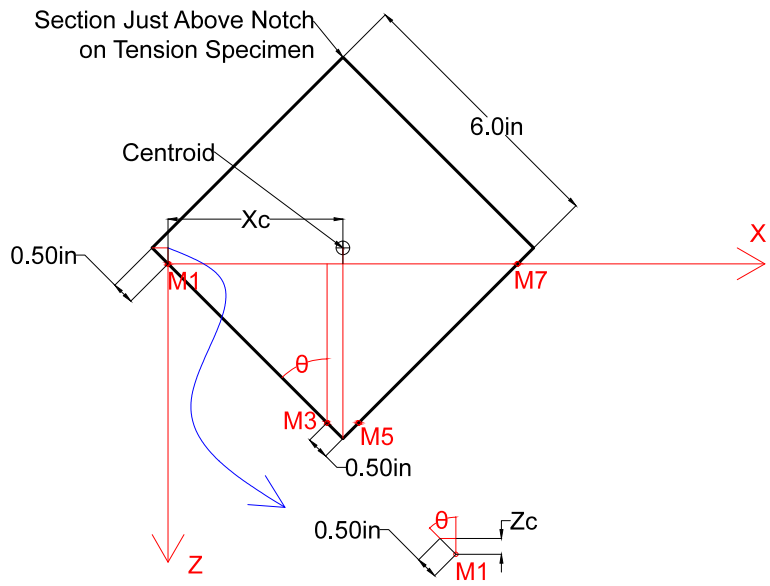


**Figure 2.33: Tension Block Centroid Coordinates**

### 2.3.4 Compression Cylinder Tests

The compressive strength of the FRCs considered in this experimental work was determined using standard 6 by 12 in. cylinders that were cast along with the eight FRC coupling beams tested. All cylinders were cured in a moisture room for at least 27 days and capped with a sulfur-based compound prior to testing. Two different compression tests were conducted using an Instron SATEC 400-kip compression frame. In order to determine the compressive strength of the FRC of each coupling beam specimen, some cylinders were tested the same day of the coupling beam test in accordance with ASTM C39-14. These cylinders were loading at a rate of 35 ± 7 psi/s. However, in order to measure the full stress-strain response of the FRC cylinders the majority of the cylinders were tested under displacement control at a rate of 0.01 in./min. For these tests a grid of Optotrak markers was used to monitor axial strains. The marker layout consisted of three columns of sensors located at 90° arcs. In order to track the displacement on the sides of the cylinders not visible by the Optotrak camera, small aluminum angles were epoxied to the cylinder sides to serve as base for the optical makers. Figure 2.34 shows the marker layout used for the cylinder compression tests, as well as the aluminum angles that were used to support the markers on the sides of the cylinder.

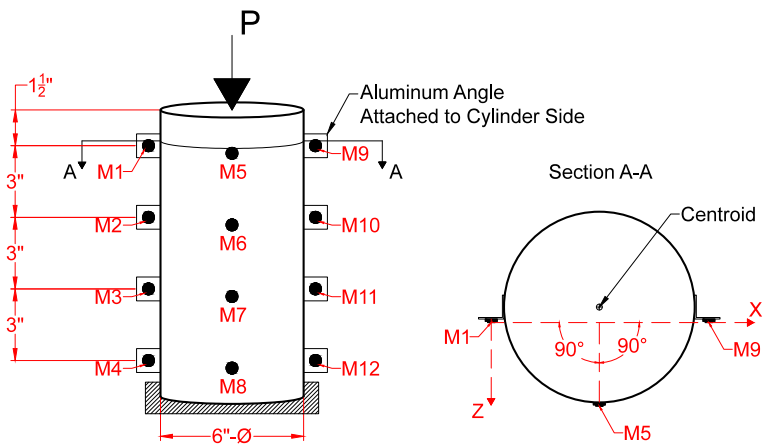


**Figure 2.34: Marker Layout for Cylinder Compression Tests**

Average strains were calculated along all three columns of markers using the uppermost and lowermost markers, i.e. markers 1 and 4, 5 and 8, and 9 and 12. Comparison of these average strains allowed the identification of any significant relative rotation that may have occurred between the cylinder ends during testing. The resulting strains were also compared to the strains calculated at each third of the cylinder (e.g. between markers 1 and 2, 2 and 3, and 3 and 4) to ensure that the strains considered were representative of the overall compressive behavior of the cylinder. Finally, the strains near the centroid of the cylinder were calculated based on the difference between the average *Y* coordinate of markers 1 and 9 and markers 4 and 12. An effort was made to glue the angles such that the average marker coordinate would represent that of the centroid of the cylinder at the section considered. Thus, it was assumed that the strains calculated with the average coordinates of markers 1 and 9 and markers 4 and 12 were a reasonable approximation of the average axial strains on the centroid of the cylinder.

# 3 Material Test Results

## 3.1 Flexural Test Results of FRC Notched Beams

The equivalent bending stress versus deflection responses of the fiber reinforced concretes used in the test coupling beams are shown in Figure 3.1 through Figure 3.8. Each curve on a plot represents the response of a tested sample, cast from the same batches as the coupling beams. Each specimen was identified according to the following naming convention: coupling beam number (e.g. CB1, CB2), followed by specimen type, where NB stands for notched beams, B for un-notched beams, TB for tension blocks, and CYLN for cylinders, and ending with the specimen number. An example of this is CB1NB1, which identifies the first notched beam corresponding to the FRC used for casting Coupling Beam CB1. Equivalent flexural stresses were calculated assuming linear-elastic, uncracked behavior of the beams under four-point bending as follows,

$$f = \frac{P\,L}{b\,h^2} \tag{16}$$

where $P$ is the total applied load, $L$ is the span length, and $b$ and $h$ are the beam width and depth, respectively. For the notched beams, $h$ was equal to 4.5 in., while for the un-notched beams $h$ was equal to 6 in.

For comparison purposes the average notched beam responses for all FRCs are presented in Figure 3.9, normalized by the cracking strength, $f_{cr}$, of each FRC. Figure 3.10 through Figure 3.18 show the flexural responses of the FRC notched beams in terms of equivalent flexural stress versus crack opening. The peak post-cracking strength, $f_{pc}$, and other parameters used to describe the flexural response of the FRC notched beams, are presented in Table 3.1.

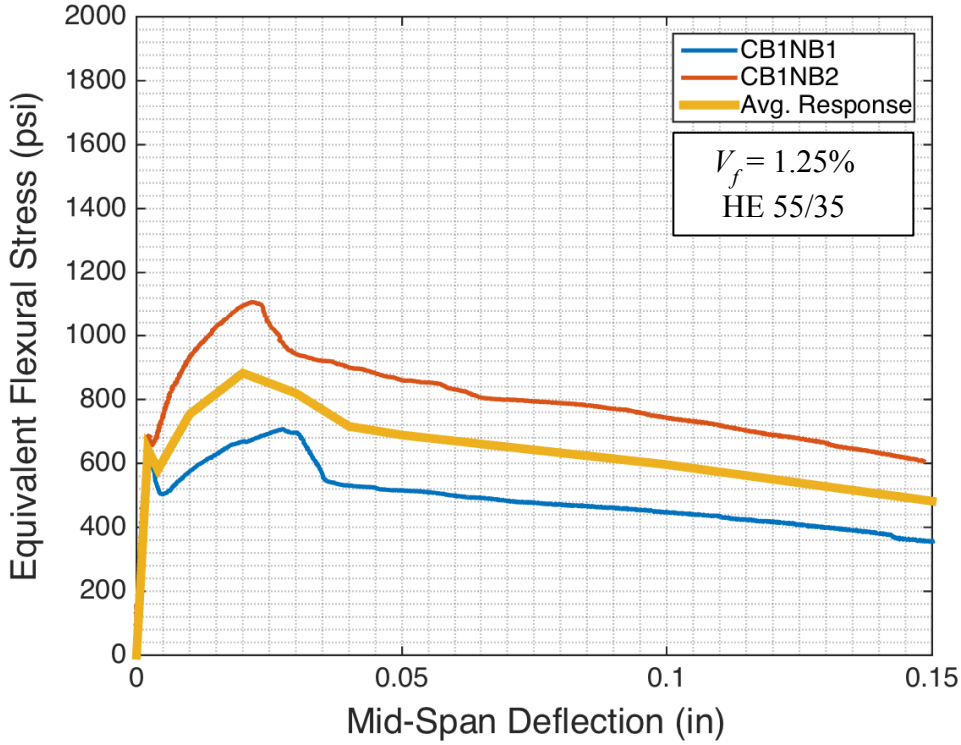


**Figure 3.1: Stress versus Deflection Response (Notched Beams Corresponding to CB1)**

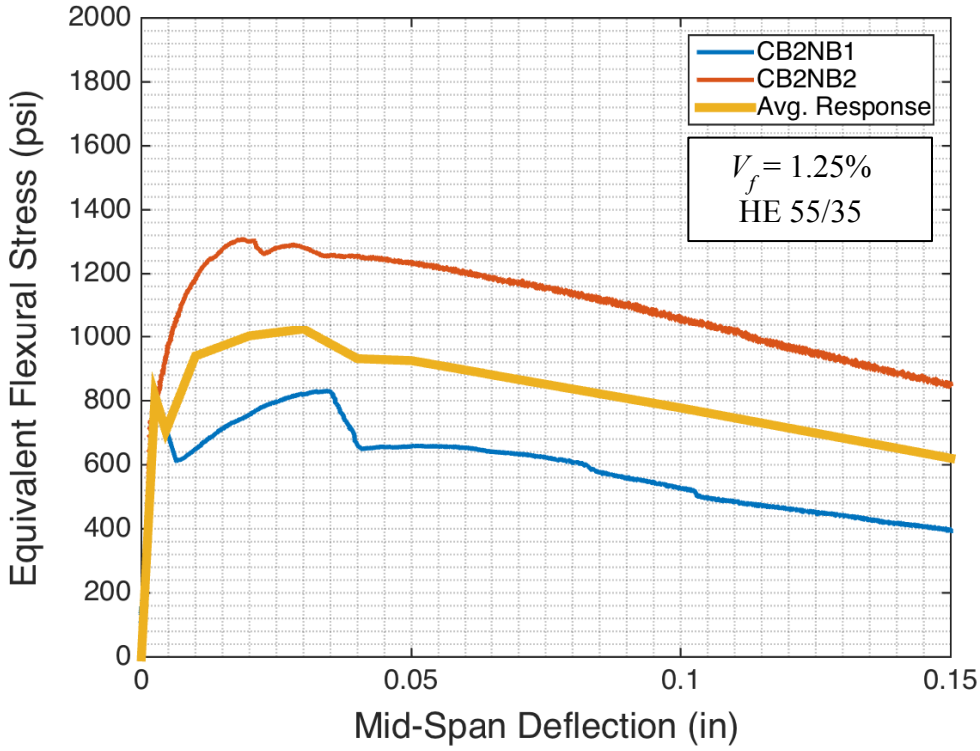


**Figure 3.2: Stress versus Deflection Response (Notched Beams Corresponding to CB2)**

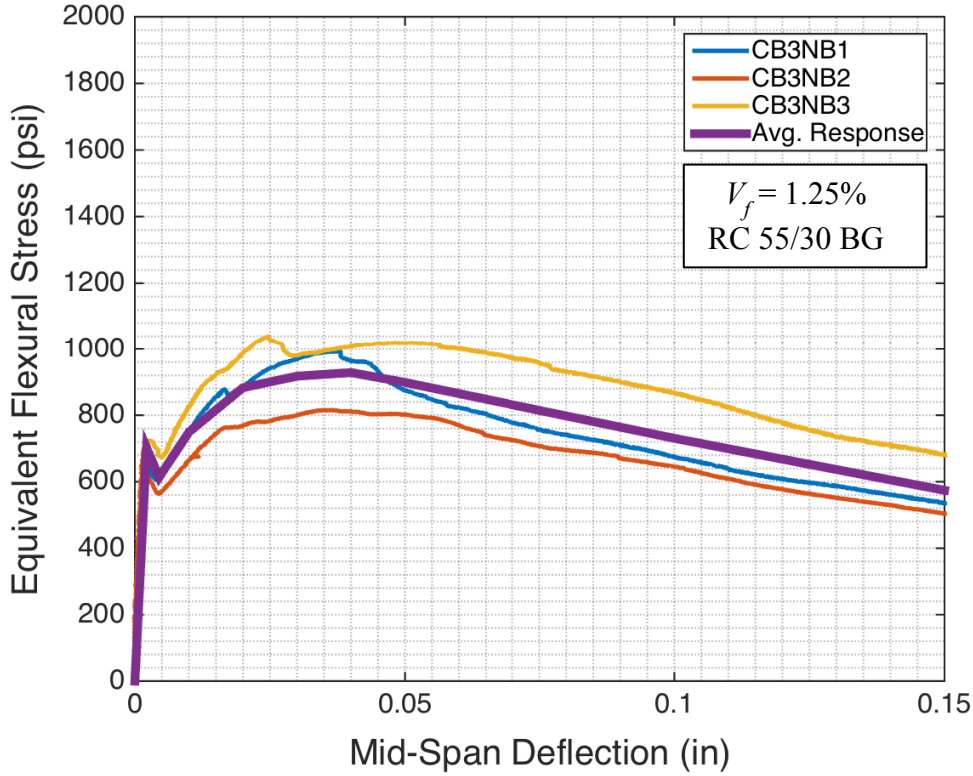


**Figure 3.3: Stress versus Deflection Response (Notched Beams Corresponding to CB3)**

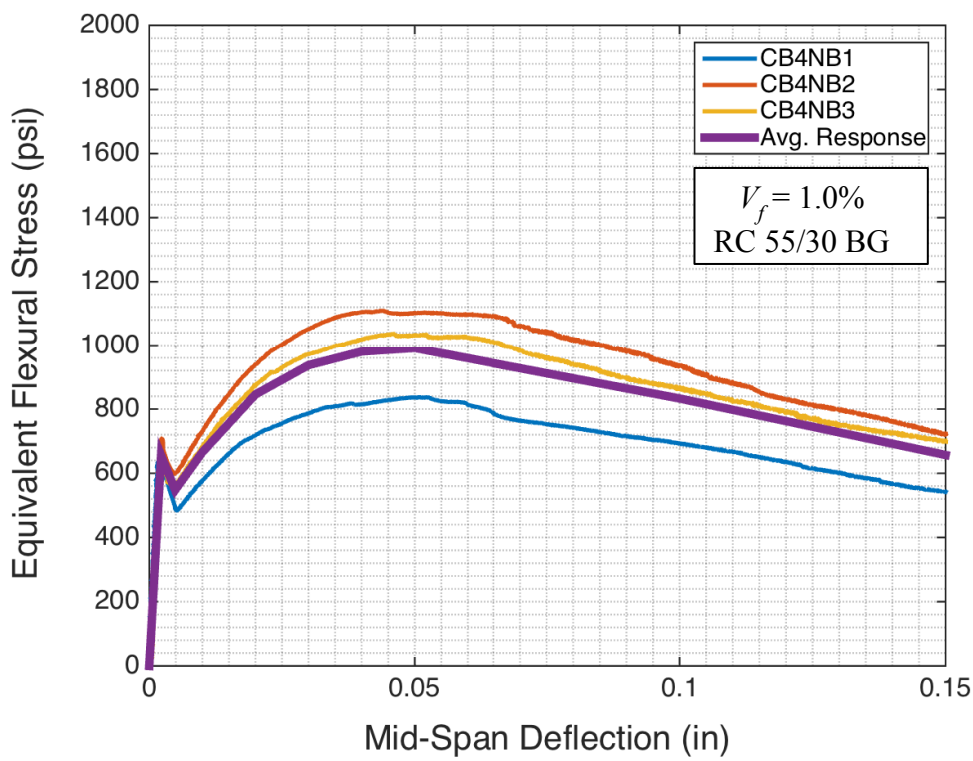


**Figure 3.4: Stress versus Deflection Response (Notched Beams Corresponding to CB4)**

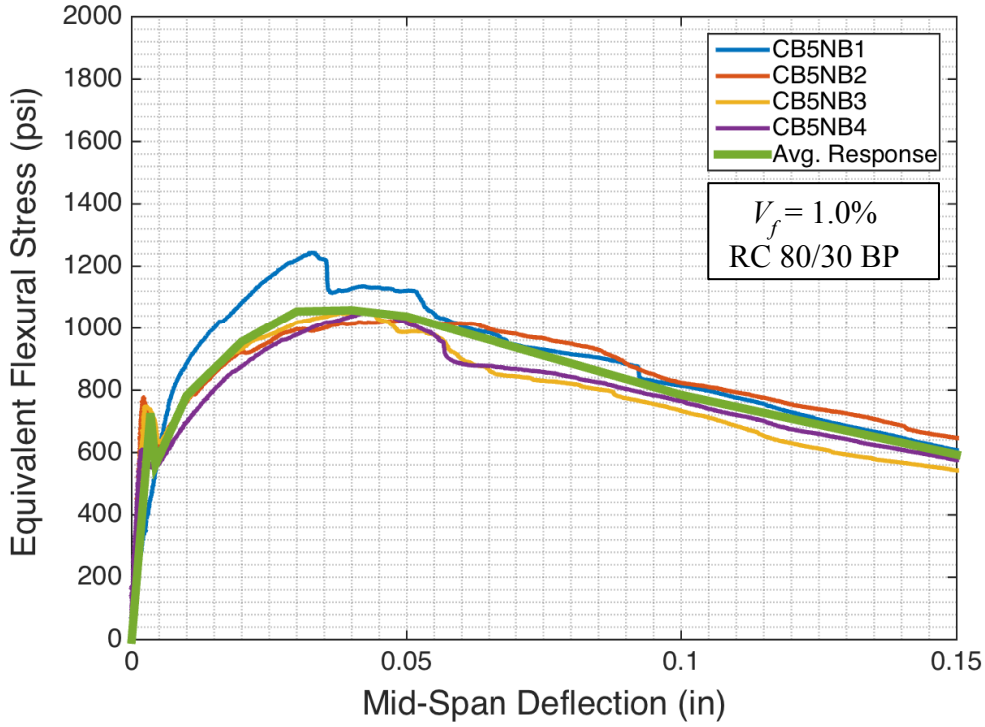


**Figure 3.5: Stress versus Deflection Response (Notched Beams Corresponding to CB5)**

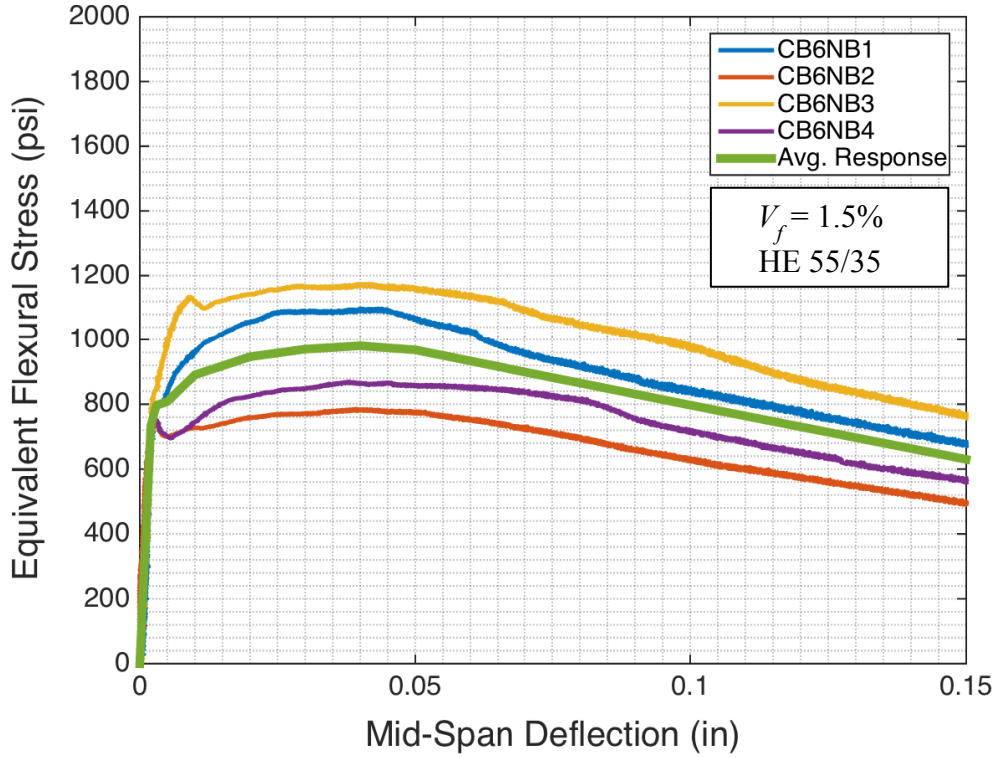


**Figure 3.6: Stress versus Deflection Response (Notched Beams Corresponding to CB6)**

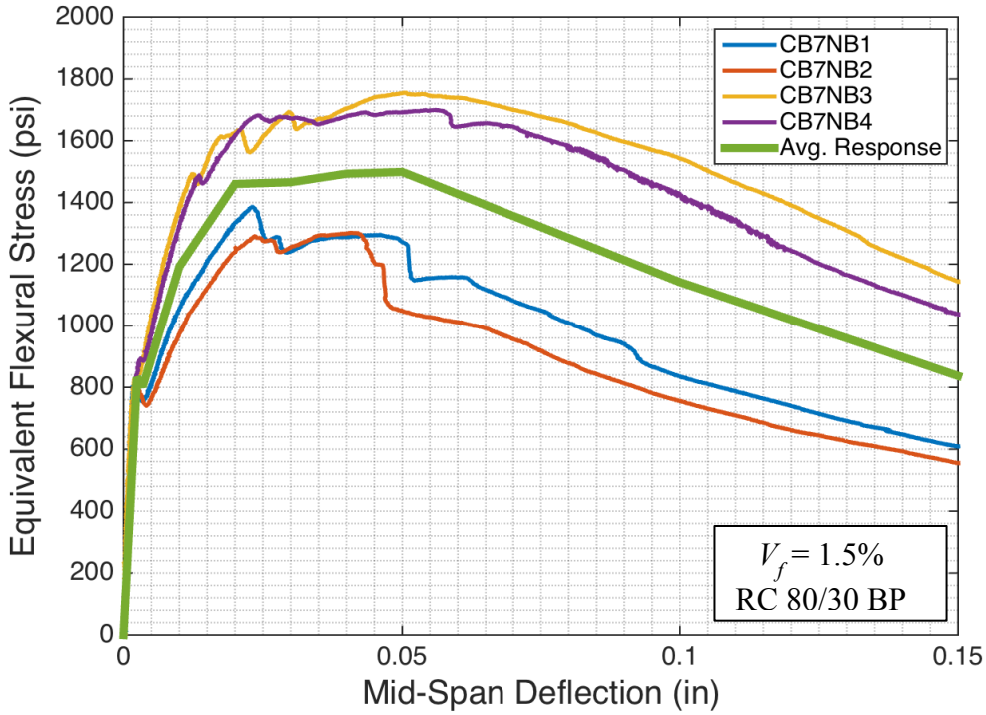


**Figure 3.7: Stress versus Deflection Response (Notched Beams Corresponding to CB7)**

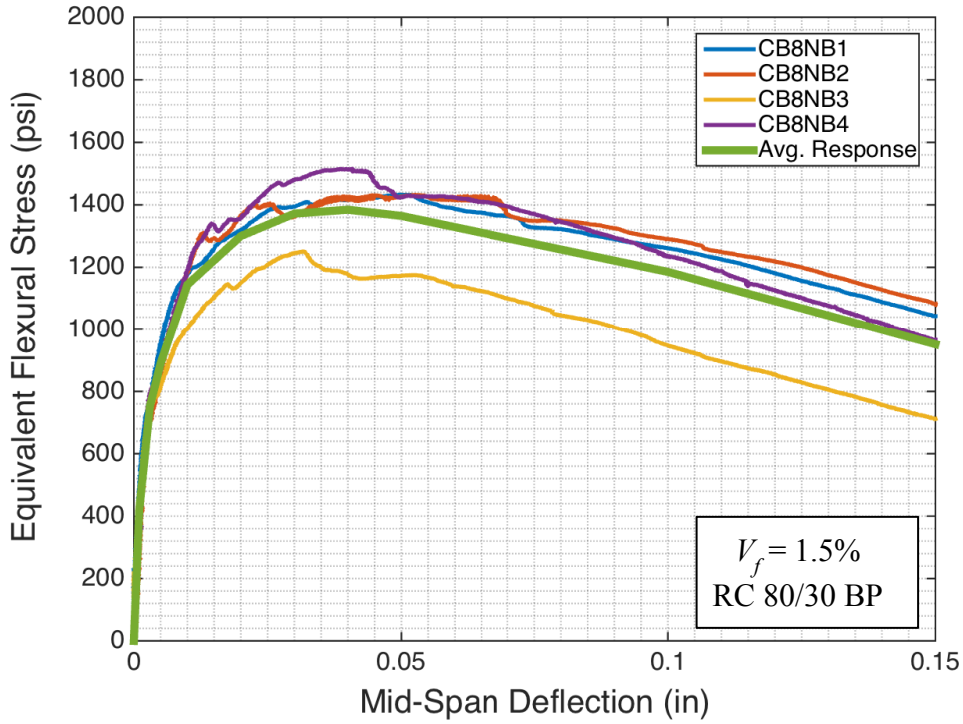


**Figure 3.8: Stress versus Deflection Response (Notched Beams Corresponding to CB8)**

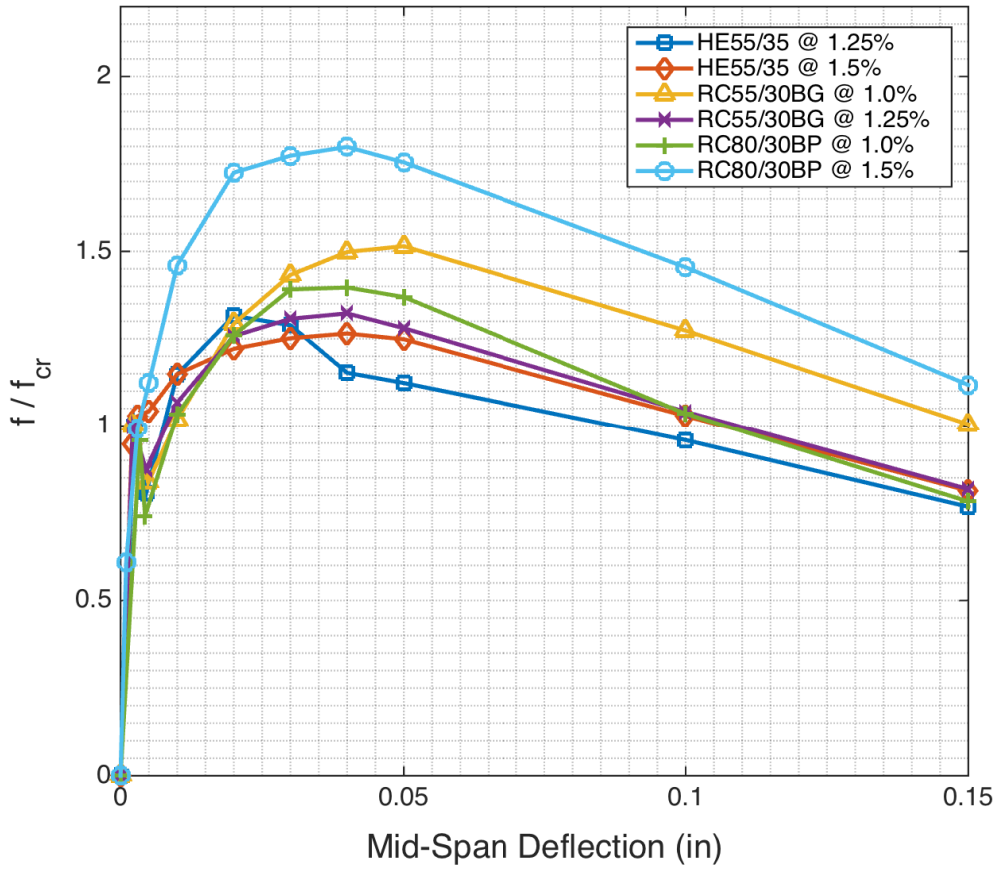


**Figure 3.9: Normalized Stress versus Deflection Response of FRC Notched Beams**

In general, the flexural behavior of FRC notched beams was characterized by a linear elastic portion followed by a drop in strength right after first cracking, a non-linear deflection hardening region, and a nearly linear descending or softening branch. The FRCs with a volume fraction of 1.5% may or may not have exhibited the drop in strength after first cracking. On average, all the FRCs considered in this study exhibited significant deflection hardening when tested using notched beams. The best behavior was exhibited by the specimens with RC 80/30 BP fibers in a 1.5% volume fraction. This was expected, as these fibers had the largest aspect ratio (80), the largest tensile strength (330 ksi), and have the smallest diameter (0.015 in.) compared to the other two types of fibers investigated.

Two measures of ductility were used to further evaluate the behavior of the FRCs: 1) a peak strength ductility ($\mu_{pc}$), calculated as the ratio of the mid-span deflection at peak post-cracking

strength ($\delta_{pc}$) to the deflection at first cracking ($\delta_{cr}$); and 2) a ductility corresponding to $f = f_{cr}$ in the descending branch ($\mu_{fcr}$), calculated as the ratio of the deflection at $f = f_{cr}$ ($\delta_{fcr}$) to $\delta_{cr}$.

**Table 3.1: Notched Beam Average Response Summary**

| Fiber Type | $V_f$ | $f_{cr}$ (psi) | $f_{pc}$ (psi) | $f_{pc}/f_{cr}$ | $\delta_{cr}$ (in.) | $\delta_{pc}$ (in.) | $\delta_{fcr}$ (in.) | $\mu_{pc} = \delta_{pc}/\delta_{cr}$ | $\mu_{fcr} = \delta_{fcr}/\delta_{cr}$ |
|---|---|---|---|---|---|---|---|---|---|
| HE 55/35 | 1.25% | 730 | 960 | 1.31 | 0.0025 | 0.020 | 0.087 | 8 | 35 |
| HE 55/35 | 1.50% | 780 | 980 | 1.27 | 0.0030 | 0.040 | 0.107 | 13 | 36 |
| RC 55/30 BG | 1.00% | 650 | 990 | 1.51 | 0.0022 | 0.050 | 0.150 | 23 | 68 |
| RC 55/30 BG | 1.25% | 700 | 930 | 1.32 | 0.0022 | 0.040 | 0.109 | 18 | 50 |
| RC 80/30 BP | 1.00% | 760 | 1060 | 1.40 | 0.0034 | 0.040 | 0.107 | 12 | 31 |
| RC 80/30 BP | 1.50% | 800 | 1440 | 1.80 | 0.0030 | 0.040 | 0.168* | 13 | 56 |

* Linearly extrapolated assuming a constant descending branch slope beyond a deflection of 0.15in.

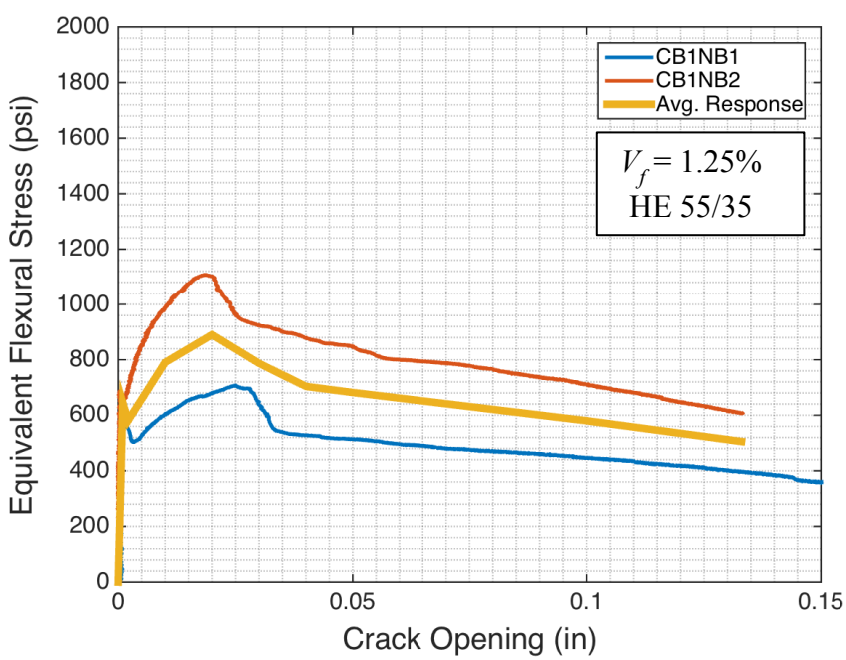


**Figure 3.10: Stress versus Crack Opening Response (Notched Beams Corresponding to CB1)**

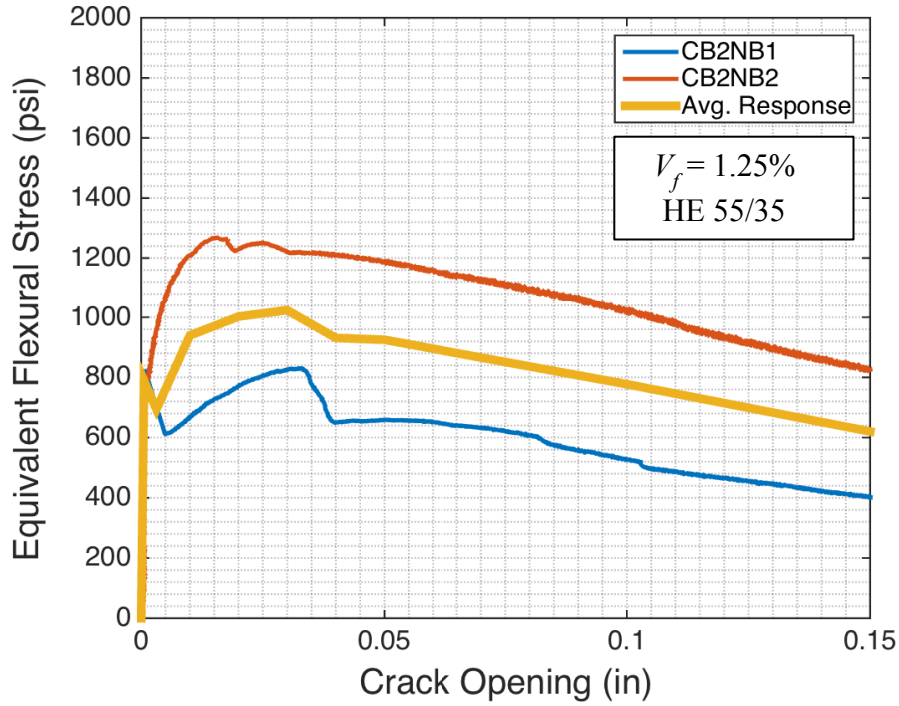


**Figure 3.11: Stress versus Crack Opening Response (Notched Beams Corresponding to CB2)**

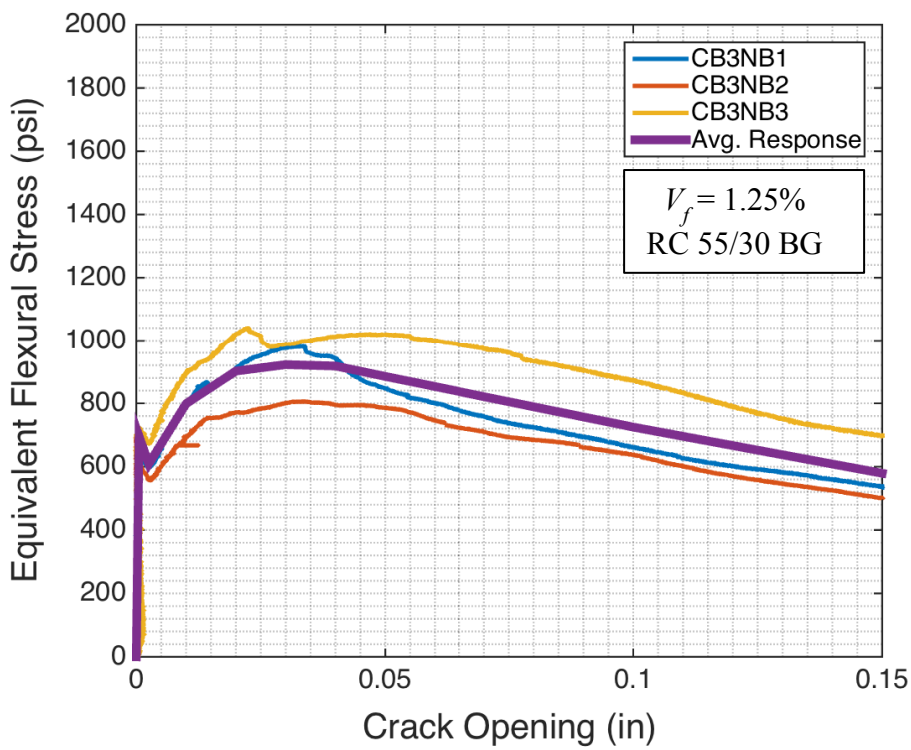


**Figure 3.12: Stress versus Crack Opening Response (Notched Beams Corresponding to CB3)**

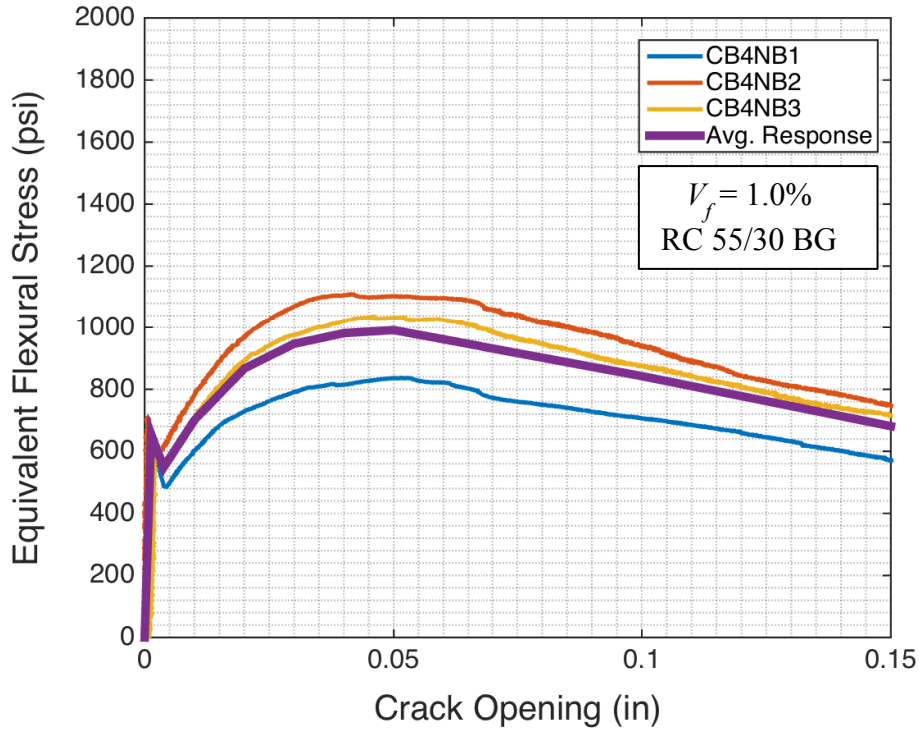


**Figure 3.13: Stress versus Crack Opening Response (Notched Beams Corresponding to CB4)**

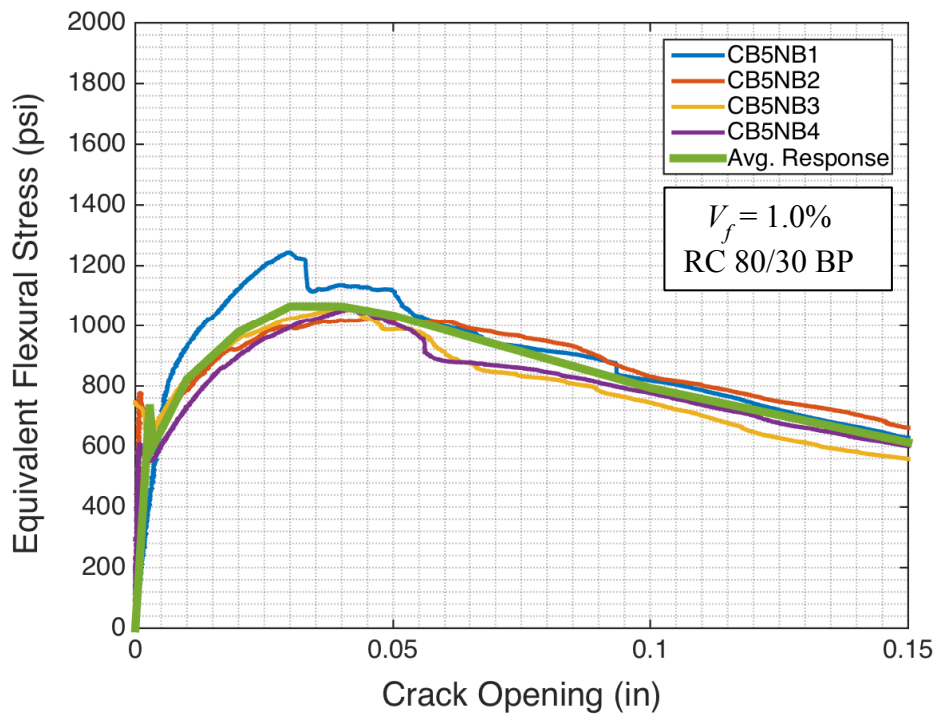


**Figure 3.14: Stress versus Crack Opening Response (Notched Beams Corresponding to CB5)**

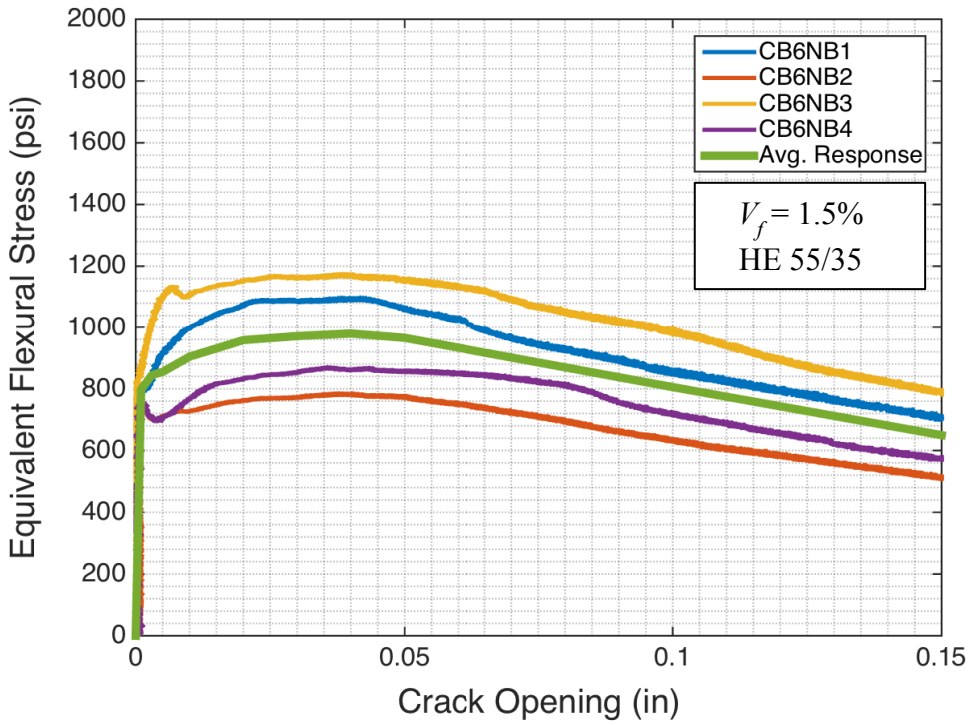


**Figure 3.15: Stress versus Crack Opening Response (Notched Beams Corresponding to CB6)**

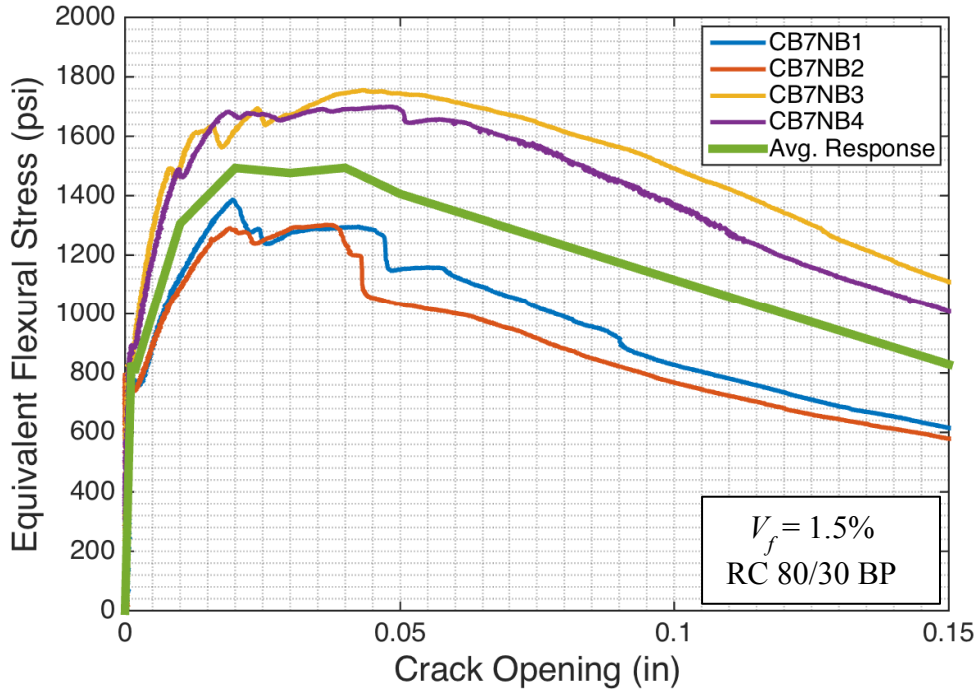


**Figure 3.16: Stress versus Crack Opening Response (Notched Beams Corresponding to CB7)**

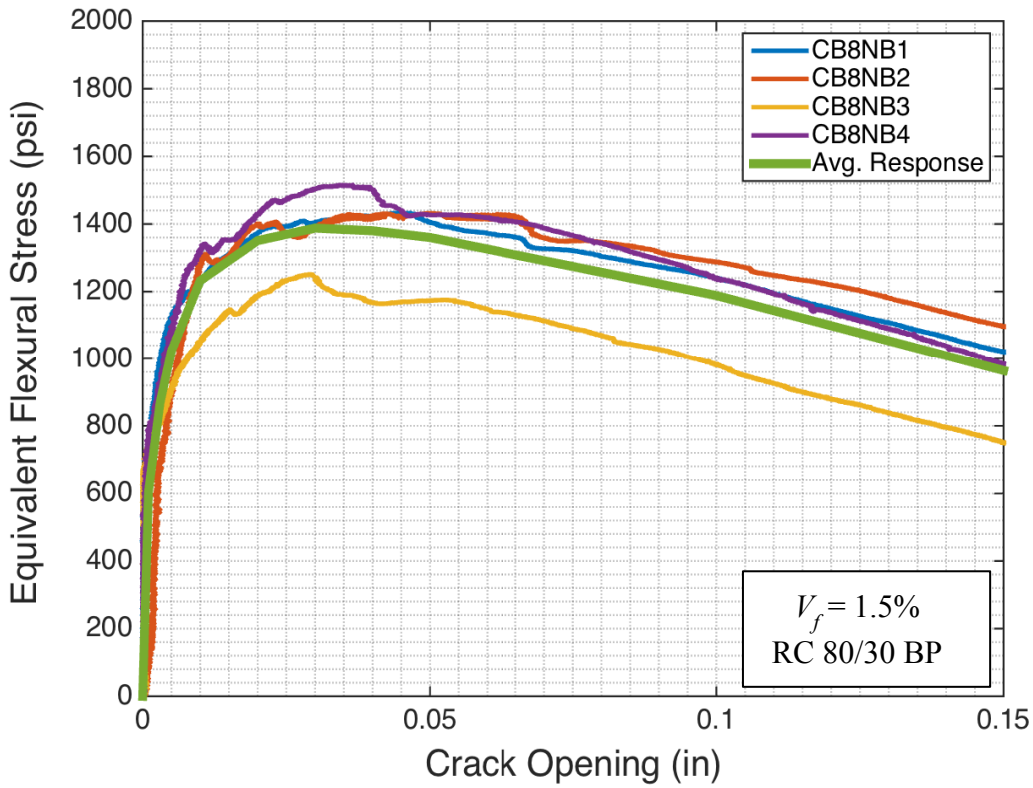


**Figure 3.17: Stress versus Crack Opening Response (Notched Beams Corresponding to CB8)**

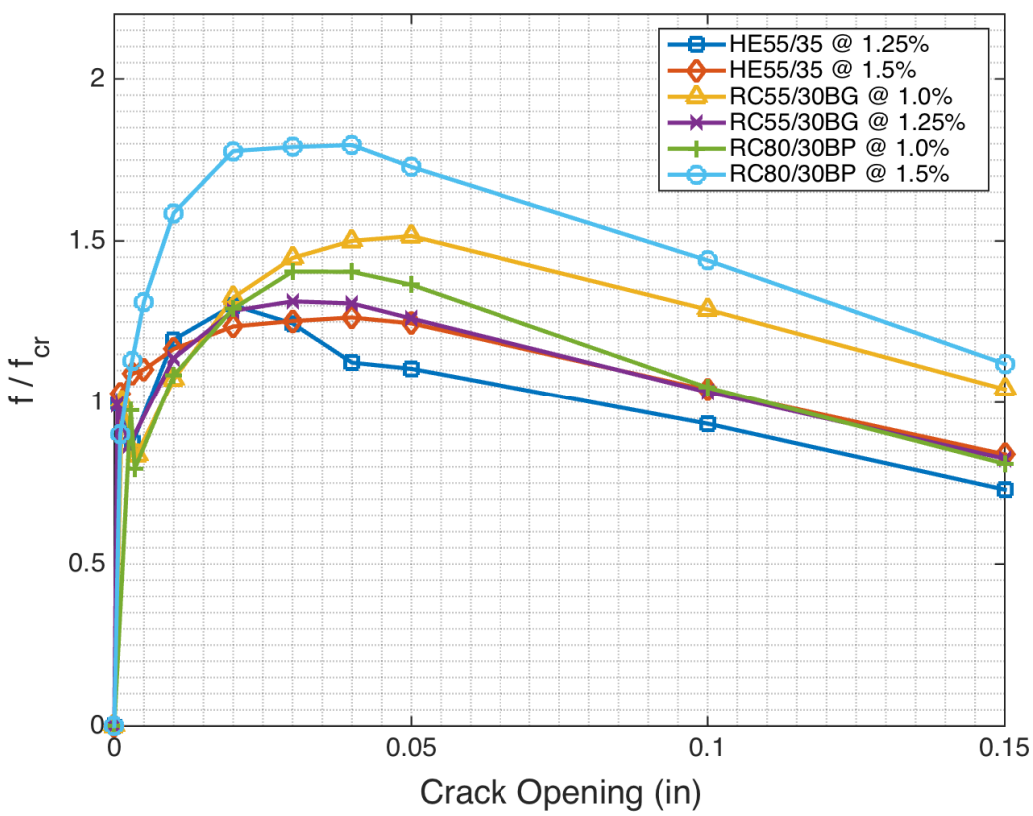


**Figure 3.18: Normalized Stress versus Crack Opening Response of FRC Notched Beams**

## 3.2 Flexural Test Results of FRC Un-notched Beams

The equivalent flexural stress versus mid-span deflection responses for all the un-notched beams tested are shown in Figure 3.19 through Figure 3.27. As for the notched beams, the equivalent bending stresses were calculated using Equation 16. It must be noted that the average response presented for the specimens corresponding to Coupling Beams CB1 and CB2 excludes Specimen CB1B2 and CB2B1, respectively. These specimens were eliminated from the average response calculation due to their considerably different behavior, which was considered not to be representative of the overall material behavior (see Figure 3.19 and Figure 3.20). The reason for such different behavior, however, is not known.

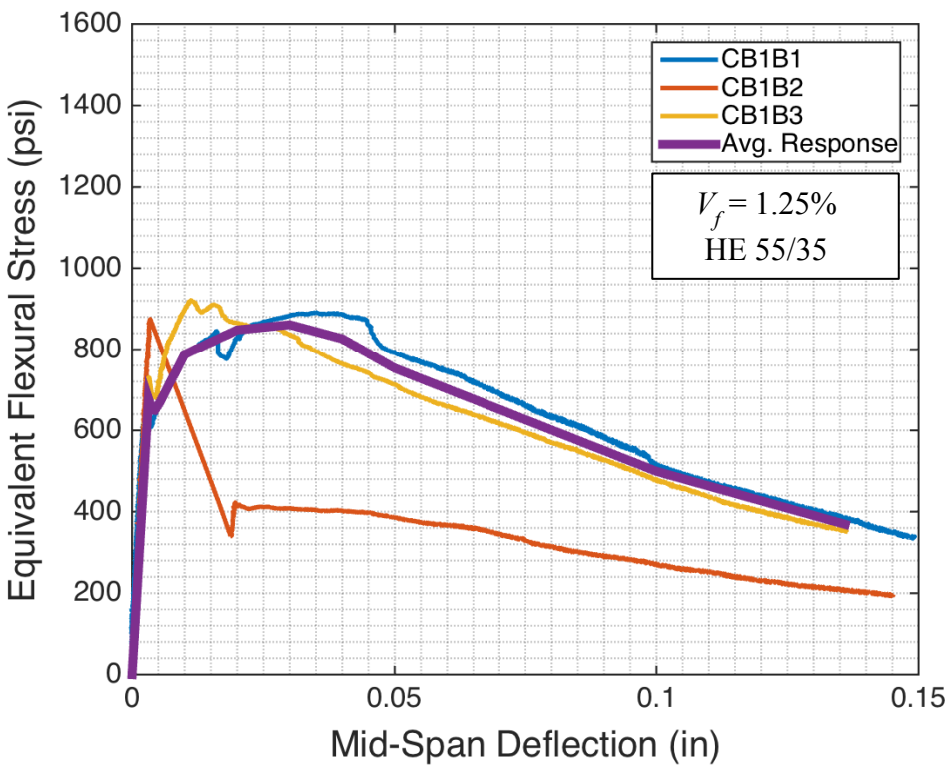


**Figure 3.19: Stress versus Deflection Response (Un-notched Beams Corresponding to CB1)**

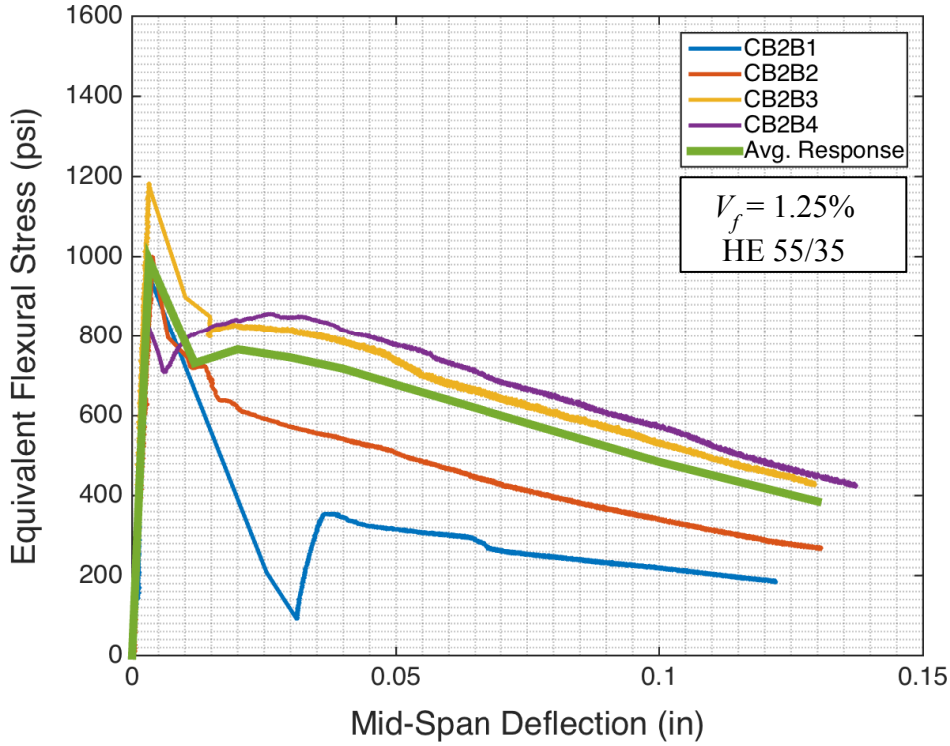


**Figure 3.20: Stress versus Deflection Response (Un-notched Beams Corresponding to CB2)**

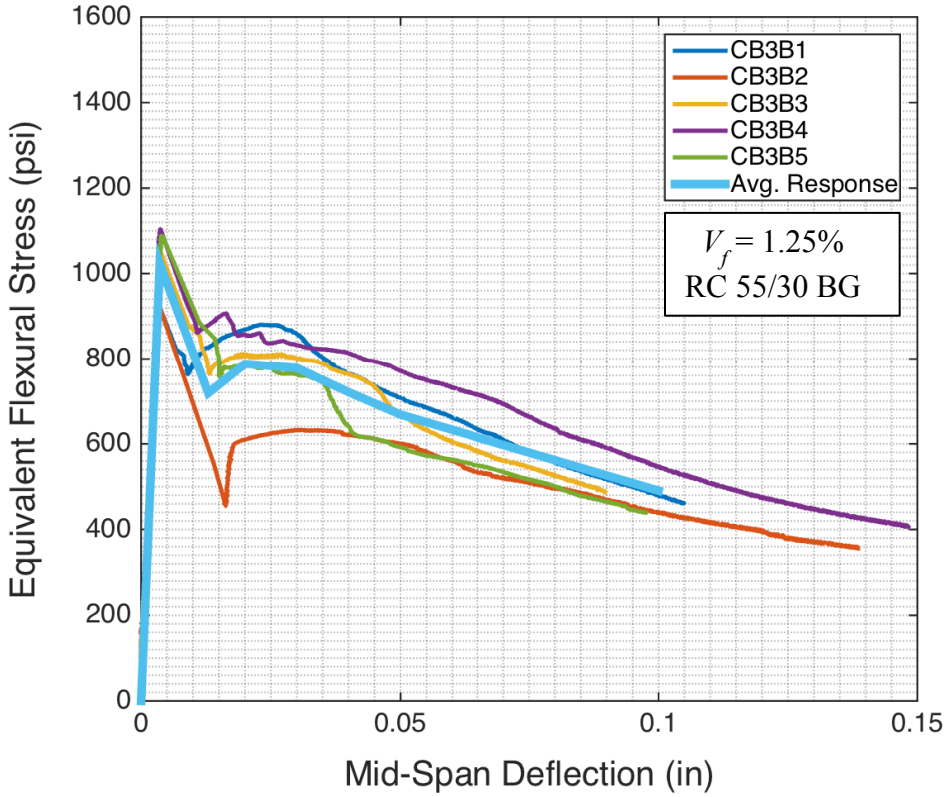


**Figure 3.21: Stress versus Deflection Response (Un-notched Beams Corresponding to CB3)**

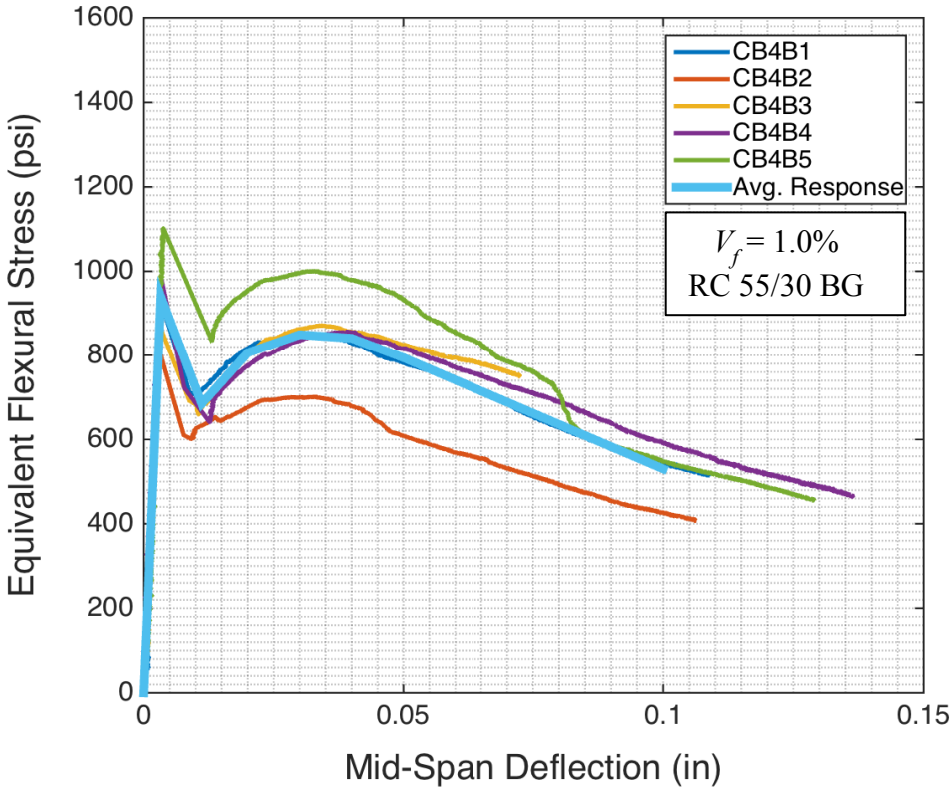


**Figure 3.22: Stress versus Deflection Response (Un-notched Beams Corresponding to CB4)**

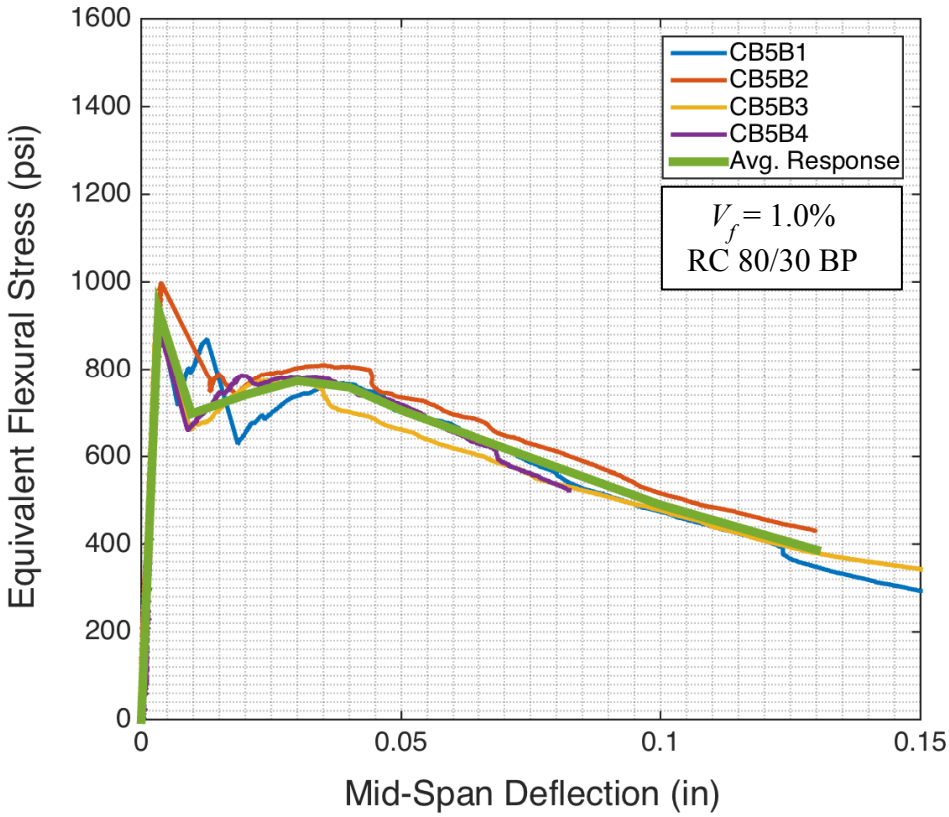


**Figure 3.23: Stress versus Deflection Response (Un-notched Beams Corresponding to CB5)**

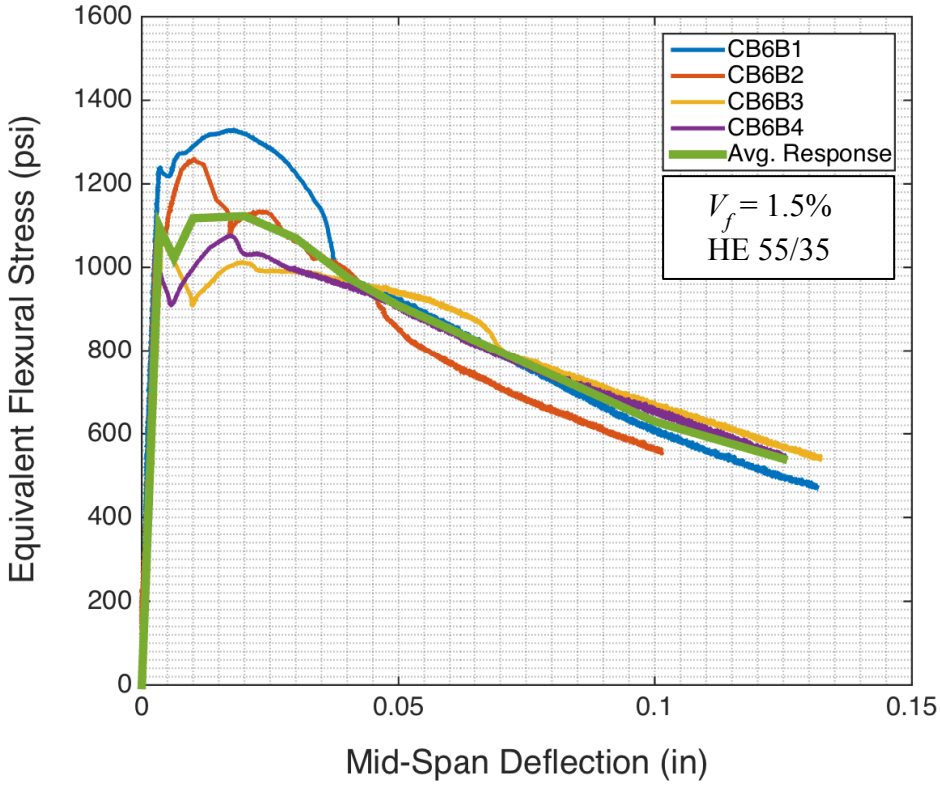


**Figure 3.24: Stress versus Deflection Response (Un-notched Beams Corresponding to CB6)**

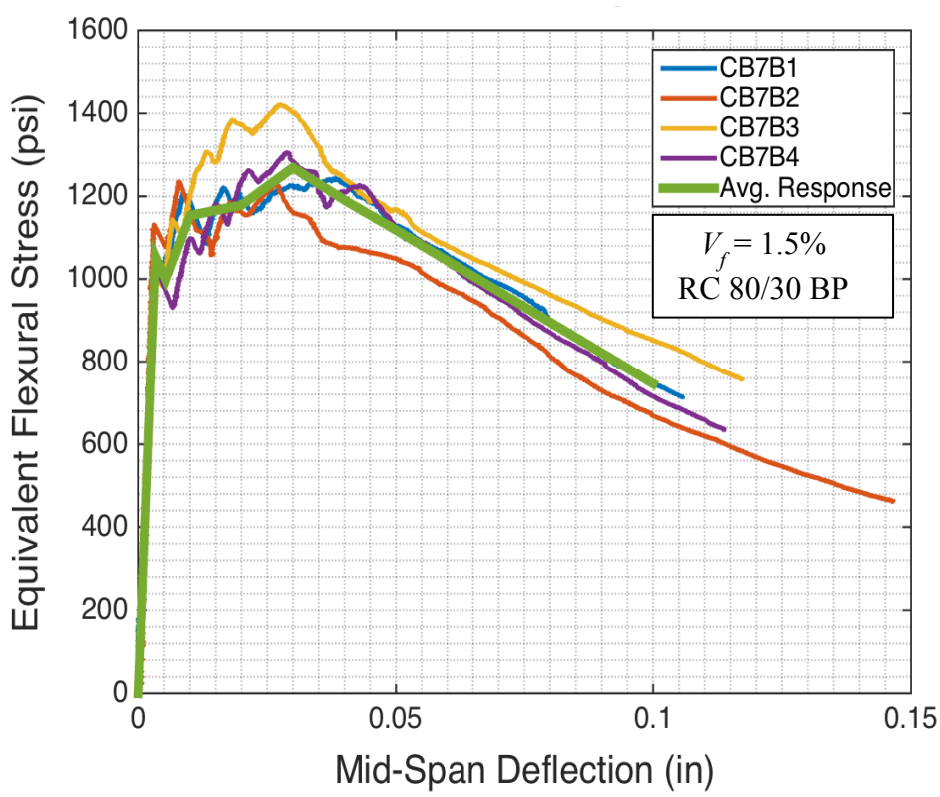


**Figure 3.25: Stress versus Deflection Response (Un-notched Beams Corresponding to CB7)**

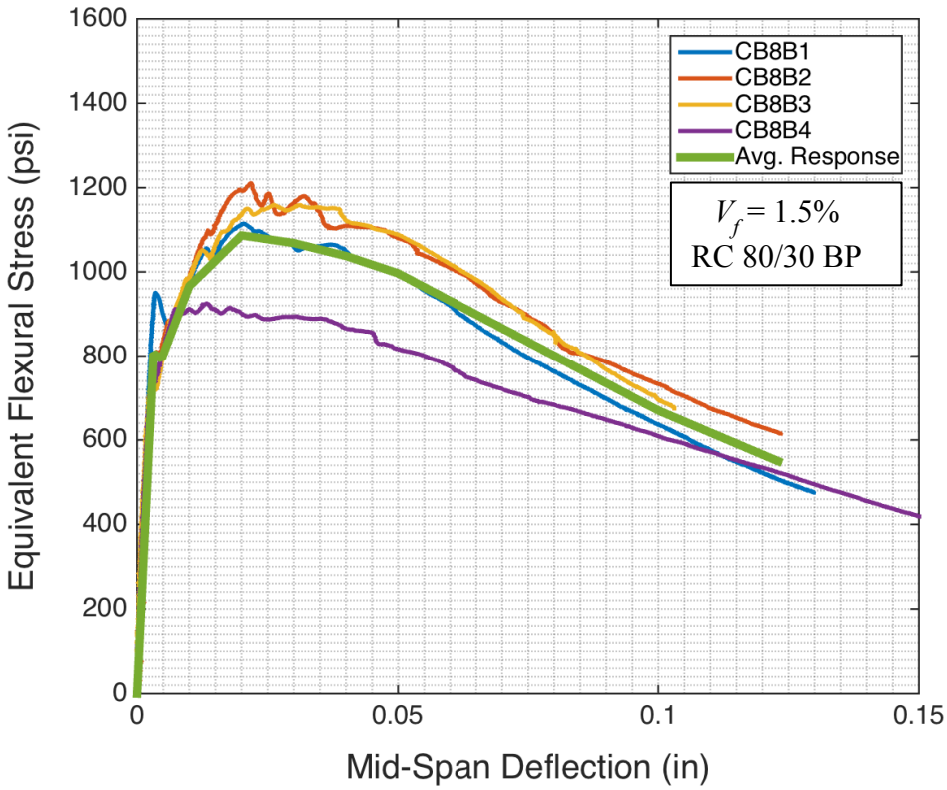


**Figure 3.26: Stress versus Deflection Response (Un-notched Beams Corresponding to CB8)**

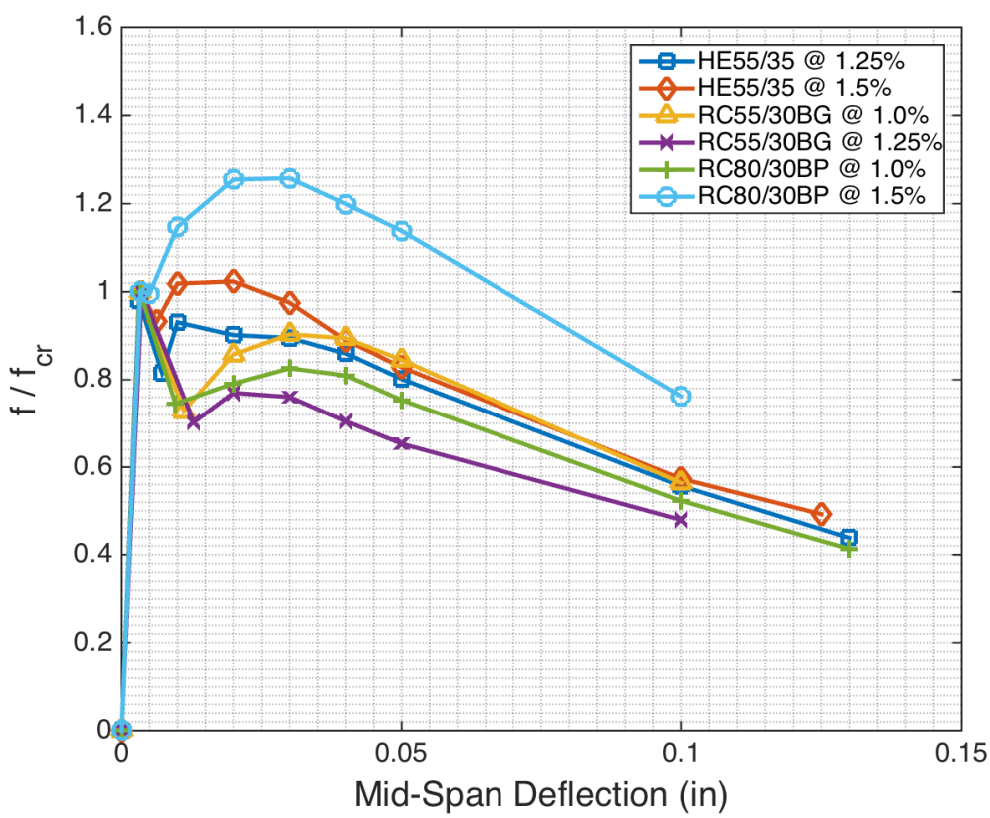


**Figure 3.27: Normalized Stress versus Deflection Response of FRC Un-notched Beams**

In general, FRCs with a fiber volume fraction of 1.25% and 1.0% exhibited strength recovery of approximately 80% of the first cracking strength after a strength loss right after first cracking. No deflection hardening was observed in these FRCs. On the other hand, both FRCs with a volume fraction of 1.5% exhibited deflection hardening behavior. As for the notched beams, the best behavior was exhibited by the material with RC 80/30 PB fibers in a 1.5% volume fraction. This is attributed to their higher aspect ratio and tensile strength, combined with a smaller diameter compared to the other two fibers investigated. Given the lower performance exhibited by the un-notched beams compared to the notched beams, different measures of ductility were used to evaluate the response of the un-notched beams. A ductility $\mu_{50}$ was calculated as the ratio of the mid-span deflection corresponding to a residual strength equal to 0.5 $f_{cr}$ ($\delta_{50}$) to the deflection at first cracking ($\delta_{cr}$) (see Table 3.2). To further characterize the post-cracking behavior of the FRCs the mid-span deflections corresponding to the peak post-cracking strength ($\delta_{pc}$) and to a residual strength $f = 0.75\ f_{cr}$ ($\delta_{75}$) are also presented in Table 3.2. Also included in Table 3.2 is the ratio of the equivalent flexural stress at a mid-span deflection equal to $L$ /150 (0.12 in.), $f_{150}$, to the peak post-cracking stress.

**Table 3.2: Un-notched Beams Stress-Deflection Behavior Summary**

| Fiber Type | $V_f$ | $f_{cr}$ (psi) | $f_{pc}$ (psi) | $f_{pc}/f_{cr}$ | $f_{150}/f_{pc}$ | $\delta_{cr}$ (in.) | $\delta_{pc}$ (in.) | $\delta_{75}$ (in.) | $\delta_{50}$ (in) | $\mu_{50}$ |
|---|---|---|---|---|---|---|---|---|---|---|
| HE 55/35 | 1.25% | 890 | 825 | 0.93 | 0.44 | 0.0032 | 0.010 | 0.050 | 0.114 | 36 |
| HE 55/35 | 1.50% | 1100 | 1140 | 1.04 | 0.49 | 0.0034 | 0.020 | 0.065 | 0.122 | 36 |
| RC 55/30 BG | 1.00% | 940 | 850 | 0.90 | 0.60 | 0.0033 | 0.030 | 0.070 | 0.111* | 34 |
| RC 55/30 BG | 1.25% | 1020 | 790 | 0.77 | 0.54 | 0.0036 | 0.020 | 0.030 | 0.094 | 26 |
| RC 80/30 BP | 1.00% | 940 | 775 | 0.82 | 0.54 | 0.0033 | 0.030 | 0.050 | 0.106 | 32 |
| RC 80/30 BP | 1.50% | 930 | 1170 | 1.26 | 0.49 | 0.0034 | 0.030 | 0.100 | 0.135* | 40 |

* Linearly extrapolated assuming the descending branch slope is constant beyond a deflection of 0.15 in

In order to further evaluate the flexural behavior of the FRCs given that the un-notched specimens cracked at different locations within the middle third of the span, Figure 3.28 through Figure 3.36 show the flexural response of each of the FRCs in terms of equivalent flexural stresses versus crack opening (see Equation 8).

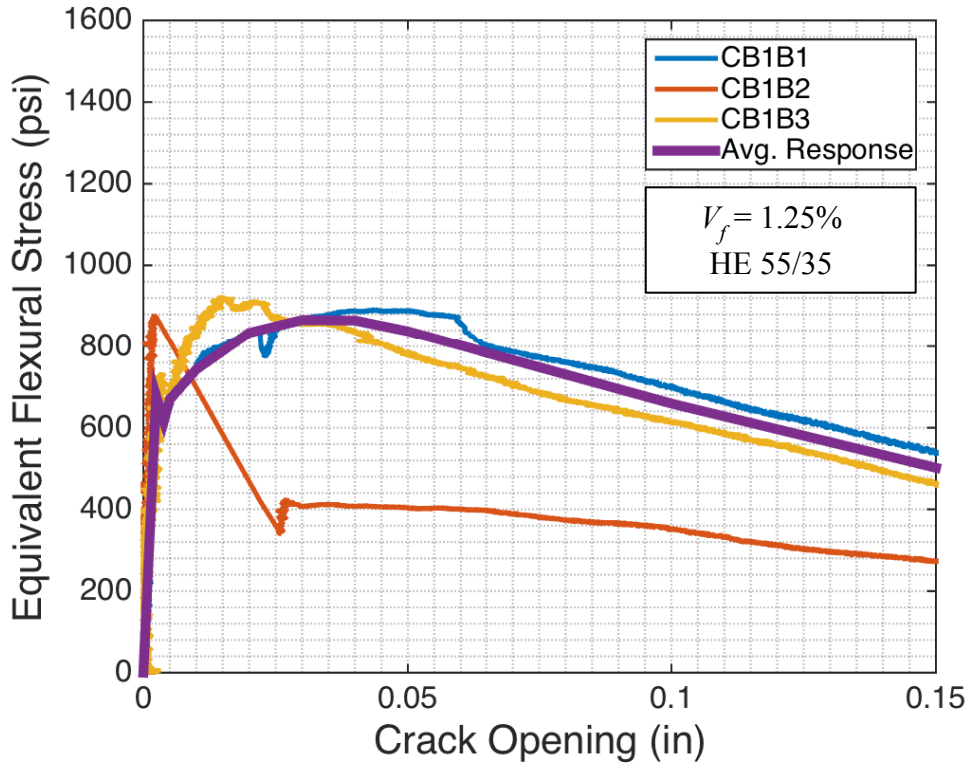


**Figure 3.28: Stress versus Crack Opening Response (Un-notched Beams Corresponding to CB1)**

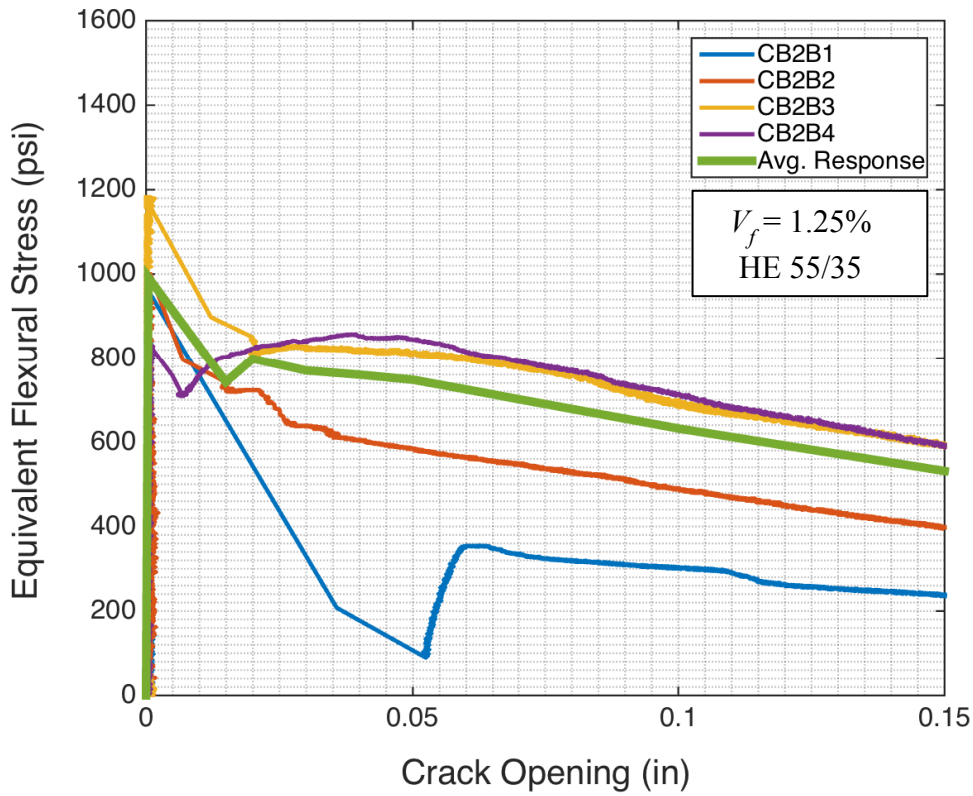


**Figure 3.29: Stress versus Crack Opening Response (Un-notched Beams Corresponding to CB2)**

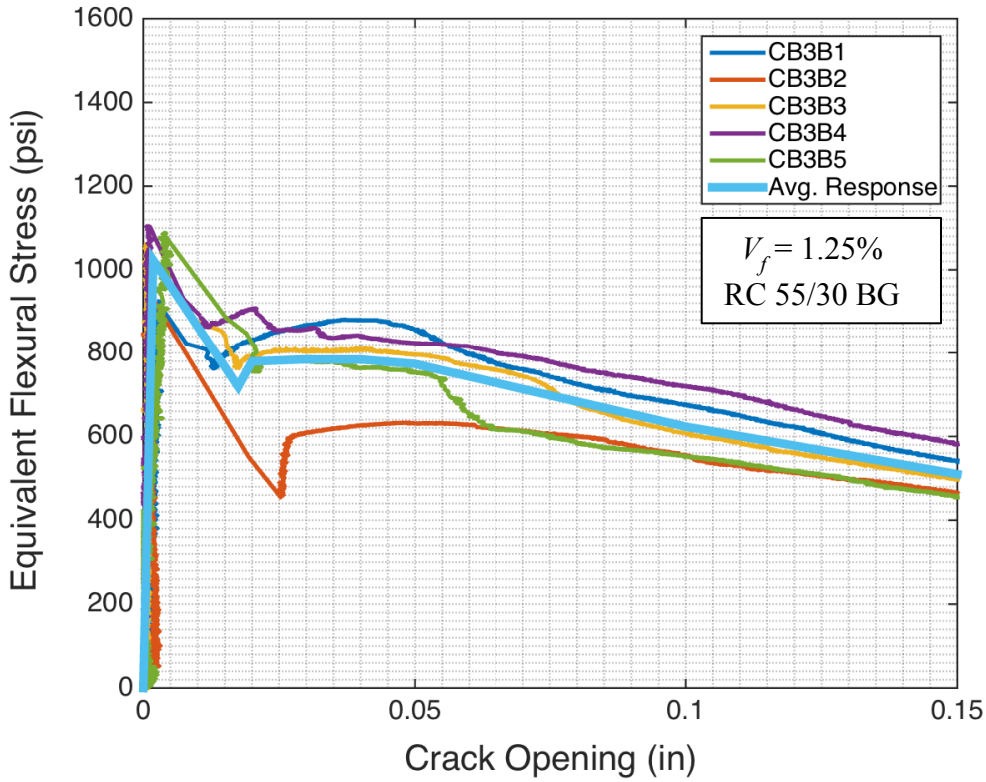


**Figure 3.30: Stress versus Crack Opening Response (Un-notched Beams Corresponding to CB3)**

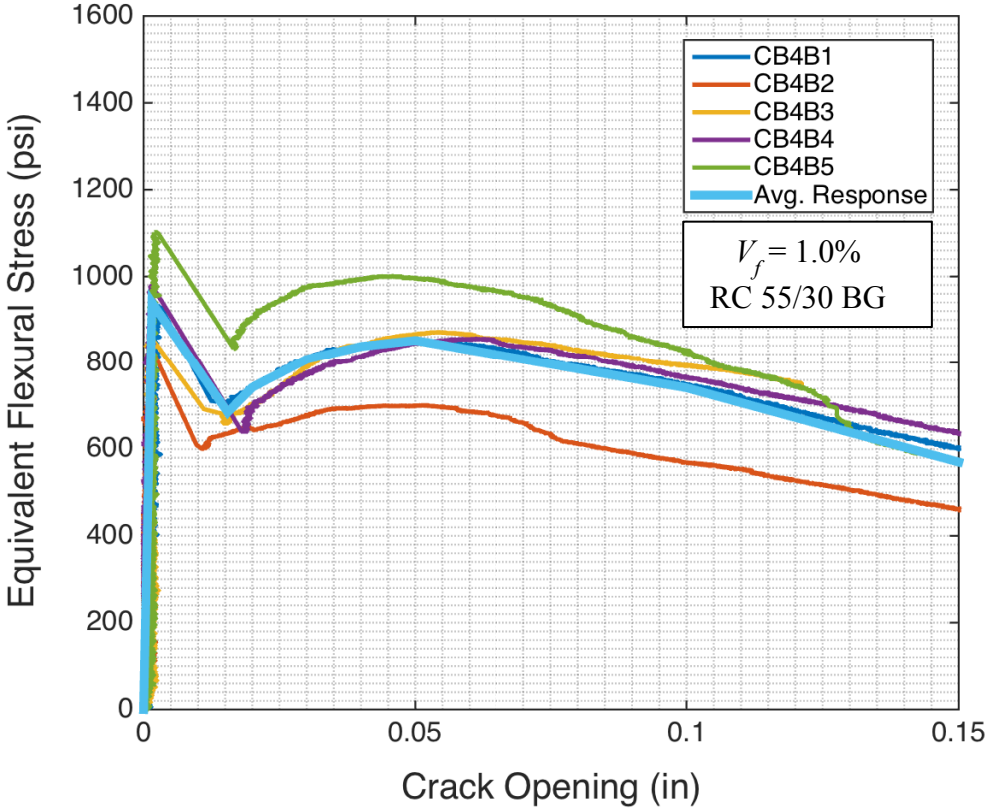


**Figure 3.31: Stress versus Crack Opening Response (Un-notched Beams Corresponding to CB4)**

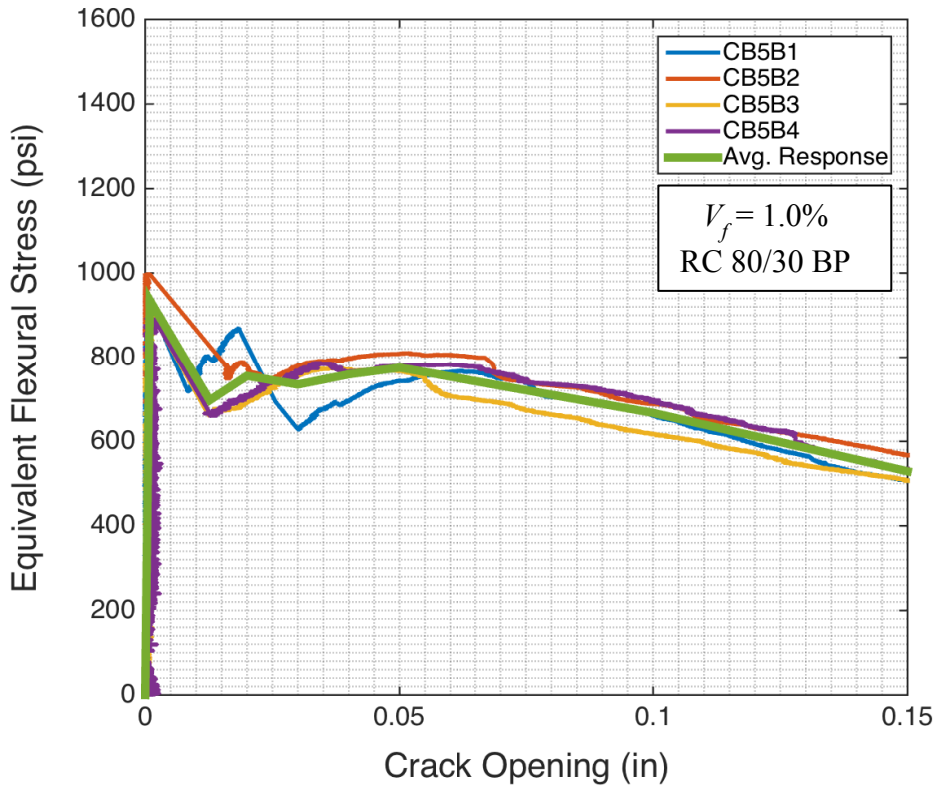


**Figure 3.32: Stress versus Crack Opening Response (Un-notched Beams Corresponding to CB5)**

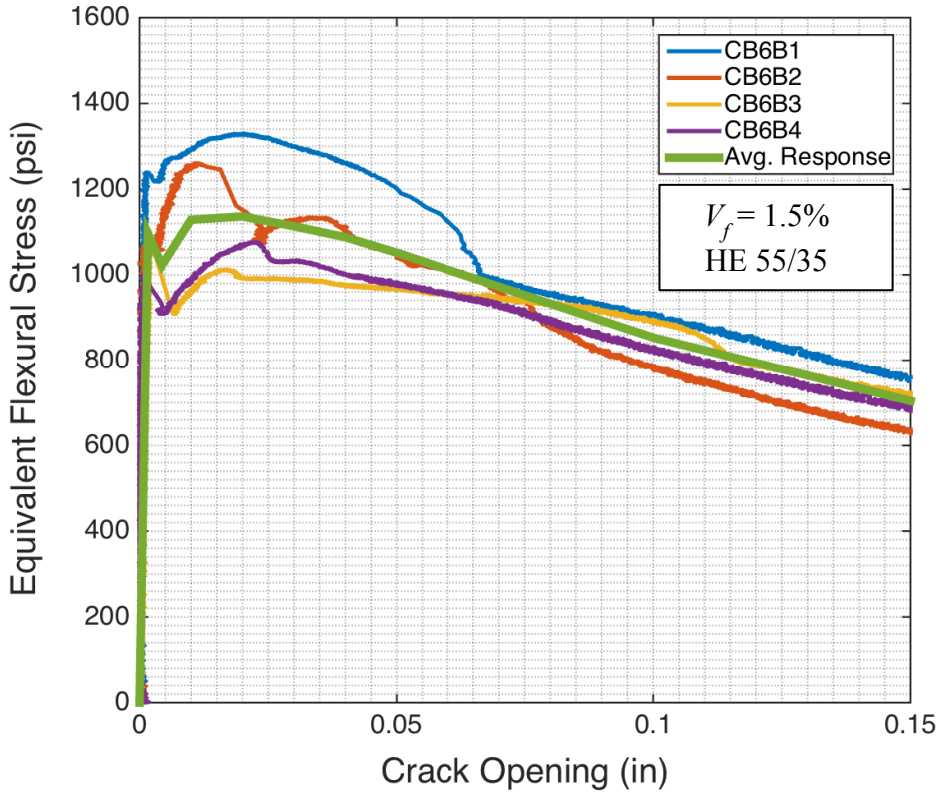


**Figure 3.33: Stress versus Crack Opening Response (Un-notched Beams Corresponding to CB6)**

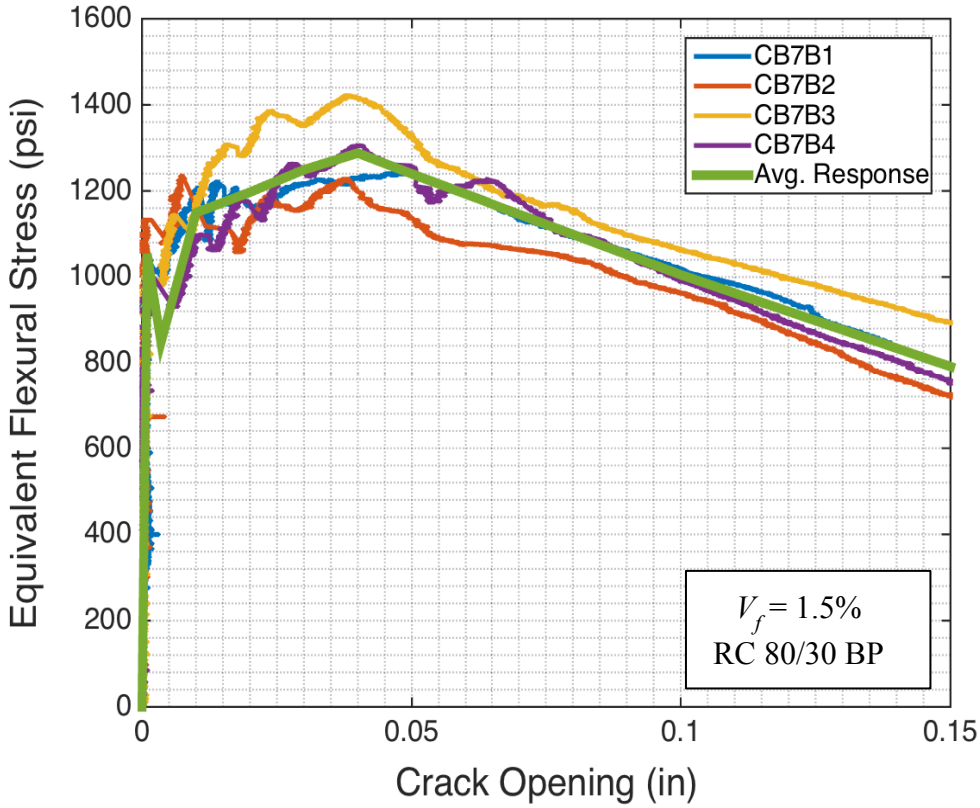


**Figure 3.34: Stress versus Crack Opening Response (Un-notched Beams Corresponding to CB7)**

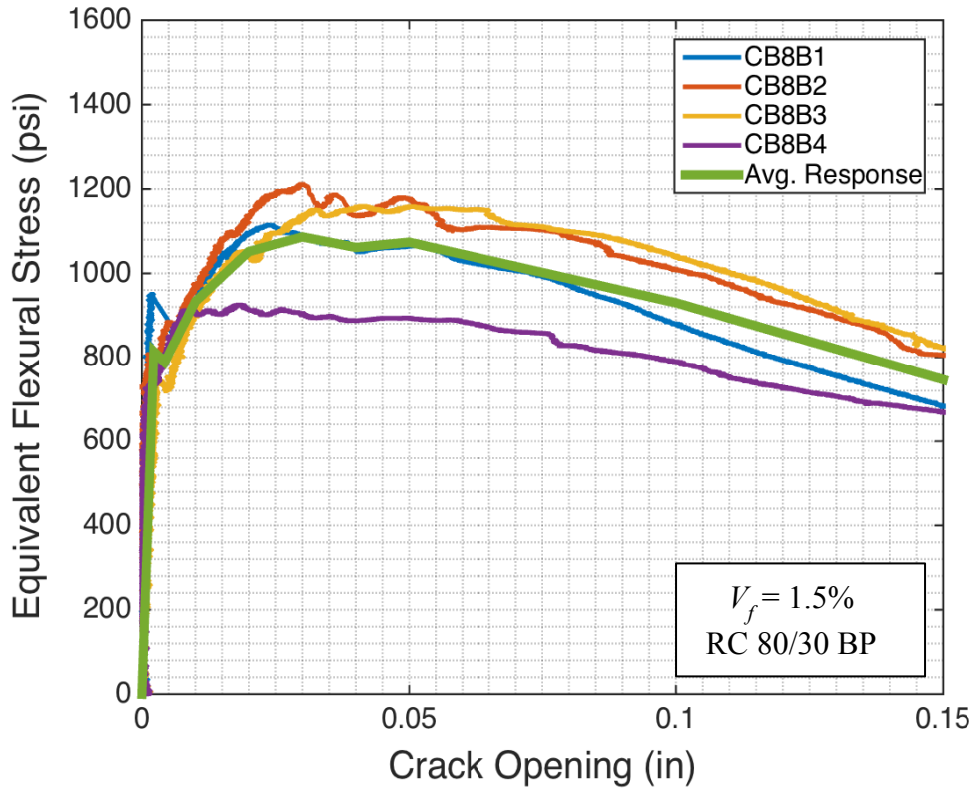


**Figure 3.35: Stress versus Crack Opening Response (Un-notched Beams Corresponding to CB8)**

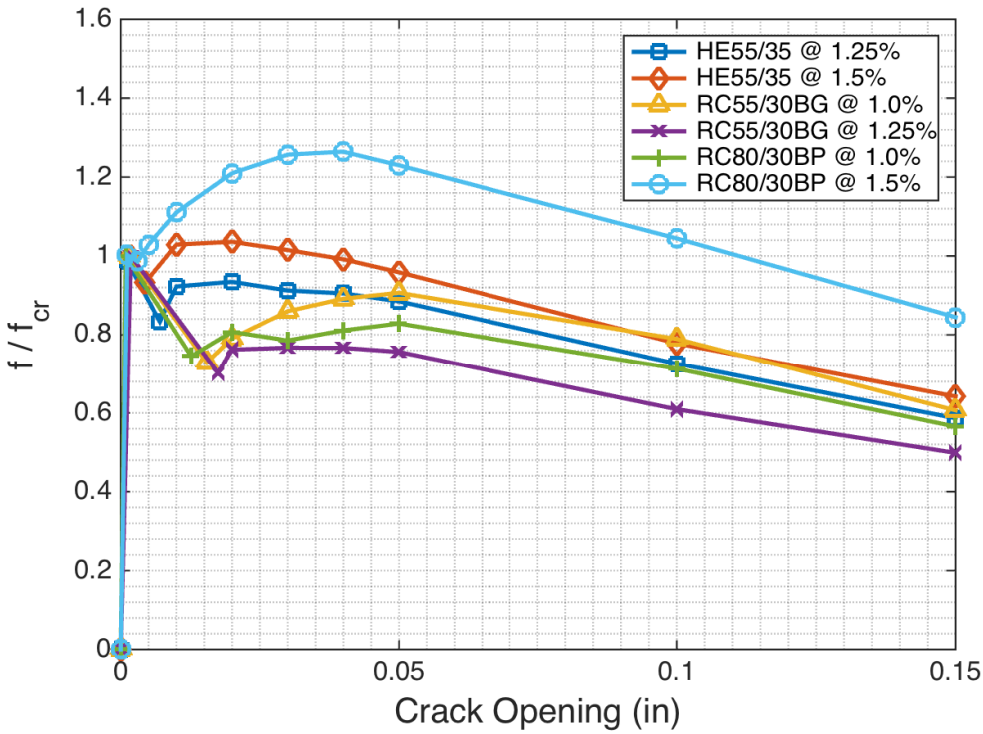


**Figure 3.36: Normalized Stress versus Crack Opening Response of FRC Beams**

It should be noted that the FRC with RC 55/30 BG fibers at a 1.0% volume fraction exhibited a slightly better behavior than the FRC that was cast using the same fibers at a 1.25% volume fraction, which was unexpected. The amount of fibers in each beam specimen for these two concretes were counted and, as expected, the FRC with the higher volume fraction had more fibers crossing the failure surface than the FRC with a $V_f$ = 1.0%. It is thus not clear why the FRC with the lower fiber dosage exhibited a slightly better behavior. Table 3.3 presents a summary of the flexural behavior of the un-notched FRC beams in terms of crack widths.

Comparing the behavior of the FRCs between notched and un-notched bending tests, the following observations can be made:

- The un-notched bending tests showed that only the FRCs with $V_f$ = 1.5% exhibited deformation hardening behavior, whereas all the FRCs exhibited deformation hardening behavior when evaluated through notched beam tests.
- The flexural behavior of the FRC cast with RC 80/30 BP fibers at $V_f$ = 1.5% outperformed all other FRCs in both notched and un-notched beam tests. This was

expected given the fact that among the three fibers investigated, the RC 80/30 BP fibers had the highest aspect ratio and tensile strength, as well as the smallest diameter.

- Both FRCs cast with HE 55/35 fibers, when compared to the rest of the FRCs (excluding the FRC cast with RC 80/30 BP at $V_f$ = 1.5%), exhibited a slightly better behavior in the un-notched beam tests. However, these FRCs were slightly outperformed in the notched beam tests. The reason for this apparent change in performance is not known.
- In general, all of the FRCs except for those with RC 80/30 BP fibers at $V_f$ = 1.5% exhibited a fairly similar flexural behavior for both notched and un-notched beam tests.

**Table 3.3: Un-notched Beams Flexural Behavior Summary**

| Fiber Type | $V_f$ | $f_{cr}$ (psi) | $f_{pc}$ (psi) | $f_{pc}/f_{cr}$ | $w_{cr}$ (in) | $w_{pc}$ (in) | $w_{75}$ (in) | $w_{50}$ (in) | $\mu_{50}$ |
|---|---|---|---|---|---|---|---|---|---|
| HE 55/35 | 1.25% | 890 | 830 | 0.93 | 0.0016 | 0.040 | 0.072 | 0.181* | 115 |
| HE 55/35 | 1.50% | 1100 | 1140 | 1.04 | 0.0016 | 0.020 | 0.110 | 0.202* | 126 |
| RC 55/30 BG | 1.00% | 940 | 850 | 0.90 | 0.0015 | 0.050 | 0.111 | 0.179* | 116 |
| RC 55/30 BG | 1.25% | 1020 | 790 | 0.77 | 0.0018 | 0.030 | 0.052 | 0.149 | 82 |
| RC 80/30 BP | 1.00% | 940 | 775 | 0.82 | 0.0009 | 0.050 | 0.084 | 0.174* | 193 |
| RC 80/30 BP | 1.50% | 930 | 1170 | 1.26 | 0.0011 | 0.040 | 0.174* | 0.236* | 206 |

* Linearly extrapolated assuming the descending branch slope is constant beyond a crack opening of 0.15 in.

## 3.3 FRC Tensile Test Results

The tensile behavior of the FRCs considered in this study was characterized by a linear elastic region up to first cracking, at which point there was a sudden drop in strength followed by some strength recovery (in some cases the post-cracking strength was greater than the cracking strength), and ending with a softening branch. The amount of recovery observed varied significantly with the fiber content of the FRC. The FRCs with volume fractions of 1.0% and 1.25% recovered at least 50% of the first cracking strength, while those with a volume fraction of 1.5% recovered significantly more or exhibited tension-hardening behavior. Figure 3.37 through Figure 3.44 show the tensile response of each of the samples tested corresponding to the FRC used in each of the coupling beam specimens.

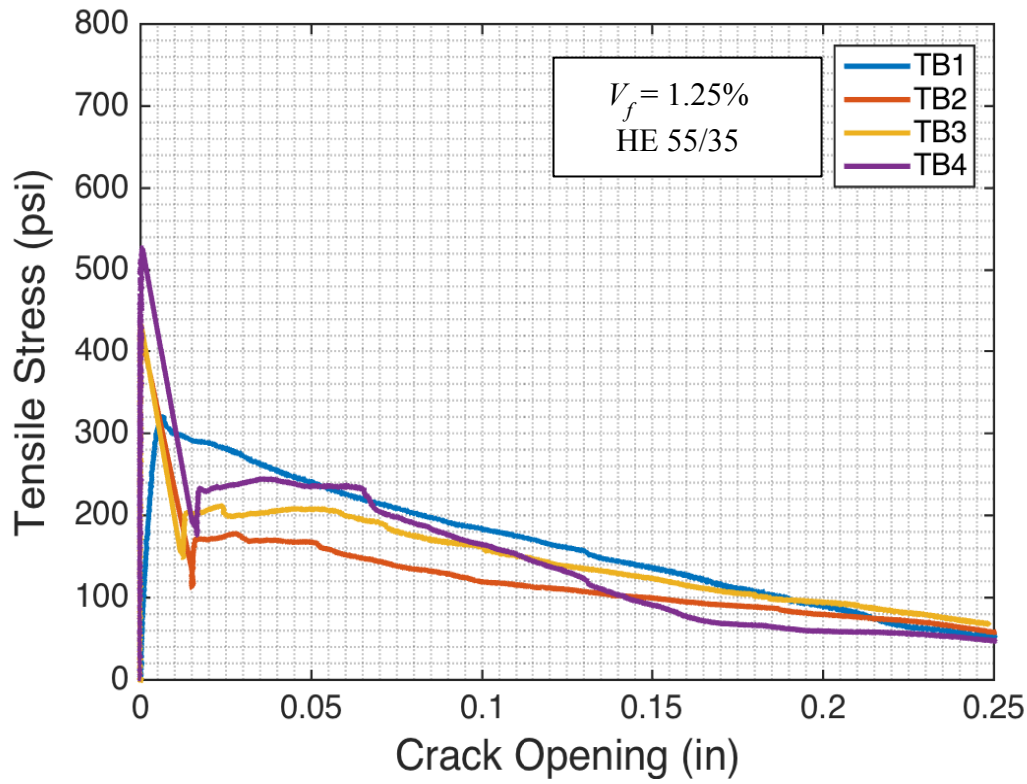


**Figure 3.37: Tensile stress versus Crack Opening Response (Tension Specimens Corresponding to CB1)**

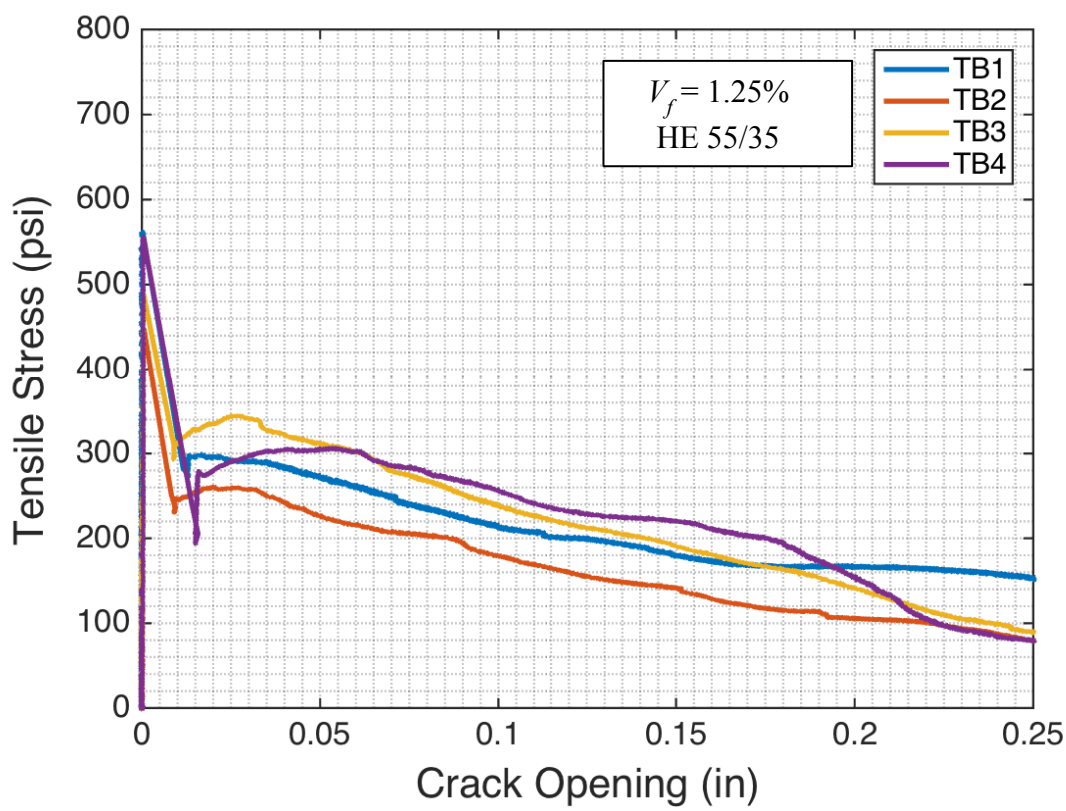


**Figure 3.38: Tensile stress versus Crack Opening Response (Tension Specimens Corresponding to CB2)**

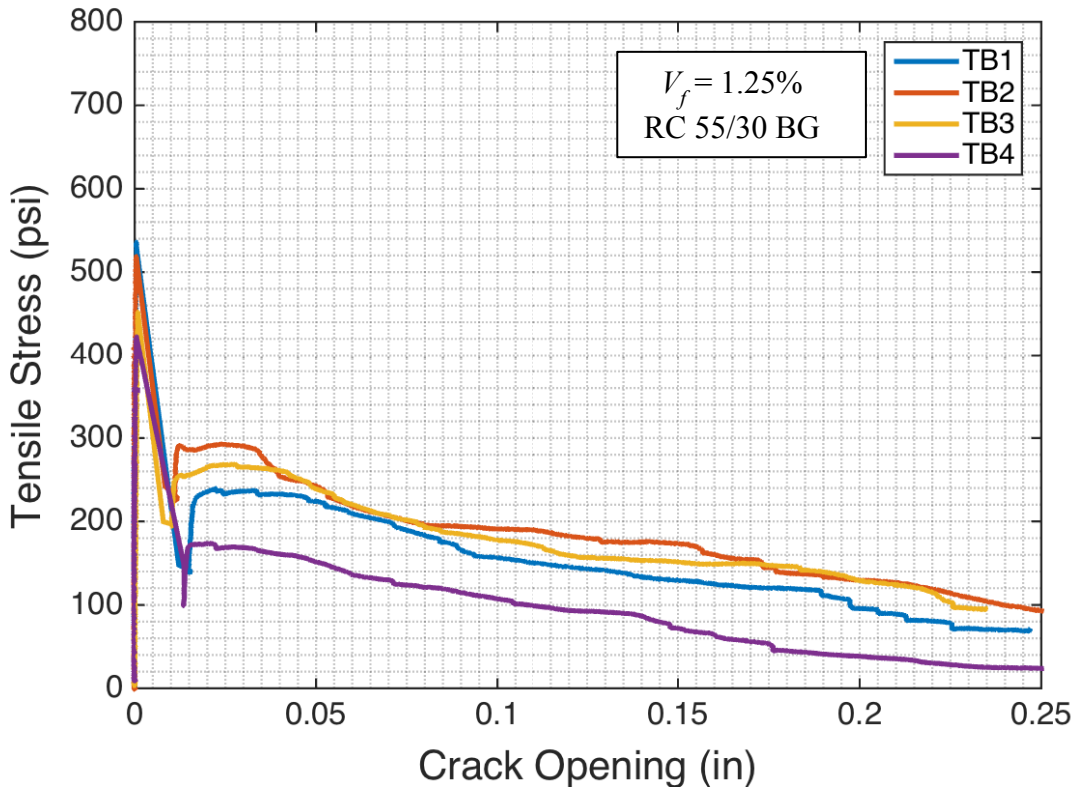


**Figure 3.39: Tensile stress versus Crack Opening Response (Tension Specimens Corresponding to CB3)**

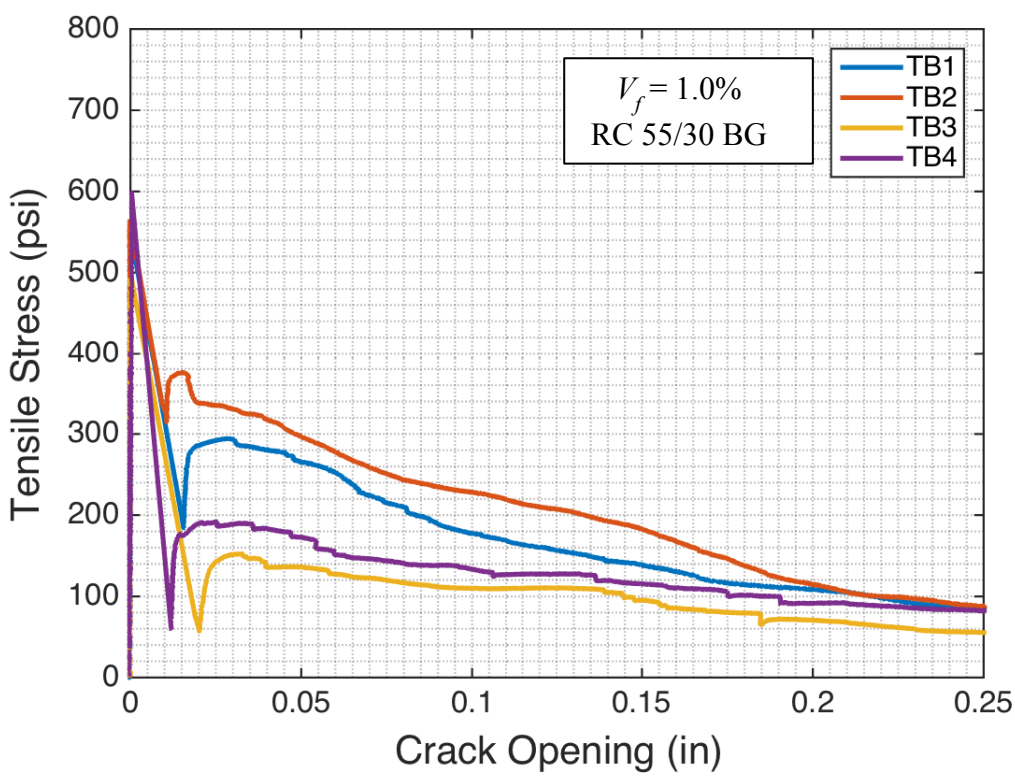


**Figure 3.40: Tensile stress versus Crack Opening Response (Tension Specimens Corresponding to CB4)**

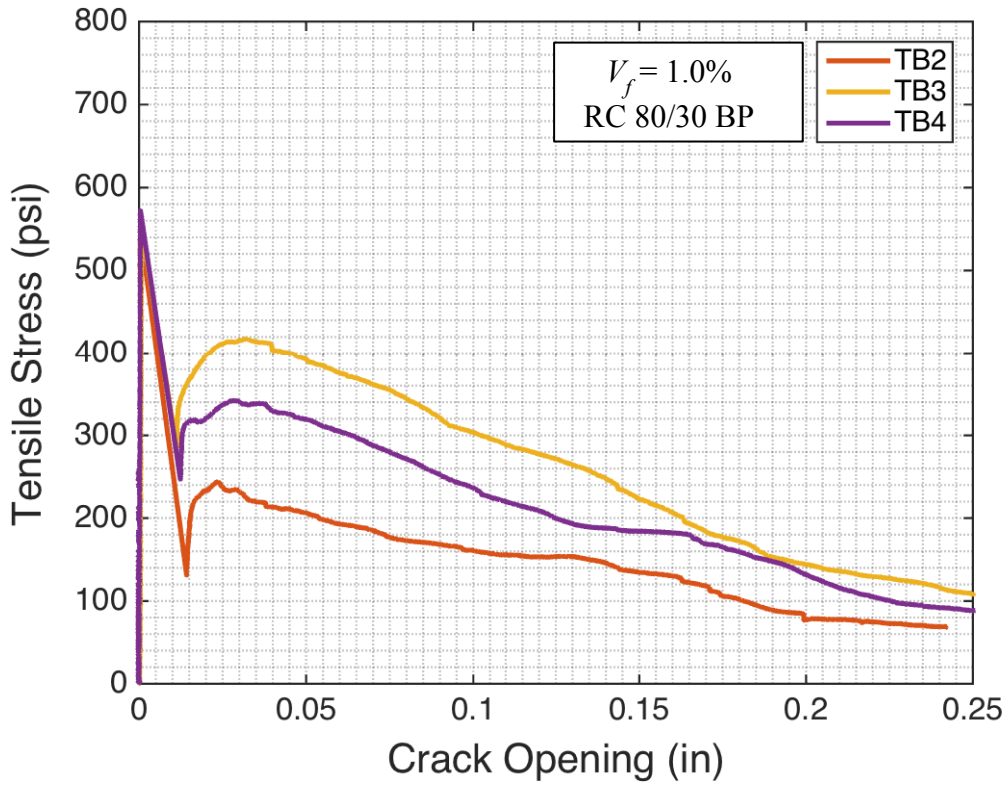


**Figure 3.41: Tensile stress versus Crack Opening Response (Tension Specimens Corresponding to CB5)**

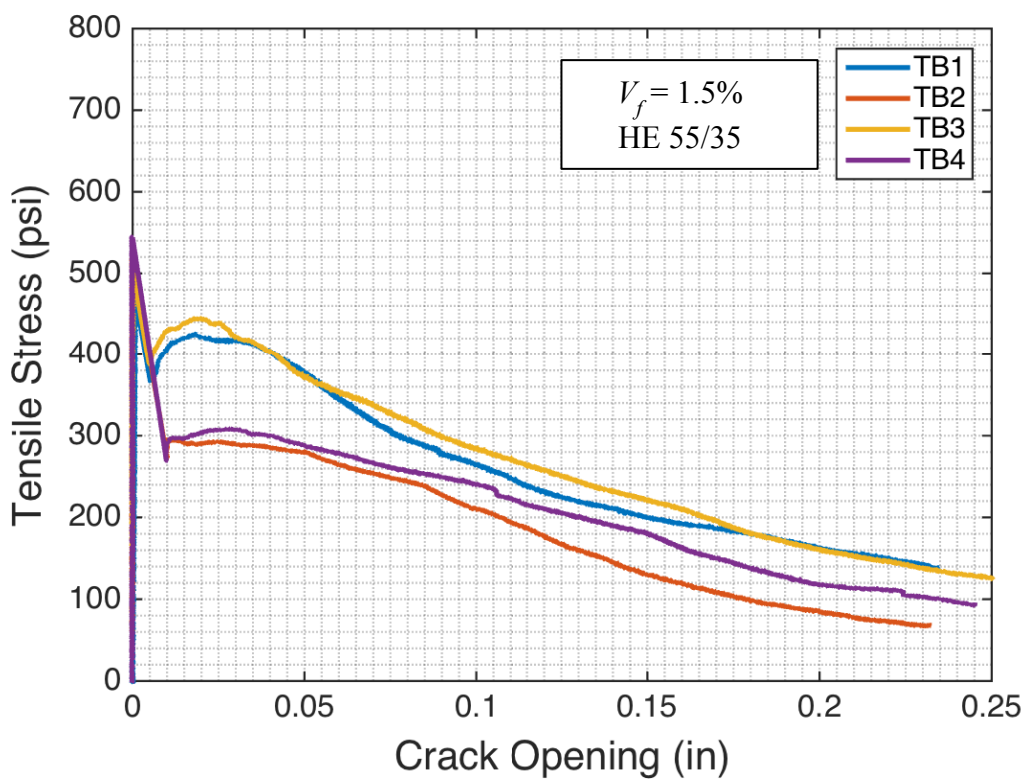


**Figure 3.42: Tensile stress versus Crack Opening Response (Tension Specimens Corresponding to CB6)**

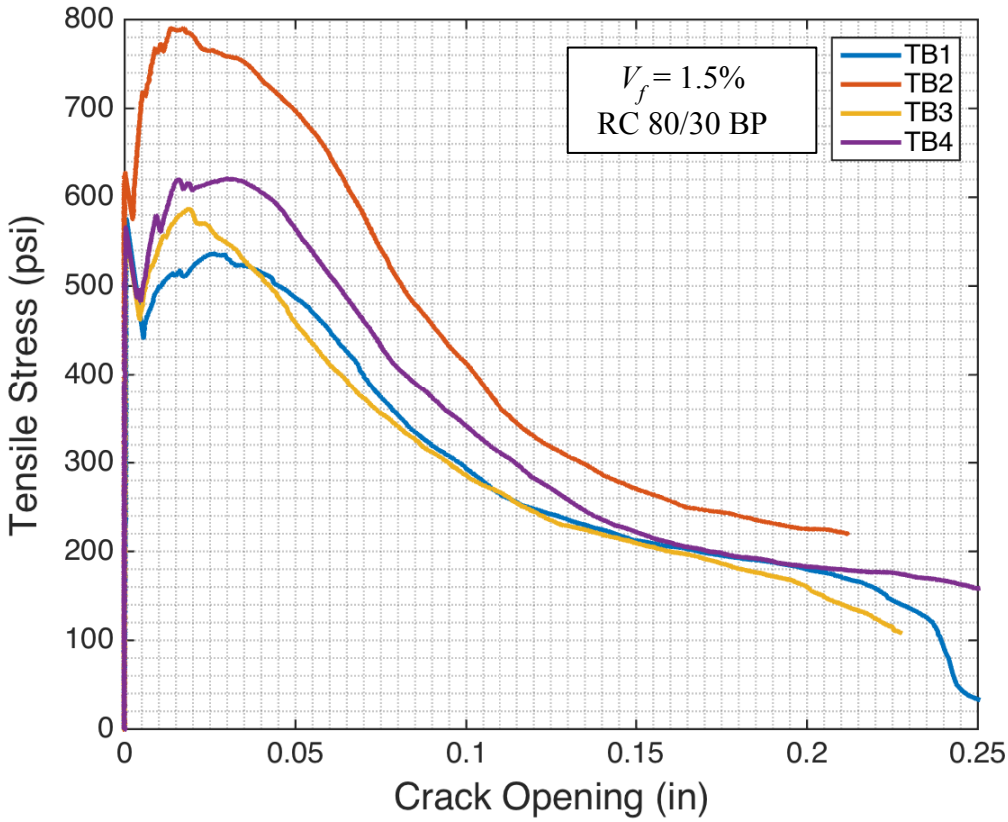


**Figure 3.43: Tensile stress versus Crack Opening Response (Tension Specimens Corresponding to CB7)**

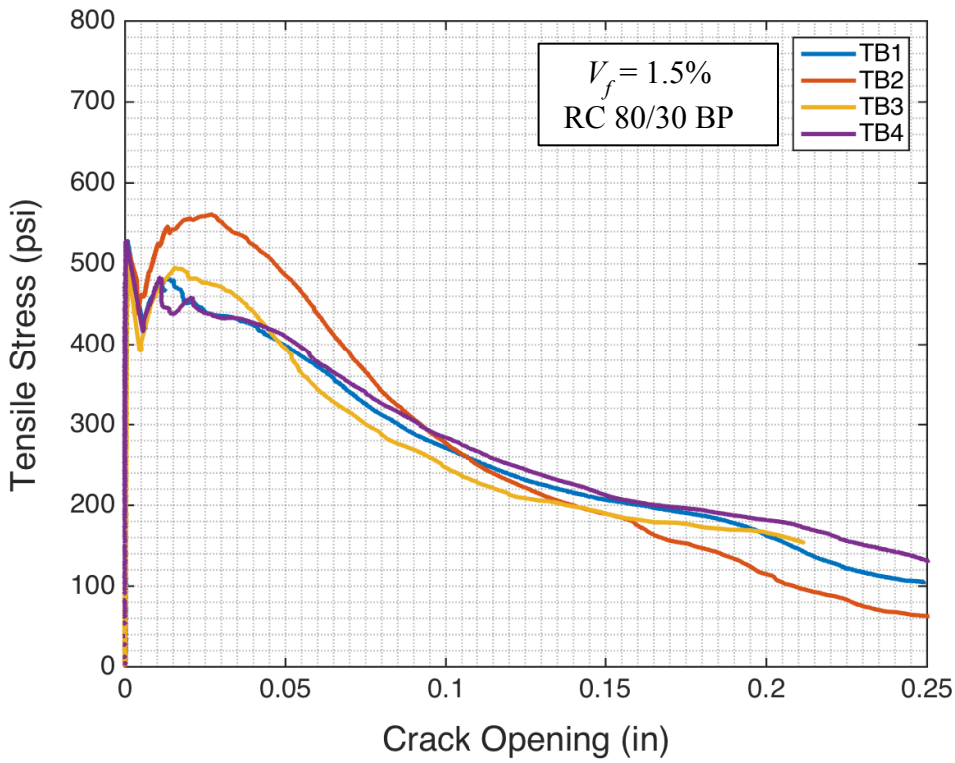


**Figure 3.44: Tensile stress versus Crack Opening Response (Tension Specimens Corresponding to CB8)**

Tensile strength recovery and tensile deformation hardening were evaluated through the ratio of peak post-cracking stress ($f_{pc}$) to cracking stress ($f_{cr}$). None of the HE 55/35 or RC 55/30 BG tension specimens exhibited tensile deformation hardening. The only specimens that exhibited tensile deformation hardening were those with RC 80/30 BP fibers at a volume fraction of 1.5%. The average results of the FRC tensile tests are summarized in Table 3.4.

In order to compare the tensile response of all the FRCs, the average responses were normalized by $\sqrt{f'_c}$ as shown in Figure 3.45 (see Table 3.5 for values of $f'_c$). The tensile first cracking strength of the FRCs ranged from 5.2 to 5.8$\sqrt{f'_c}$ (psi), with an average of 5.6$\sqrt{f'_c}$ (psi). As mentioned above, the FRC cast using RC 80/30 BP fibers at $V_f$ = 1.5% was the only FRC to exhibit tensile deformation hardening. The behavior of both of the FRCs cast with RC 55/30 BG fibers was very similar, which could be due to the fact that, on average, the specimens from these two FRCs had a very similar number of fibers inside the net tensile area.

**Table 3.4: Tensile Test Results Summary**

| Coupling Beam Specimen | $f_{cr}$ (psi) | $f_{pc}$ (psi) | $f_{pc}/f_{cr}$ | Fiber $l/d$ | Fiber | $V_f$ |
|---|---|---|---|---|---|---|
| CB1 | 458 | 203 | 0.44 | 64 | HE 55/35 | 1.25% |
| CB2 | 511 | 296 | 0.58 | 64 | HE 55/35 | 1.25% |
| CB3 | 497 | 251 | 0.51 | 55 | RC 55/30 BG | 1.25% |
| CB4 | 551 | 281 | 0.51 | 55 | RC 55/30 BG | 1.0% |
| CB5 | 556 | 312 | 0.56 | 79 | RC 80/30 BP | 1.0% |
| CB6 | 504 | 367 | 0.73 | 64 | HE 55/35 | 1.5% |
| CB7 | 589 | 644 | 1.09 | 79 | RC 80/30 BP | 1.5% |
| CB8 | 522 | 511 | 0.98 | 79 | RC 80/30 BP | 1.5% |

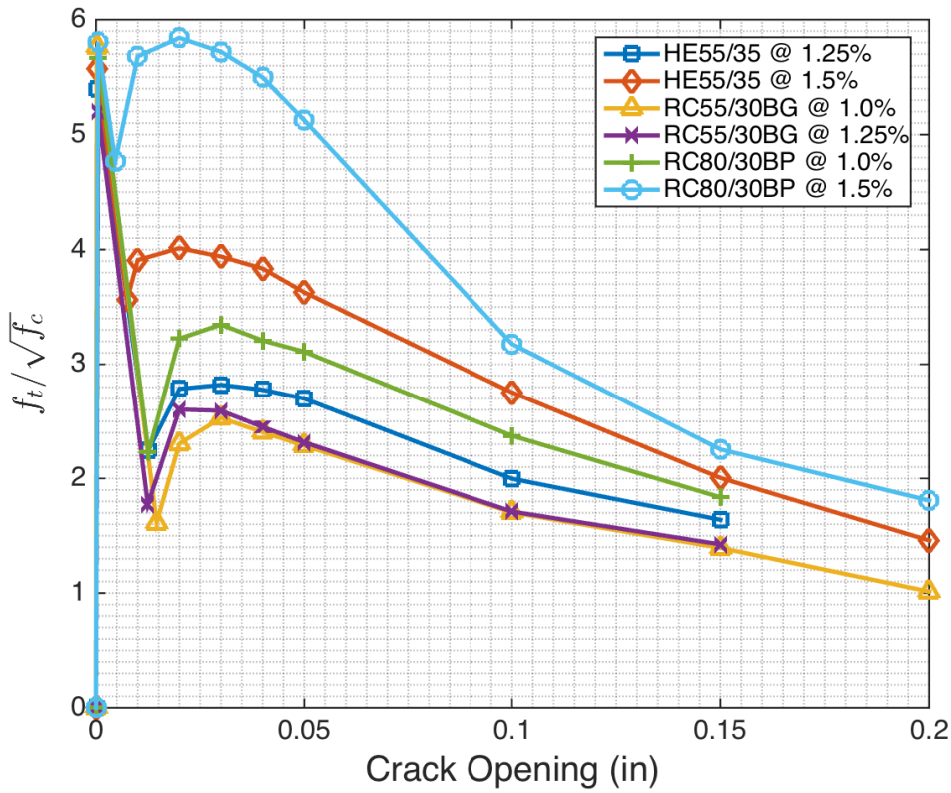


**Figure 3.45: Average Normalized Tensile Stress versus Crack Opening Response of the FRCs Investigated**

## 3.4 Relationship between Tensile and Flexural Behavior

In order to evaluate whether the tensile behavior of the FRCs obtained from the tests of notched prisms is representative of that obtained indirectly from notched and un-notched beams, the following was performed: 1) the equivalent flexural stress was calculated for each material at a maximum crack width of 0.02 in. and 0.15 in. using the simple tension model shown in Figure 3.46. Values of $f_{pc}$ and $\gamma$ used were obtained from the average response from the tension tests of notched prisms. 2) The post-cracking strength $f_{pc}$ and the residual strength parameter $\gamma$ were calculated using the results from the bending tests (notched and un-notched beams) and assuming a linear tensile behavior as shown in Figure 3.46. In both cases, the compression zone was modeled using a concrete compression stress block as defined in ACI 318-14. Given the very small depth of the compression zone, even significant errors in the estimation of the neutral axis depth would have little effect in the calculated moment strength and thus, equivalent flexural stress.

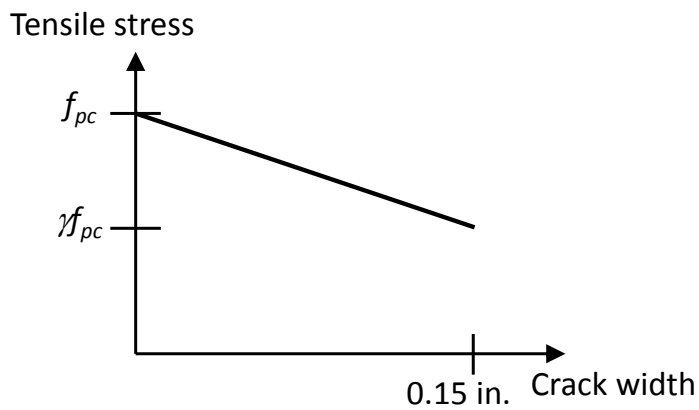


**Figure 3.46: Simulated Tensile Behavior of FRCs**

In general, reasonable estimations of the equivalent bending stress using the results from the direct tension tests, or of the tensile behavior of notched prisms using the results from the bending tests, were obtained. It should be kept in mind that the FRC in the test beams was subjected to a strain (or crack width) gradient while, theoretically, no strain (or crack width) gradient was intended in the direct tensile tests. It is thus expected that the presence (or absence) of a deformation gradient influenced the tensile behavior of the material.

For un-notched beams, the calculated equivalent flexural stress, using the simplified response in Figure 3.46 obtained from direct tensile tests, ranged approximately between 70% and 122% and between 75% and 108% of the experimental values for a maximum crack width of 0.02 in. and 0.15 in., respectively. For notched beams, the calculated stresses for these two maximum crack widths ranged between 88% and 128% and between 77% and 127% of the experimental values. In general, for a given material, the ratio between experimental and calculated equivalent bending stress was greater for the case of notched beams compared to un-notched beams. This is expected, as cracking in un-notched beams occurs at the weakest section, while the crack location in notched beams is forced to occur at a pre-determined section.

The calculated simplified tensile response obtained from the bending tests of un-notched and notched beams showed a larger variability, particularly for the case of notched beams. For the tensile response obtained from the tests of un-notched beams, calculated $f_{pc}$ and $\gamma f_{pc}$ ranged between 67% and 121% and between 75% and 113% of the values obtained from direct tensile

tests, respectively. The values of $f_{pc}$ and $\gamma f_{pc}$ calculated from the bending response of notched beams, on the other hand, ranged between 84% and 135% and between 57% and 124%, respectively.

Given the variability in bending and tensile behavior obtained from the material tests, the comparisons above suggest that results from the tests of un-notched beams, such as those based on ASTM C1609, can be used to reasonably estimate the tensile behavior of FRCs with strain-softening behavior or even of those with a slight strain-hardening behavior, such as the FRCs with RC 80/30 BP fibers at a 1.5% volume fraction.

## 3.5 Compression Cylinder Tests

In order to determine the compressive strength and the compressive behavior of the FRCs used in every coupling beam specimen, a minimum of four 6 by 12 in. cylinders were tested in compression. The use of the Optotrak system allowed the measurement of deformations up to peak strength. However, in most cases, the amount of concrete surface damage after reaching the peak strength caused the optical markers to fall off the cylinder, preventing accurate measurement of post peak deformations. Because of this, a hybrid response was used to describe the compressive behavior of the FRCs. The hybrid responses were generated using the deformations calculated based on the Optotrak data up to peak strength and the post peak response was based on the displacement data obtained from the Instron SATEC load frame. In order to obtain a continuous and compatible stress-strain curve the strains calculated from the SATEC data were adjusted to ensure that the strain at peak stress matched the strain at peak stress calculated with the Optotrak data (Figure 3.47).

The stress-strain curves obtained from each cylinder were averaged to generate average response curves for each of the FRCs used for each coupling beam specimen. The main parameters used to describe the responses, i.e., compressive strength ($f'_c$), strain at peak strength ($\varepsilon o$) and strain at a 50% strength loss ($\varepsilon 50u$) are presented in Table 3.5. The elastic modulus ($E_c$) was defined as the secant modulus of elasticity at a stress equal to $0.5f'_c$. Also reported is the slope of the descending branch of the response ($Z_{50}$), which is defined as the slope of a linear segment

connecting the point of peak strength to the point at which the strength decreased by 50%, normalized by the concrete compressive strength. $Z_{50}$ can be calculated per Equation 17. It should be mentioned that the values of $f'_c$ reported in Table 3.5 correspond to the average of all cylinders tested, while only some of them were instrumented for determination of compressive stress versus strain response. Also, cylinders corresponding to Coupling Beams CB6 and CB7 were tested in two groups a significant period apart (see Table A1 in Appendix A). The increase in measured compressive strength over time for these two specimens, however, was only 11% and 16%, respectively. Thus, the average of all cylinders was considered representative of the cylinder compressive strength.

$$Z_{50} = \frac{0.5}{\varepsilon_{50u} - \varepsilon_o} \tag{17}$$

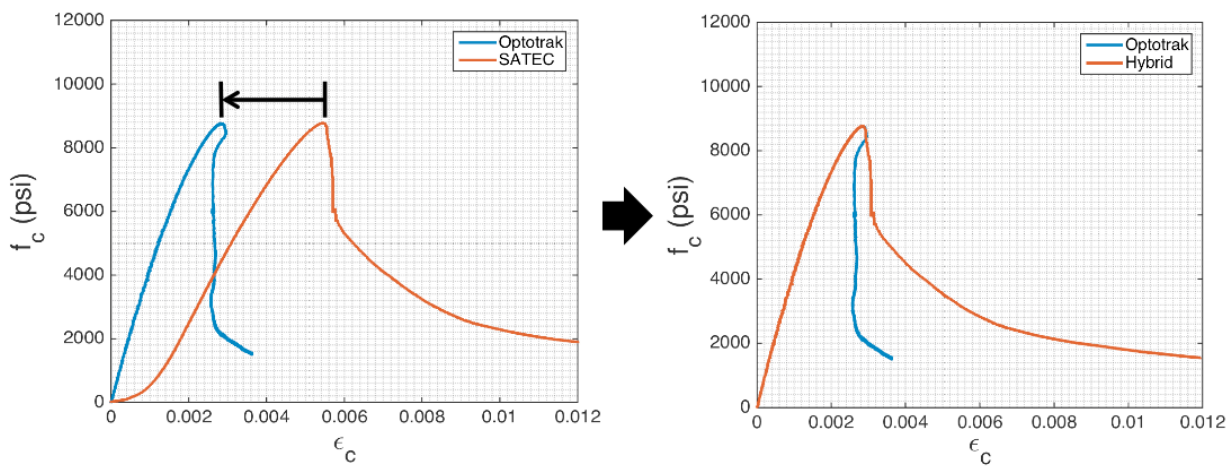


**Figure 3.47: Stress-Strain Curves used to Estimate Post-Peak Response of FRC Cylinders**

**Table 3.5: Average Compressive Response Parameters**

| CB Specimen | Fiber | $V_f$ | $f'_c$ (psi) | $\varepsilon_0$ | $\varepsilon_{50u}$ | $E_c$ (ksi) | $Z_{50}$ |
|---|---|---|---|---|---|---|---|
| CB1 | HE 55/35 | 1.25% | 7790 | 0.0024 | 0.0042 | 4700 | 278 |
| CB2 | HE 55/35 | 1.25% | 8690 | 0.0024 | 0.0034 | 5090 | 500 |
| CB3 | RC 55/30 BG | 1.25% | 8490 | 0.0027 | 0.0038 | 4370 | 455 |
| CB4 | RC 55/30 BG | 1.00% | 9180 | 0.0029 | 0.0039 | 4440 | 500 |
| CB5 | RC 80/30 BP | 1.00% | 9790 | 0.0029 | 0.0041 | 4240 | 417 |
| CB6 | HE 55/35 | 1.50% | 8320 | 0.0026 | 0.0050 | 5250 | 208 |
| CB7 | RC 80/30 BP | 1.50% | 10,210 | 0.0029 | 0.0071 | 4820 | 119 |
| CB8 | RC 80/30 BP | 1.50% | 8510 | 0.0024 | 0.0056 | 4460 | 156 |

The FRCs with a fiber volume fraction of 1.5% had the most ductile compressive response of the FRCs investigated. In general, as expected, the strain at peak strength increased with an increase in $f'_c$. The average compressive responses of each of the FRCs under consideration are presented in Figure 3.48. For comparison purposes the curves shown in Figure 3.48 were normalized by their respective compressive strengths.

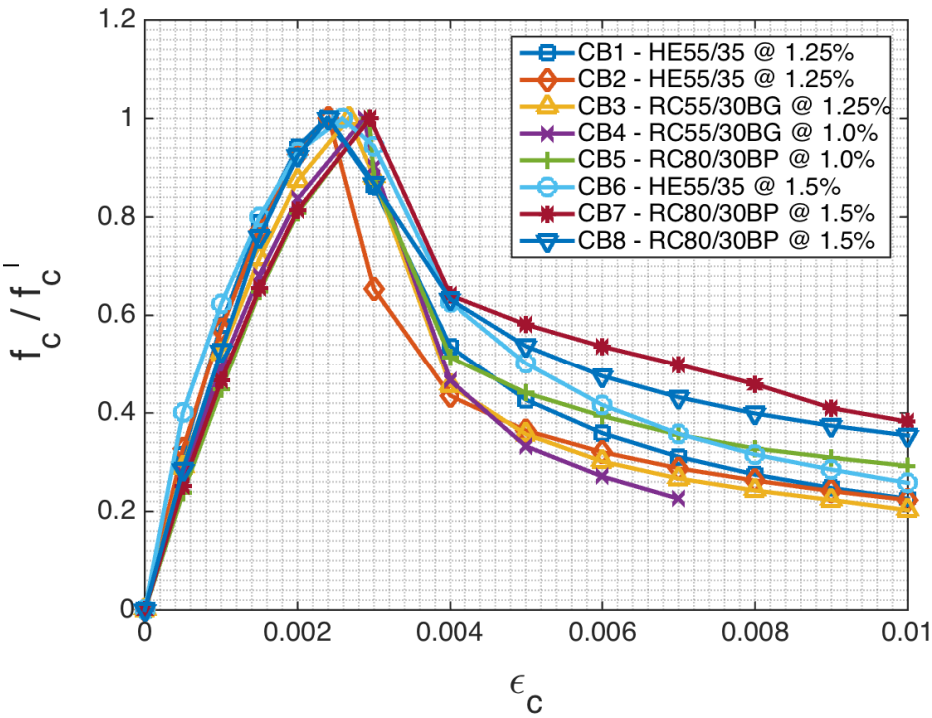


**Figure 3.48: Normalized FRC Compressive Stress-Strain Responses**

## 3.6 Steel Reinforcement Tensile Tests

All the steel reinforcement used in the coupling beam specimens was tested in accordance to ASTM A370-14. The reinforcing bars were tested at the minimum stress rate allowed of 10,000 psi/min. and the Optotrak system was used to monitor strains. Figure 3.49 shows the location of the markers used to monitor the deformations of the steel reinforcing bars.

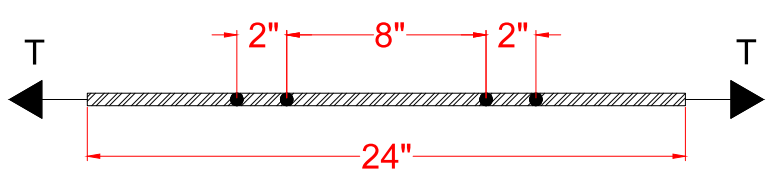


**Figure 3.49: Optotrak Marker Layout for Tensile Testing of Reinforcement Bars**

Some of the reinforcement tested did not exhibit a clear yield plateau, as can be seen in Figure 3.50. The reported yield strengths ($f_y$) were calculated either as the average strength in the yield plateau or using the 0.2% offset method whenever a yield plateau was not clearly defined. Key parameters that describe the tensile behavior of the reinforcement steel, i.e., yield strength, tensile strength ($f_u$), elastic modulus ($E_s$), ultimate strain capacity ($\varepsilon_u$), and strain at initiation of strain hardening ($\varepsilon_{sh}$) are summarized in Table 3.6.. Figure 3.50 through Figure 3.53 show sample experimental stress-strain curves for the reinforcing bars used in the coupling beam specimens.

**Table 3.6: Steel Reinforcement Properties**

| Specimen | Bar Size | $f_y$ (ksi) | $f_u$ (ksi) | $E_s$ (ksi) | $\varepsilon_u$ | $\varepsilon_{sh}$ |
|---|---|---|---|---|---|---|
| CB1 | #3 | 67 | 98.0 | 29200 | 0.13 | ** |
| | #4 | 67 | 102 | 29200 | 0.10 | ** |
| | #6 | 79 | 100 | 28900 | 0.14 | 0.020 |
| CB2 | #3 | 69 | 99.0 | 29100 | 0.12 | ** |
| | #4 | 84 | 99.0 | 29000 | 0.11 | 0.022 |
| | #6 | 79 | 99.0 | 29000 | 0.14 | 0.020 |
| CB3 | #3 | 69 | 99.0 | 29100 | 0.12 | ** |
| | #4 | 82 | 99.0 | 29100 | 0.13 | 0.022 |
| | #6 | 79 | 99.0 | 29000 | 0.14 | 0.020 |
| CB4 | #3 | 72 | 103 | 29200 | 0.13 | ** |
| | #4 | 80 | 95.0 | 29200 | 0.10 | 0.023 |
| | #5 | 83 | 101 | 28900 | 0.10 | 0.019 |
| CB5 | #3 | 68 | 100 | 29000 | 0.10 | 0.016 |
| | #4 | 84 | 101 | 28900 | 0.11 | 0.021 |
| | #5 | 82 | 100 | 29100 | 0.12 | 0.020 |
| CB6 | #3 | 74 | 103 | 28900 | 0.12* | ** |
| | #4 | 68 | 95.0 | 29100 | 0.13 | ** |
| CB7 | #3 | 69 | 99.0 | 29200 | 0.12* | ** |
| | #4 | 87 | 104 | 28900 | 0.10 | 0.022 |
| CB8 | #3 | 69 | 98.0 | 29100 | 0.16 | ** |
| | #4 | 70 | 104 | 29000 | 0.12* | ** |

* Optotrak markers came off during testing and thus, the ultimate strain was estimated using the displacement from the MTS load frame and the original length of the test bar between the grips of the load frame.
** No clear yield plateau was observed.

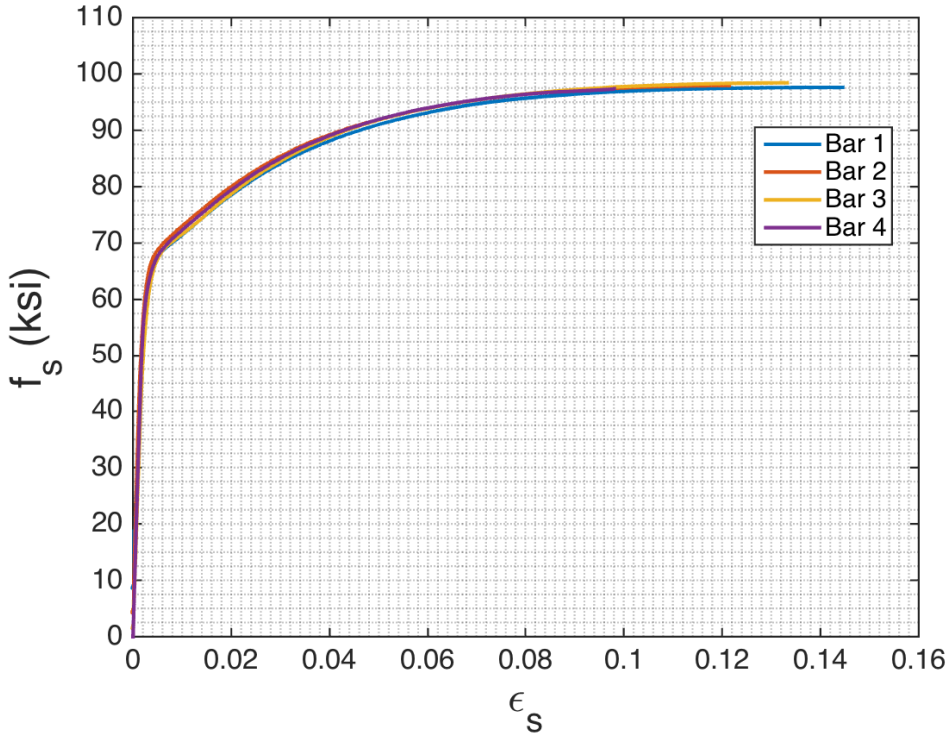


**Figure 3.50: Sample Tensile Responses of #3 Reinforcing Bars**

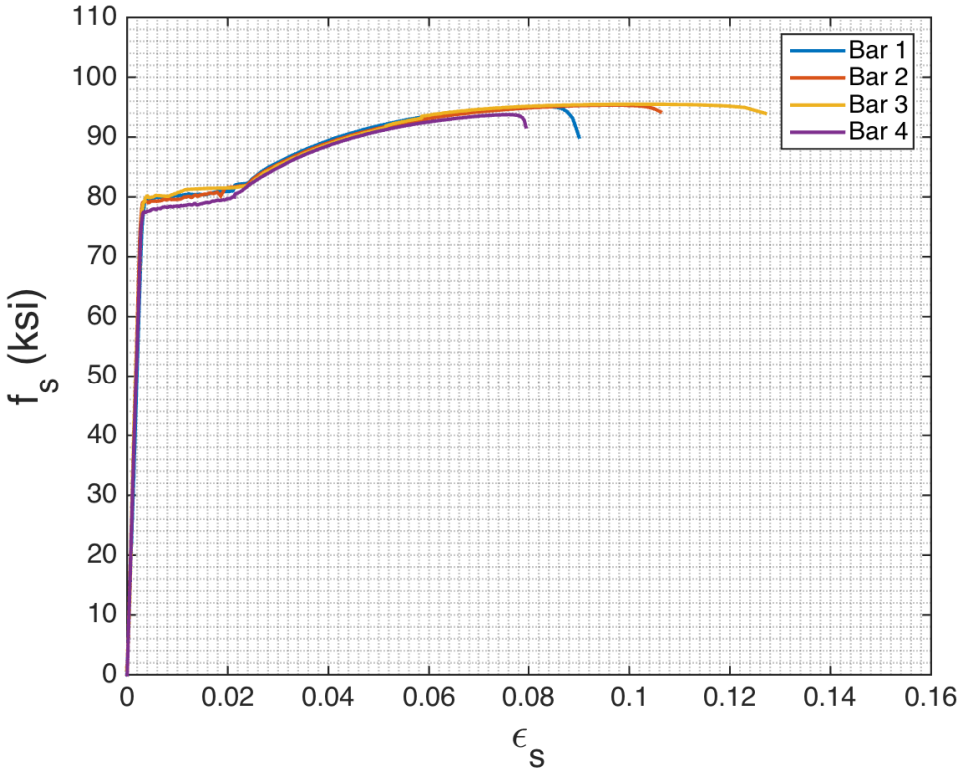


**Figure 3.51: Sample Tensile Responses of #4 Reinforcing Bars**

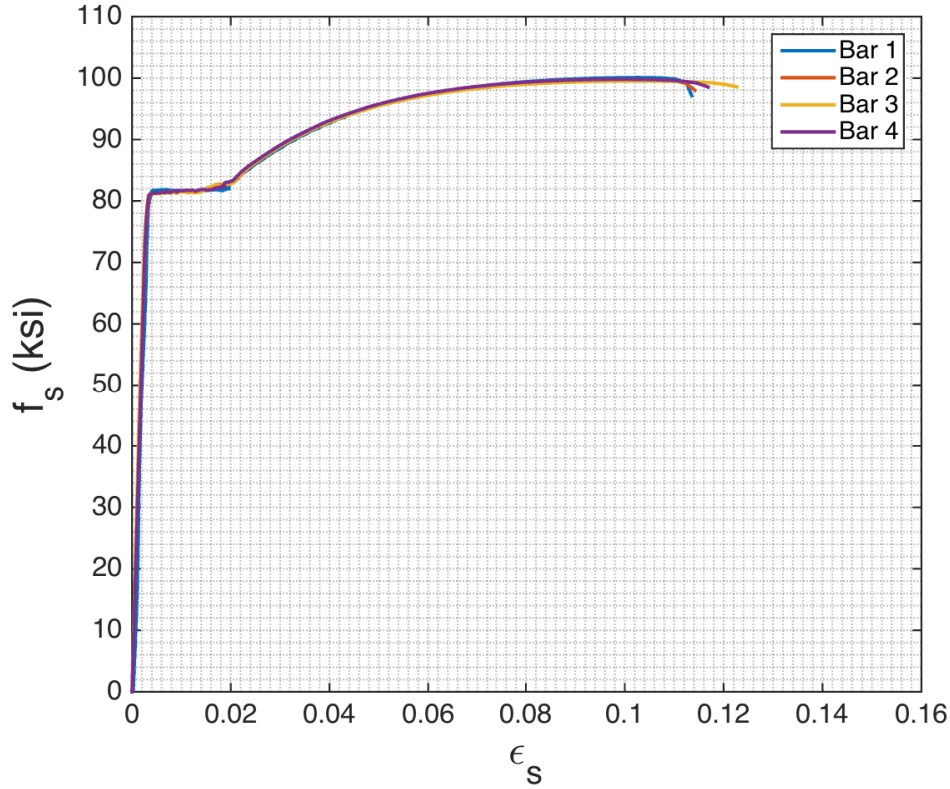


**Figure 3.52: Sample Tensile Responses of #5 Reinforcing Bars**

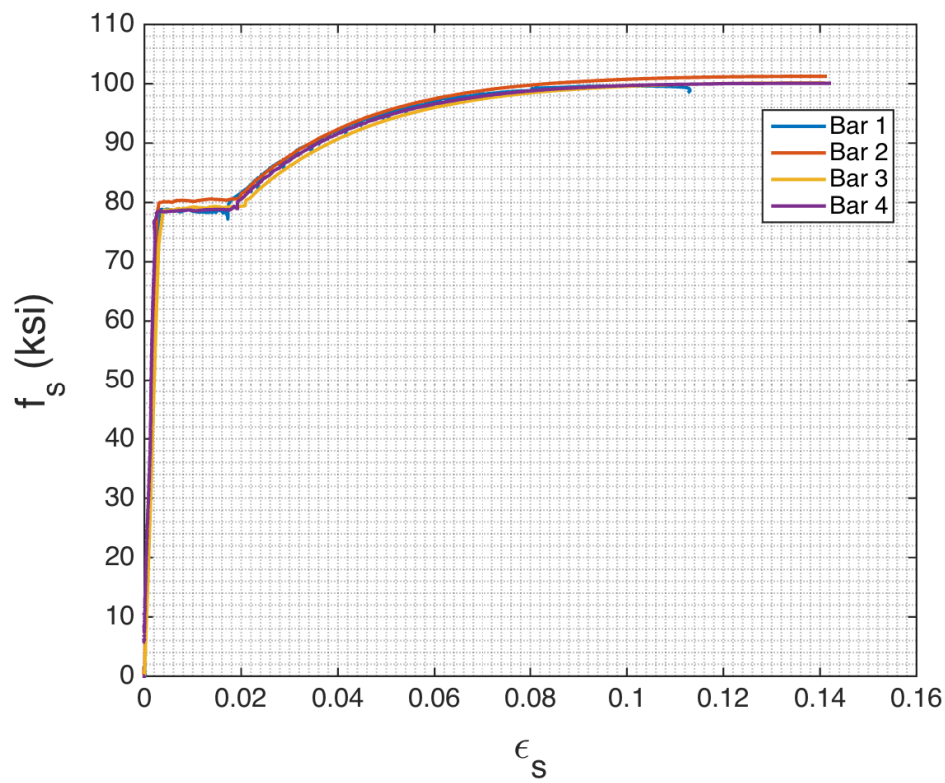


**Figure 3.53: Sample Tensile Responses of #6 Reinforcing Bars**

# 4 Coupling Beam Test Results

## 4.1 Overall Behavior

All test coupling beam specimens, except Coupling Beam CB1, exhibited a stable behavior under large displacement reversals with peak average shear stresses ranging between approximately 7 and 10 $\sqrt{f'_c}$ (psi). Coupling beam drift capacity in these specimens was at least 5.0%. In Coupling Beam CB1, on the other hand, the amount of longitudinal reinforcement was greater than that in all other specimens, which translated into a higher peak shear stress (12.2 $\sqrt{f'_c}$ [psi]) and lower drift capacity. Drift capacity was defined as the average of the peak positive and negative drift of the last cycle completed prior to a strength loss greater than 20% of the peak strength in either loading direction.

In general, early cracking in the coupling beams consisted of flexural cracks at the beam ends and diagonal cracks in the middle region of the beam. Except for Coupling Beam CB1, diagonal cracks in the middle region of the beam remained narrow, while flexural cracks at the beam ends widened as lateral displacements increased and reinforcement yielding developed at the beam ends. At large drifts, typically 4.0% and greater, significant damage could be observed at the beam ends, characterized by some concrete crushing and spalling, and the joining of flexural cracks corresponding to both loading directions, which typically led to a through-depth crack at each beam end. Ultimately, significant shear sliding developed along these through-cracks, which led to a substantial loss of lateral stiffness and energy dissipation capacity of the specimens.

Table 4.1 presents a summary of the peak responses of the coupling beam specimens including peak average shear stress demand (based on the gross cross section), $v_u$, peak axial load, $P_u$, and average of the peak positive and negative drift of the last cycle completed prior to a strength loss greater than 20% and 30%. Also included in Table 4.1 is the concrete compressive strength, $f'_c$, calculated as the strength average of the cylinders cast from the first two batches of each FRC material, which were those used to cast the coupling beam specimens (see Section 2.2.2). At least two cylinders were tested on the coupling beam test day, except for Specimen CB1 for which only one cylinder was tested on the coupling beam test day. The other cylinders used to

calculate average compressive strength were tested within ten days of the coupling beam test. Axial forces developed in the coupling beams were calculated based on the axial force in each vertical steel arm obtained through a load cell, where a positive force corresponds to a compressive axial force in the coupling beam.

The behavior as well as the damage observed during each coupling beam test are discussed next.

**Table 4.1: Summary of Coupling Beam Peak Responses**

| Specimen | $f'_c$ (psi) | $V_u$ (kips) | $v_u$ (psi) | $v_u/\sqrt{f'_c}$ | $P_u$ (kips) | Drift | |
|---|---|---|---|---|---|---|---|
| | | | | | | 20% loss | 30% loss |
| CB1 | 7930 | 117 | 1080 | 12.2 | 89 | 3.4% | 3.4% |
| CB2 | 8840 | 100 | 930 | 9.9 | 144 | 5.5% | 6.5% |
| CB3 | 8630 | 95 | 880 | 9.5 | 116 | 6.7% | 6.7% |
| CB4 | 9260 | 75 | 690 | 7.2 | 99 | 5.2% | 6.2% |
| CB5 | 9750 | 83 | 770 | 7.8/6.6** | 91 | 6.2%* | 6.7%* |
| CB6 | 7950 | 78 | 720 | 8.1/7.3** | 74 | 5.1%* | 6.1%* |
| CB7 | 9330 | 105 | 970 | 10.1 | 125 | 5.3% | 5.3% |
| CB8 | 8490 | 82 | 760 | 8.2 | 90 | 6.2% | 7.7% |

* Reported drifts based on peak strength reached after adjustment of axial force
** Peak shear stress after adjustment of axial force

### 4.1.1 Coupling Beam Specimen CB1

Coupling Beam CB1, with HE 55/35 fibers at a volume fraction of 1.25%, was subjected to a peak shear stress of $\mathbf{12.2}\sqrt{\boldsymbol{f'_c}}$ (psi). The calculated shear contribution of the transverse reinforcement in the middle region of the beam, assuming a longitudinal projection of the diagonal crack equal to the beam effective depth *d* and using the measured yield strength of the steel (67 ksi, see Section 3.6), was $\mathbf{6.2}\sqrt{\boldsymbol{f'_c}}$ (psi) (see also Section 4.5.1). For simplicity, a constant *d* value of 15.5 in. was assumed for all specimens .This shear stress proved too large, which led to a rapid degradation of shear resisting mechanisms after a few displacement cycles and, ultimately, a premature shear failure in the mid-region of the beam as shown in Figure 4.1.

**Figure 4.1: Shear Failure of Specimen CB1**

The shear stress versus drift hysteresis for Specimen CB1 is shown in Figure 4.2. The applied shear stress, *v*, calculated based on the gross cross sectional area, is shown normalized by $\sqrt{f'_c}$ (psi). Drifts were adjusted to account for relative rotations between the top and bottom blocks using Equation 2.

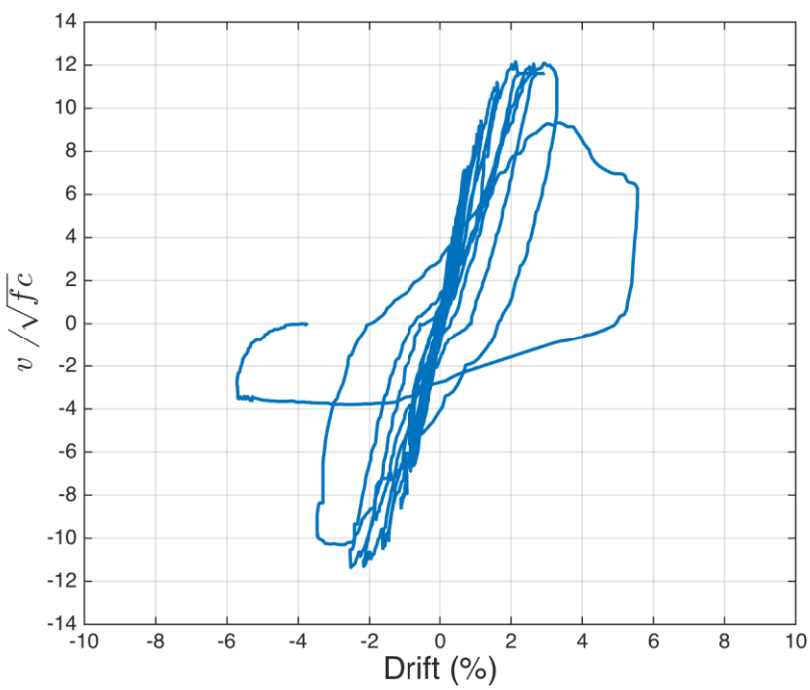


**Figure 4.2: Hysteresis Response of Specimen CB1**

In Specimen CB1 diagonal cracking initiated throughout the mid-span region, along with some flexural cracks near the beam ends. As the applied lateral displacement increased, extensive diagonal cracking developed throughout the beam length. These cracks, however, remained

narrow (≤ 0.02 in.) with negligible damage at the beam ends and beam-to-wall interface during displacement cycles of up to 3.0% drift.

Figure 4.3 shows the cracking pattern observed at 1.0%, 2.0% and 3.0% drift levels. When pushed to 4.0% drift, the coupling beam suffered a sudden strength loss caused by significant shear-related damage that developed in the middle region of the beam. This failure was characterized by severe beam cracking and dilation, as well as the development of a large splitting crack along the main longitudinal reinforcement near the top end of the beam (right end on Figure 4.1).

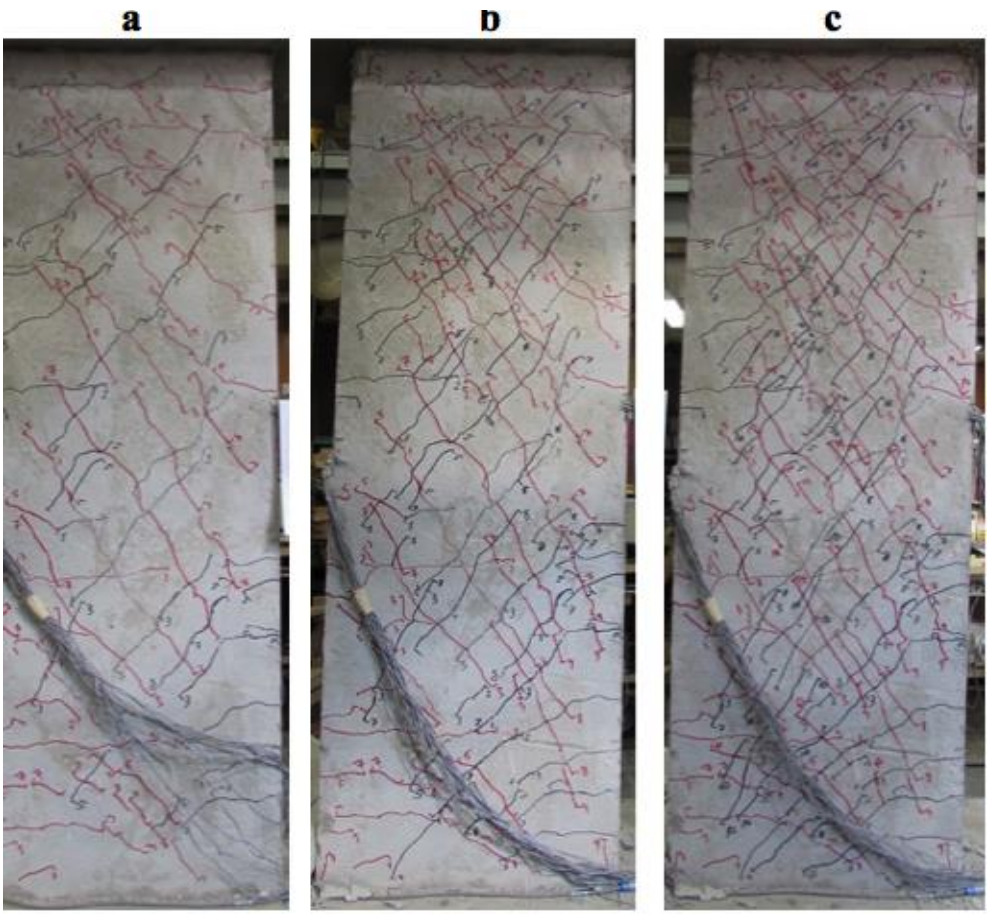


**Figure 4.3: Damage Progression in Specimen CB1, a) 1.0% Drift, b) 2.0% Drift, c) 3.0% Drift.**

Maximum axial force developed in the beam, caused by longitudinal expansion due to concrete cracking and reinforcement yielding through cycling, was 89 kips. This axial force corresponded

to an average axial stress of $0.10f'_c$ based on the beam gross area and to 76% of the peak applied shear. The maximum elongation of the coupling beam prior to failure was 0.10 in., which corresponded to an average longitudinal tensile strain of approximately 0.2%.

### 4.1.2 Coupling Beam Specimen CB2

Coupling Beam CB2 was also reinforced with HE 55/35 fibers at a volume fraction of 1.25%. The beam exhibited wide hysteresis loops throughout loading cycles up to approximately 5.0% drift (Figure 4.4), indicating a stable, flexurally-dominated response. This specimen was subjected to a peak shear stress close to the maximum limit allowed in ACI 318-14 of $10\sqrt{f'_c}$ (psi) for diagonally reinforced coupling beams.

Specimen CB2 developed the highest axial load (144 kips) among the coupling beams investigated, which corresponded to an average compressive stress of $0.15f'_c$ based on the gross cross sectional area and 1.44 times the peak applied shear force. Average peak elongation of the beam was approximately 0.28 in., which corresponds to an average axial strain of approximately 0.5%. The peak shear stress of $9.8\sqrt{f'_c}$ was first achieved at a drift of approximately 2.8% in the positive loading direction. Peak shear force in subsequent drift cycles up to 5.0% drift (inclusive) was greater than 90% of the overall peak shear force.

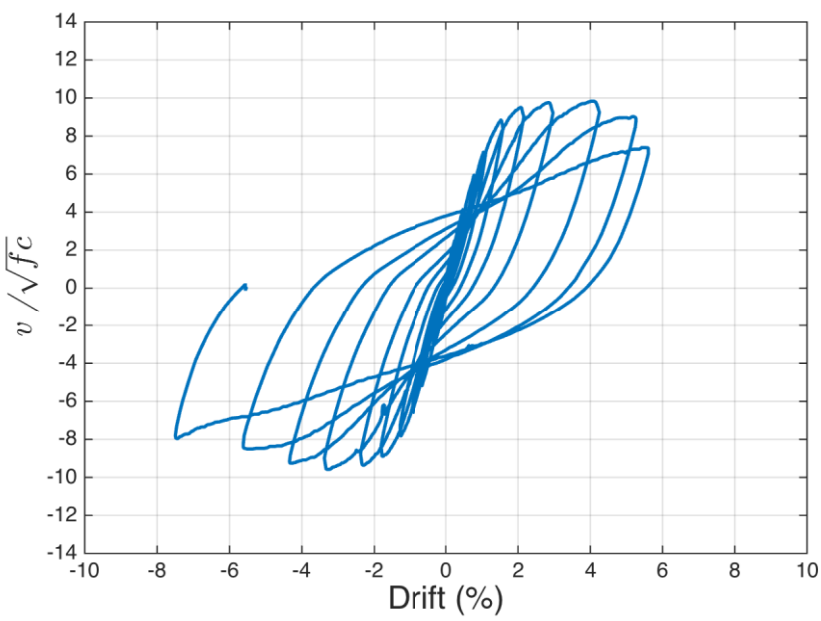


**Figure 4.4: Hysteresis Response of Specimen CB2**

Flexural cracks in Specimen CB2 were observed at the ends of the beam and near the termination of the dowels during small displacements cycles (< 1.0% drift). Although diagonal cracks were also observed in the mid-region of the beam, flexural cracks were dominant. Cracking continued to spread throughout the beam up to approximately 2.0% drift, after which only a few new cracks formed. As the imposed displacement was further increased, damage concentrated at the beam ends, mostly near the section where the U-shaped dowels ended. For drifts greater than approximately 4.0%, significant damage was observed at the ends of the beam. Shear sliding displacements were evident during the cycles at 4.0% and 5.0% drifts, once flexural cracks corresponding to the two loading directions joined to form a through-depth crack. The damage observed in Specimen CB2 at 2.0%, 4.0% and 5.5% drift is shown in Figure 4.5.

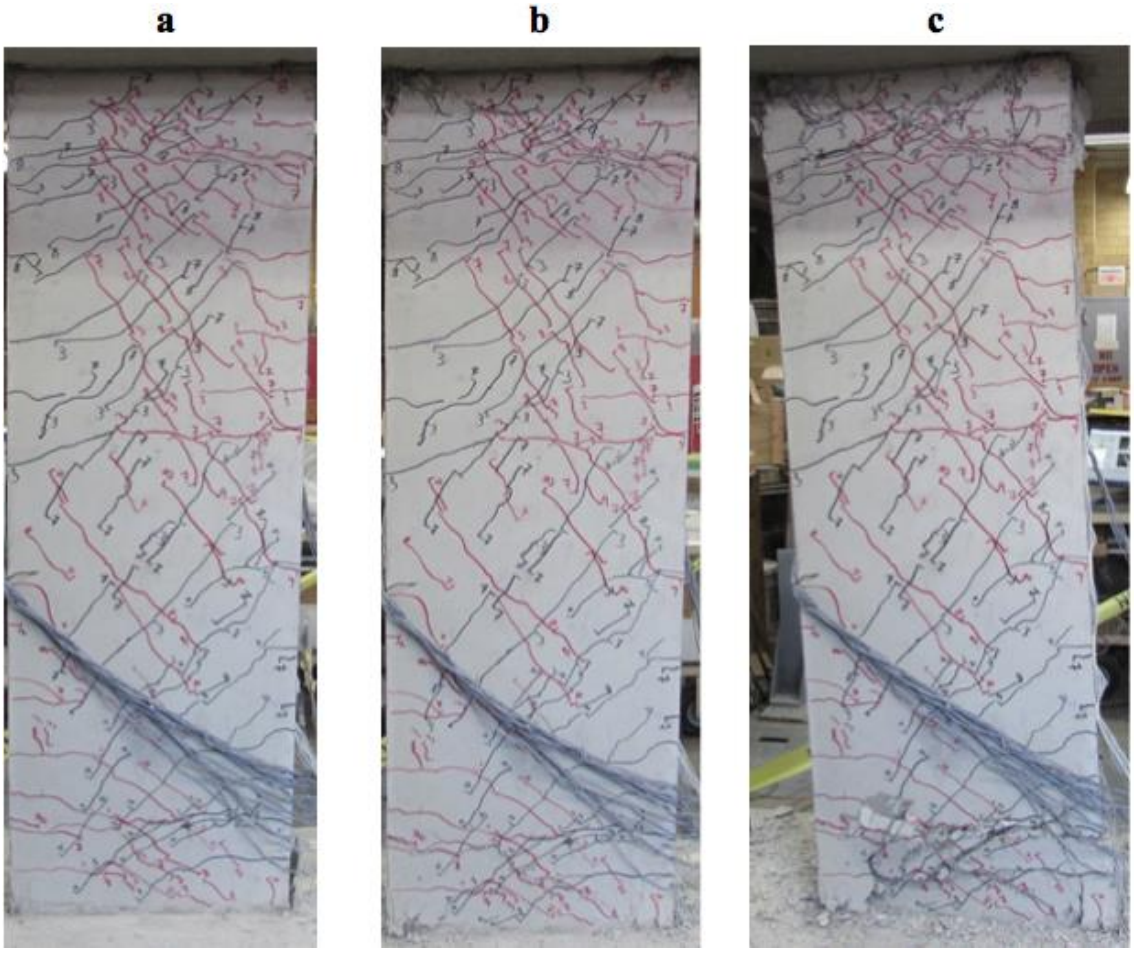


**Figure 4.5: Damage Progression in Specimen CB2, a) 2.0% Drift, b) 4.0% Drift, c) End of Test (Drift ≈ -5.5%)**

### 4.1.3 Coupling Beam Specimen CB3

The behavior of Specimen CB3 was very similar to that of Specimen CB2. However, Specimen CB3 was reinforced with RC 55/30 BG fibers at a volume fraction of 1.25%. The beam sustained drifts of 5.2% and 8.2% in the positive and negative loading directions, respectively, while maintaining at least 80% of its peak shear strength in each loading direction. The peak shear demand was achieved at approximately 4.0% drift. Overall, Specimen CB3 exhibited stable hysteresis, characterized by relatively wide loops, as shown in Figure 4.6. The maximum axial compressive force developed in the beam (116 kips) corresponded to a stress of approximately $0.12f'_c$ based on the gross cross-sectional area and was 22% higher than the peak applied shear force.

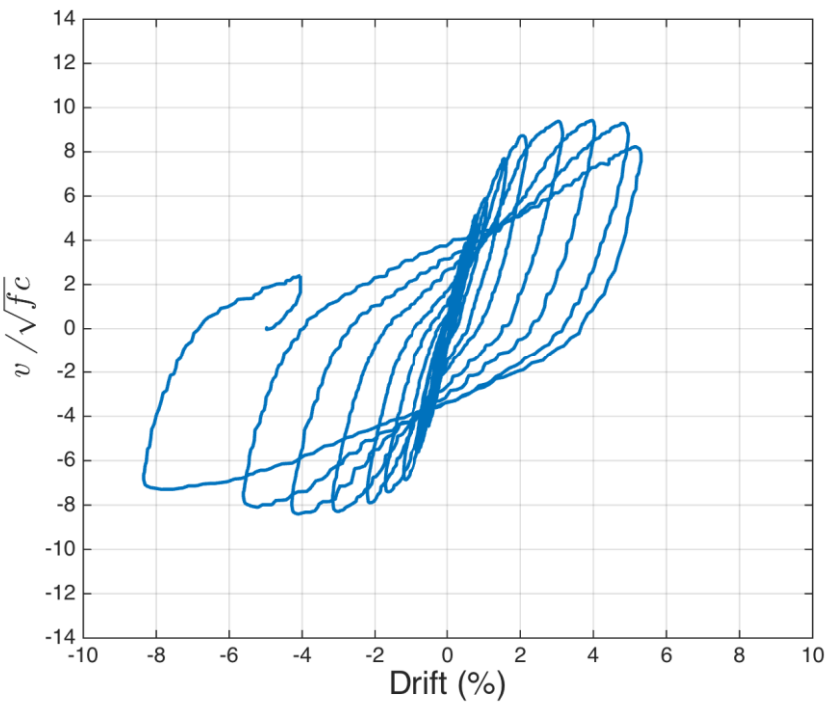


**Figure 4.6: Hysteresis Response of Specimen CB3**

The small displacement cycles (< 1.0% drift) applied to Specimen CB3 were characterized by the formation of flexural cracks near the ends of the beam as well as some diagonal cracks around mid-span. Multiple cracks continued to form throughout the beam up to approximately 2.0% drift. As the applied displacement increased the cracks near the ends grew wider and by 4.0% drift, considerable damage had accumulated near the beam ends. Figure 4.7 shows the condition of Coupling Beam CB3 at 2.0%, 4.0% and 5.6% drift. As can be seen in Figure 4.7c

wide through-depth flexural cracks had developed towards the end of the test, which allowed substantial sliding displacements to occur and ultimately leading to failure of the specimen.

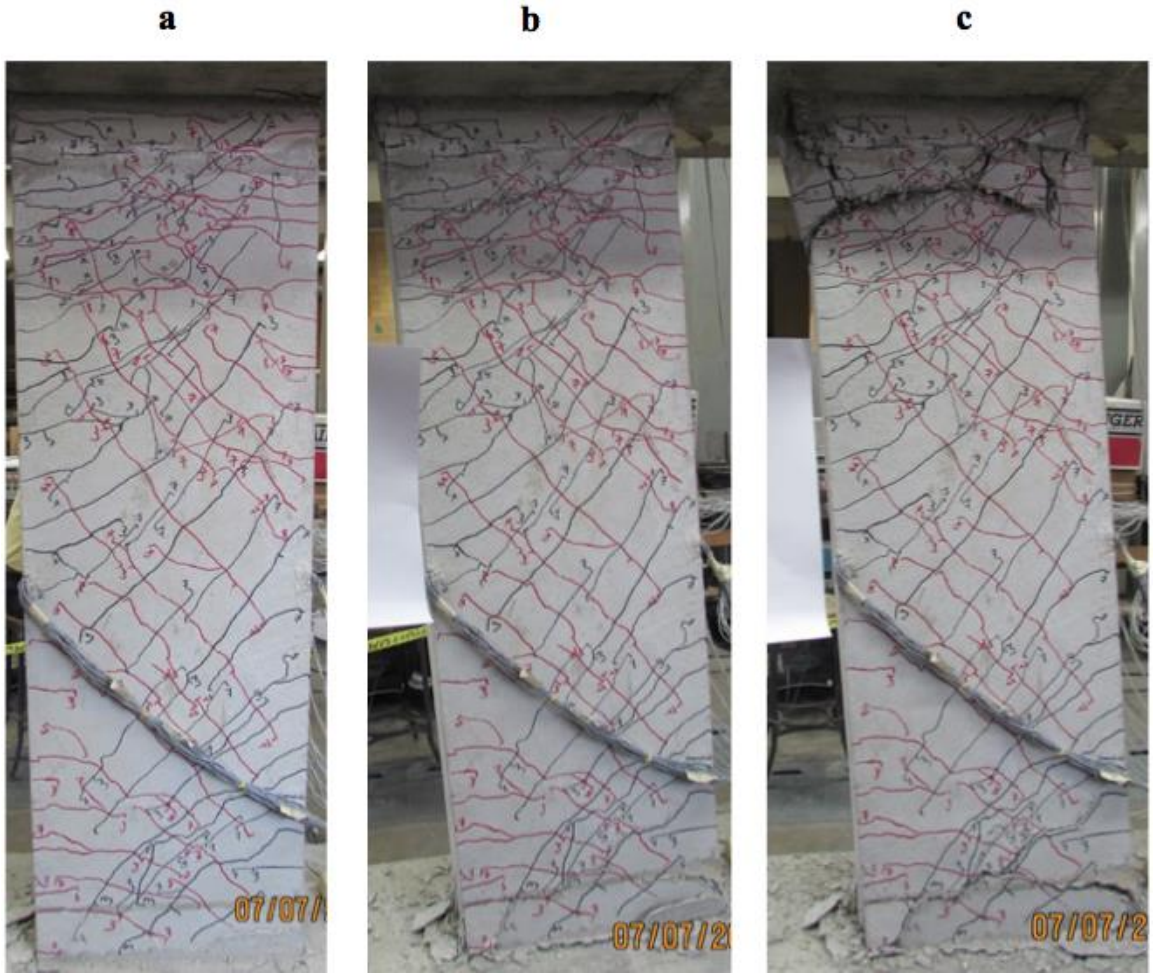


**Figure 4.7: Damage Progression in Specimen CB3, a) -2.0% Drift, b) -4.0% Drift, c) -5.6% Drift**

### 4.1.4 Coupling Beam Specimen CB4

Specimen CB4 was the first beam cast using an FRC with a volume fraction of 1.0% (RC 55/30 BG fibers were used). This specimen was thus designed for a lower peak shear stress compared to Specimens CB1 through CB3. The hysteresis response for Specimen CB4 is shown in Figure 4.8. The peak shear stress demand was $7.2\sqrt{f'_c}$ (psi), which was achieved at approximately 3.2% drift (positive direction). Although the peak shear applied in subsequent

cycles decreased, the specimen was able to maintain at least 80% of the peak strength up to 5.1% and 6.5% drift in the positive and negative loading directions, respectively. A peak axial force of 99 kips (1.32$V_u$) was developed in the beam, which corresponded to an axial compressive stress of approximately 0.10$f'_c$ based on the beam gross section area. The beam elongated a maximum of approximately 0.27 in. due to concrete cracking and accumulation of strain in the longitudinal reinforcement during displacement reversal cycles. This elongation corresponds to a peak axial strain of approximately 0.5%.

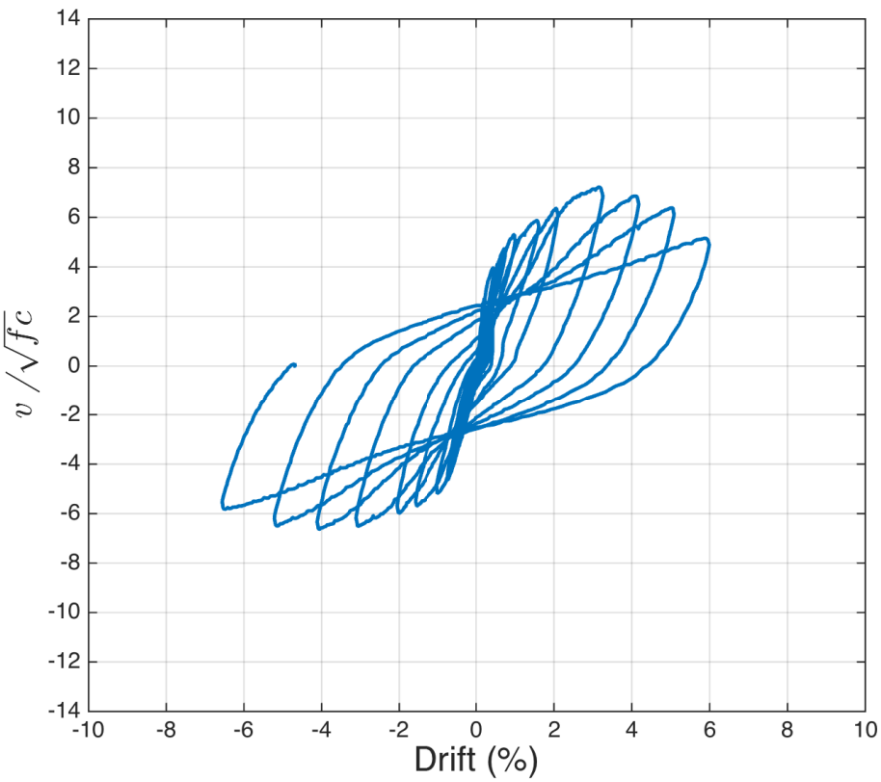


**Figure 4.8: Hysteresis Response of Specimen CB4**

Flexural cracks started to form at the beam ends since the early displacement cycles and cracking continued to spread throughout the beam, similarly to what was observed in previous specimens. However, cracking was not as dense as the cracking pattern exhibited by the other coupling beams with steel fibers at a 1.25% fiber volume fraction. The smaller volume fraction used for Specimen CB4 allowed the cracks to grow wider instead of proliferating. A large flexural crack (0.1 in. wide) started to open near the top end of the beam when a drift of 1.5% was achieved. This crack continued to widen as the applied displacement further increased, achieving a width

of approximately 5/16 in. as the beam was displaced to 3.0% drift. The cracking pattern observed, as well as the damage at various stages of the test, is shown in Figure 4.9. Wide intersecting flexural cracks can be seen at the top plastic hinge (Figure 4.10a), where deformations localized since early in the test. During the last drift cycles, extensive damage accumulated at both beam ends, as shown in Figure 4.10b, mostly localized along a single through-depth crack at each beam end.

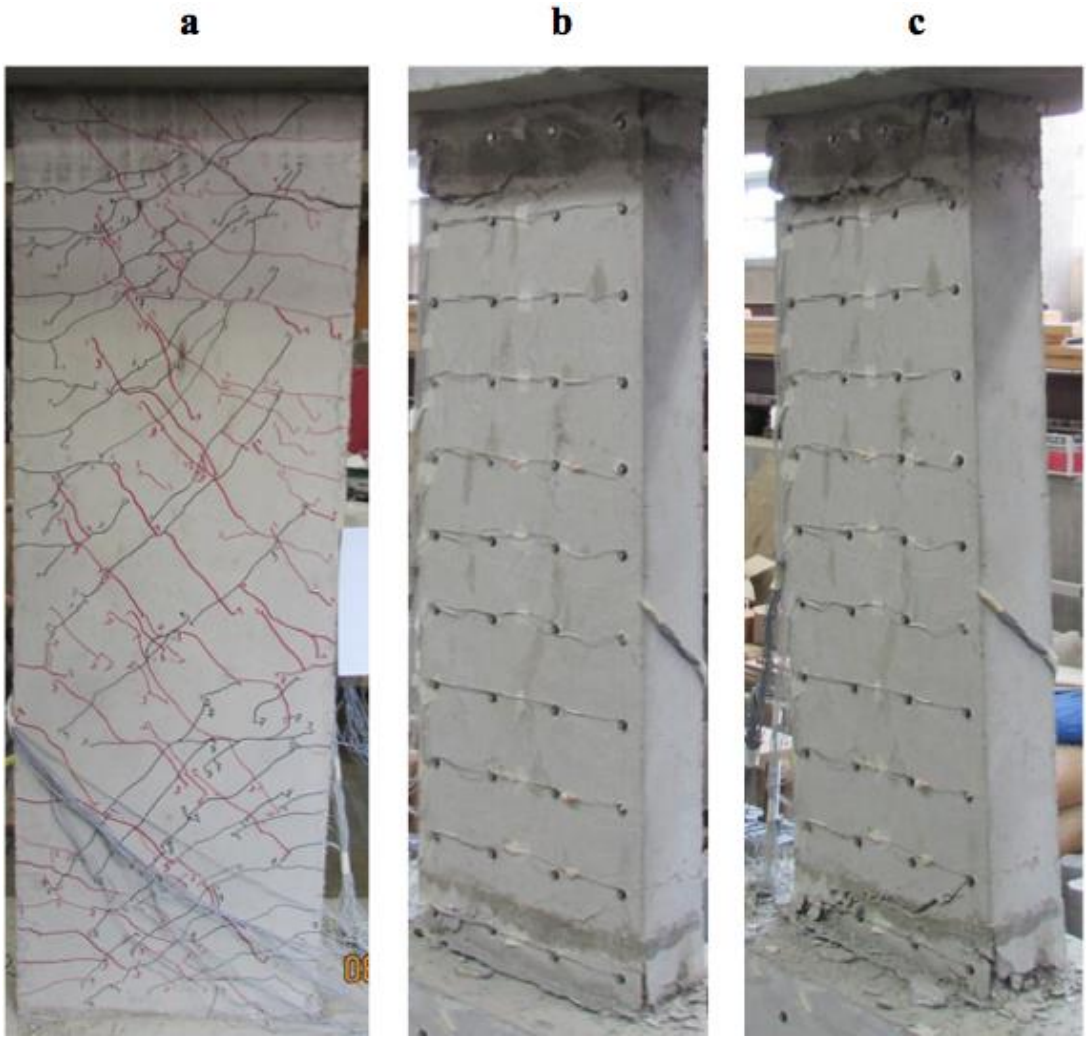


**Figure 4.9: Damage Progression in Specimen CB4, a) 2.0% Drift, b) 4.1% Drift, c) 6.0% Drift**

After the test was completed, the loosed and damaged concrete in the plastic hinge regions was removed to observe the extent of damage that the plastic hinges had sustained. Figure 4.10c shows the significant amount of concrete that could be removed, which extended to the confined

concrete core. It should be kept in mind, however, that this specimen sustained large shear stress demands through cycles up to approximately 6.0% drift. This suggests that the steel fibers considered in this study, at a volume fraction of 1.0%, can be successfully implemented in the design of FRC coupling beams with $\boldsymbol{l_n/h = 3}$, subjected to shear stress demands up to $\boldsymbol{6\sqrt{f'_c}}$ (psi).

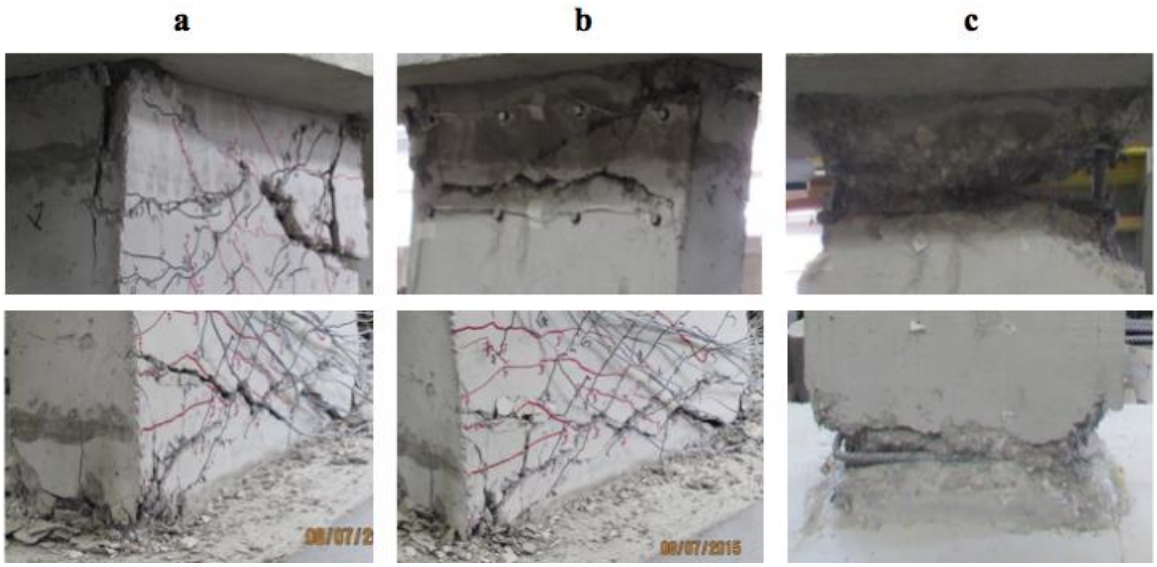


**Figure 4.10: Ends of Coupling Beam CB4, a) 6.0% Drift, b) -6.5% Drift, c) After Removal of Spalled Concrete**

### 4.1.5 Coupling Beam Specimen CB5

Specimen CB5 was the second specimen cast using an FRC with a 1.0% fiber volume fraction. Contrary to Specimen CB4, however, high strength (330 ksi) fibers (RC80/30 BP) were used. The behavior of Specimen CB5 was characterized by a stable hysteresis response with large displacement capacity. The hysteresis response of Specimen CB5 is shown in Figure 4.11.

A peak shear strength of $7.8\sqrt{f'_c}$ was achieved at a drift of approximately 3.1% in the positive displacement direction. At this point the axial force developed in the beam was 91 kips, which corresponded to a compressive stress of approximately $0.09f'_c$ based on the beam gross cross-sectional area. Given the potential for substantial increases in axial load with continuing cycling, which would result in an increased flexural strength and shear stresses higher than the target of $8\sqrt{f'_c}$ (psi), the bolts connecting the steel links that provided the axial restraint to the coupling

beams were loosened. The peak axial load developed by the beam after loosening the bolts was 88 kips ($1.06V_u$) and the maximum estimated elongation was 0.38 in., corresponding to an average axial strain of approximately 0.7%.

After the axial load was adjusted the highest shear stress achieved was $6.6\sqrt{f'_c}$ (psi), which was reached at a drift of approximately 5.1%. This decrease in shear stress was caused by the decrease in axial force developed in the coupling beam and not by damage developed in the specimen. Specimen CB5 exhibited a drift capacity of approximately 6.2%, taken as the maximum drift achieved before a 20% strength loss compared to the second peak ($6.6\sqrt{f'_c}$ [psi]).

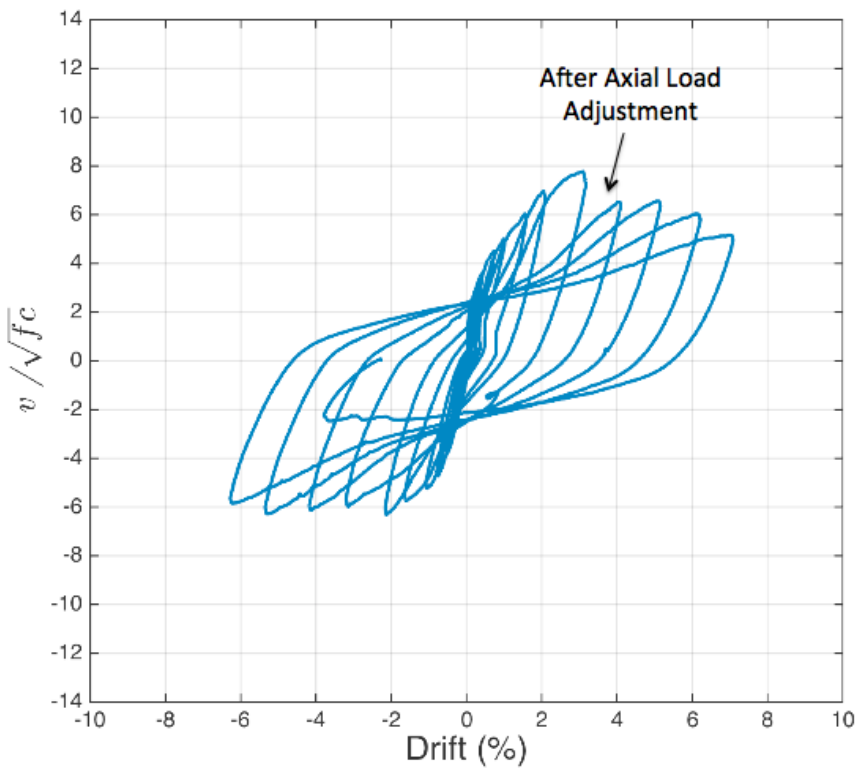


**Figure 4.11: Hysteresis Response of Specimen CB5**

During the smaller displacement cycles, flexural cracks formed near the beam ends while diagonal cracks formed around the mid-span region. New cracks continued to form throughout the beam up to drifts of approximately 2.0% (Figure 4.12a). In general the cracking pattern was very similar to that of Specimen CB4. However, the crack widths remained much smaller (≤ 0.08 in.) in Specimen CB5 up to drifts of approximately 3.0% in the positive direction. RC 80/30 BP

fibers thus exhibited better crack width control than the RC 55/30 BG fibers. Figure 4.12b shows the damage observed at 4.0% drift. As the applied lateral displacements further increased damage continued to concentrate at both beam ends and a through-depth crack formed at the top of the beam (Figure 4.12a). Beam damage at 6.2% drift is shown in Figure 4.12c. After a drift of approximately 7.0% the coupling beam failed due to the fracture of several of the main longitudinal reinforcement bars. Once the test ended, the damaged concrete around the plastic hinges was removed to expose the fractured bars, which are shown marked in red in Figure 4.13b and Figure 4.13c.

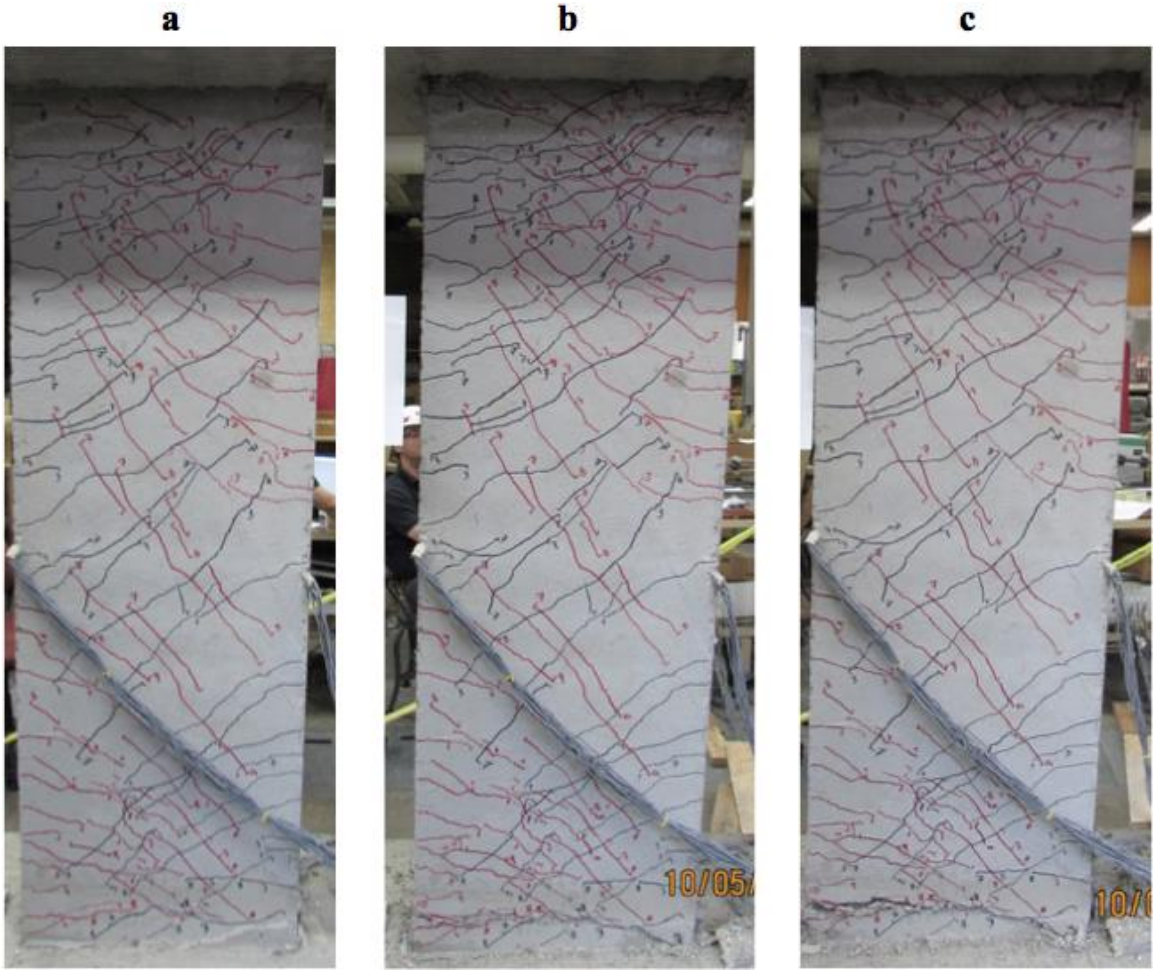


**Figure 4.12: Damage Progression in Specimen CB5, a) 2.0% Drift, b) 4.0% Drift, c) 6.2% Drift**

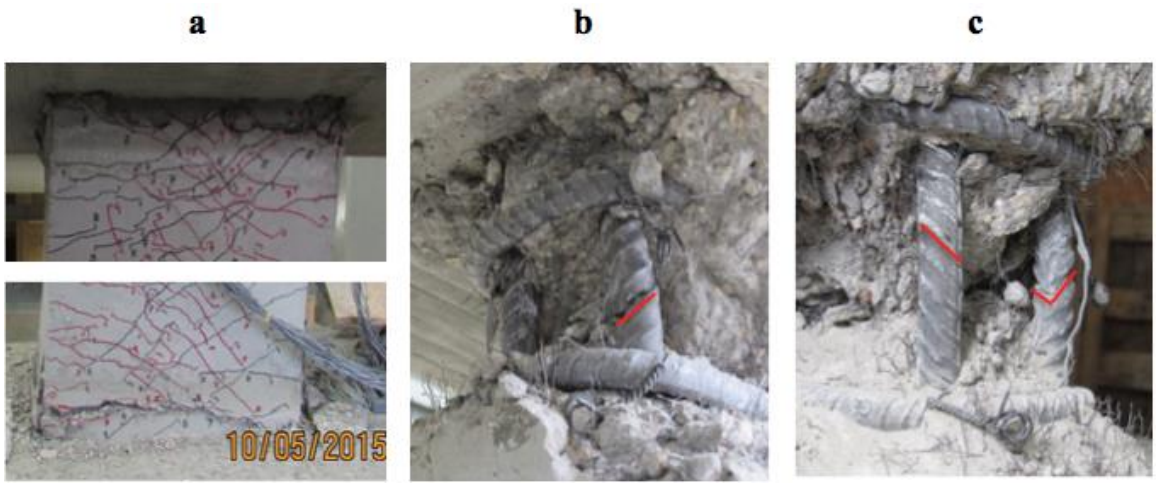


**Figure 4.13: Damage after testing of Specimen CB5, a) Through-Depth Cracks at Top and Bottom Plastic Hinges, b) Fractured Flexural Reinforcement (Top Plastic Hinge), c) Fractured Flexural Reinforcement (Bottom Plastic Hinge)**

### 4.1.6 Coupling Beam Specimen CB6

Specimen CB6 was the first coupling beam tested with a span-to-depth ratio of 2.0. Given the increased role played by shear as the beam aspect ratio was decreased, Specimen CB6 was reinforced with a 1.5% volume fraction of HE 55/35 fibers.

In spite of the small span-to-depth ratio, the behavior of Specimen CB6 was predominantly flexurally-dominated. The hysteresis response of Specimen CB6 is shown in Figure 4.14. The bolts connecting the links providing axial restraint were loosened after the beam developed shear stresses in excess of $8\sqrt{f'_c}$ (psi), at a drift of approximately 3.6% in the negative direction. The peak axial load developed up to this point was 74 kips, which corresponded to an average compressive stress of approximately $0.09f'_c$ based on the gross area of the cross section. After this adjustment, the maximum shear stress sustained by the beam was $7.3\sqrt{f'_c}$ (psi) at a drift of approximately 4.0%. The maximum axial force devolved after the links were loosened was 70 kips ($0.9V_u$) and the maximum elongation of the beam throughout the test was 0.33 in., which corresponded to an average axial strain of 0.9%. The lateral displacement capacity of Specimen CB6 was approximately 5.1% drift in both directions while maintaining at least 80% of the second peak shear strength ($7.3\sqrt{f'_c}$ [psi]).

During the first few displacement cycles several flexural cracks formed near the ends of the beam and some diagonal shear cracks near the mid-span region. Cracking did not seem to be as dense as in the specimens with $l_n/h = 3$. As the lateral displacement was increased beyond 2.0% drift, cracking concentrated at the very ends of the beam and significantly more damage occurred at the beam-to-wall interfaces compared to the more slender specimens. By the time a drift of approximately 4.0% was achieved, a large flexural crack had formed near the top end of the beam and the flexural cracks near the bottom support were starting to join to form a through-depth crack. As the applied displacements further increased the deformations continued to localize at the ends, making the cracks wider and enabling sliding displacements to take place. The cracking pattern as well as the damaged sustained at different drift levels are shown in Figure 4.15.

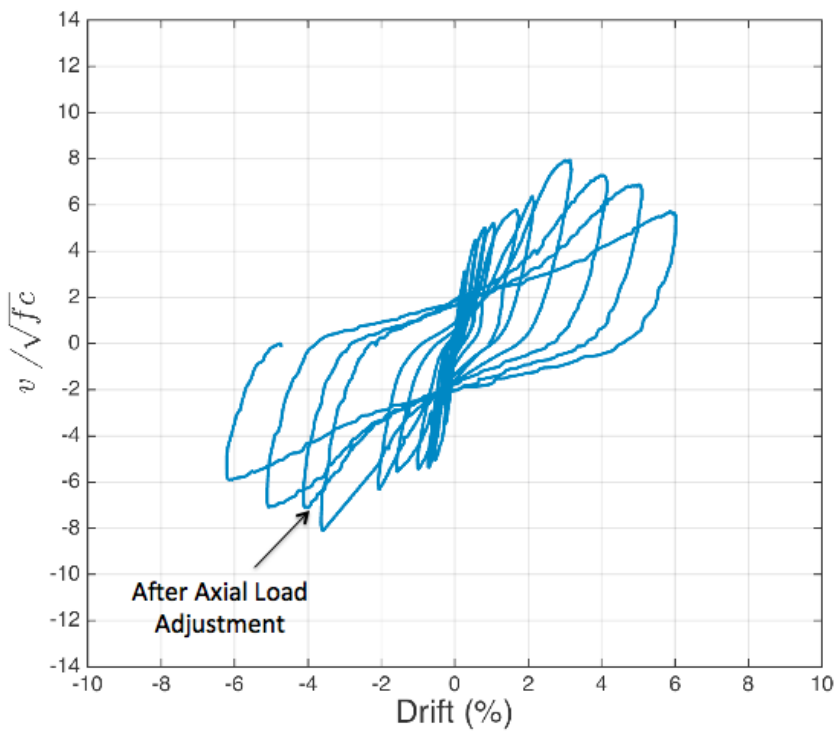


**Figure 4.14: Hysteresis Response of Specimen CB6**

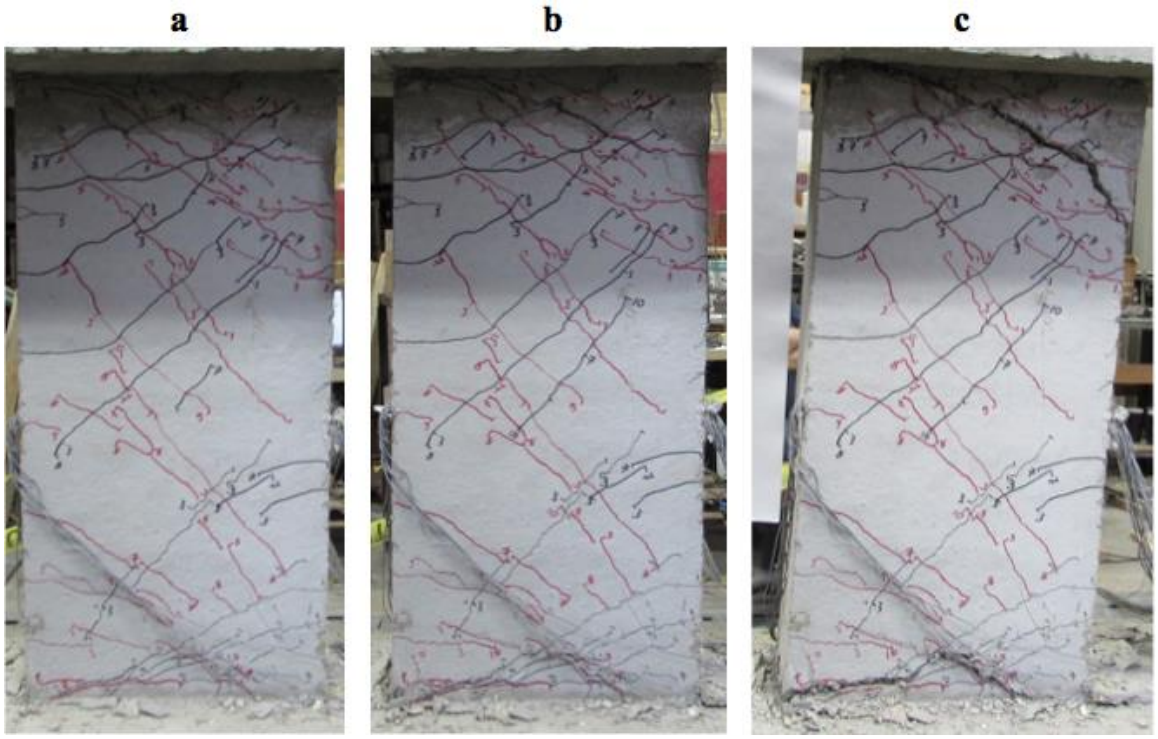


**Figure 4.15: Damage Progression in Specimen CB6, a) 2.1% Drift, b) 4.1% Drift, c) 6.0% Drift**

### 4.1.7 Coupling Beam Specimen CB7

An FRC with a 1.5% fiber volume fraction was also used in Specimen CB7. However, RC 80/30 BP fibers were used instead of HE55/35 fibers. The hysteresis response of Specimen CB7 is shown in Figure 4.16. This specimen developed the second highest axial load among the tested coupling beam (125 kips; see Table 4.1). The presence of this large axial force substantially increased the flexural capacity, which resulted in shear stress demands much higher than intended. This axial force of 125 kips corresponded to an average compressive stress of approximately $0.12f'_c$ based on the gross area of the cross section and was approximately 20% higher than the maximum applied shear force, $V_u$. At a lateral displacement of approximately 4.0% drift, the beam sustained a shear stress of $10.1\sqrt{f'_c}$ (psi). The high shear stresses acting on the beam, combined with the displacement reversals, caused substantial degradation of the shear resisting mechanisms associated with the FRC. This led to a rapid loss of strength as the displacements were further increased beyond 4.0% drift. The rapid loss of strength for drifts exceeding 4.0% can be observed in the hysteresis response shown in Figure 4.16. Even under

these high demands Specimen CB7 achieved a displacement of approximately 5.3% drift while retaining at least 80% of its strength in each loading direction.

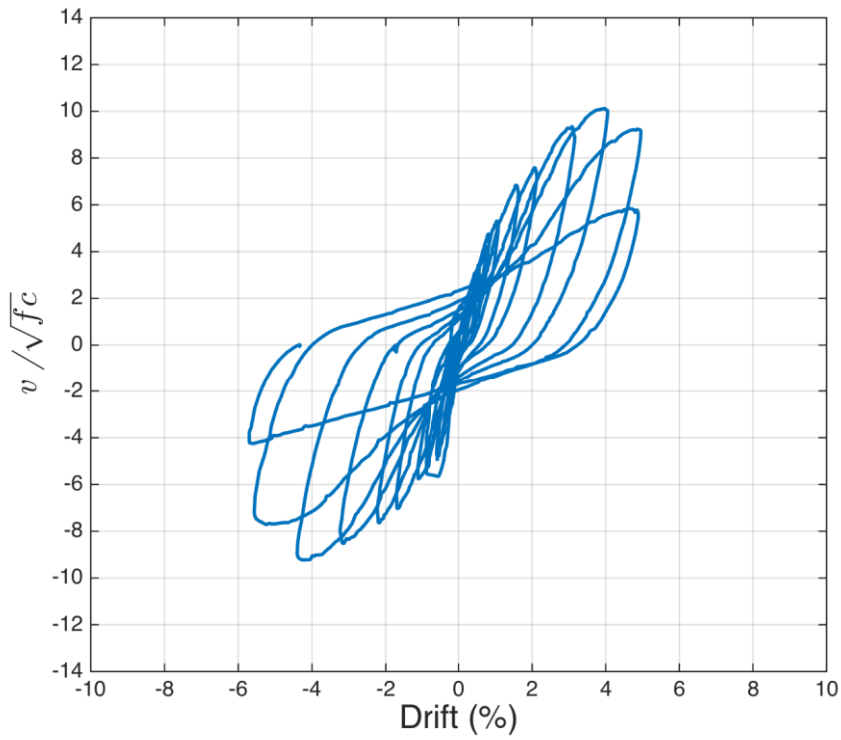


**Figure 4.16: CB7 Hysteresis Response**

Several flexural cracks formed near the ends of the beam during the first few displacement cycles. The formation of diagonal cracks near the mid-region of the beam seemed more pronounced than what was observed for the other specimens. Cracking continued to spread through the beam up to approximately 2.0% drift. At this point the deformations seemed to start localizing near the beam ends and at the lower beam-to-wall interface. A flexural crack near the top end of the beam became noticeable but still remained narrow (0.04 in.). As the displacement demand was further increased up to approximately 5.0% drift, cracking continued to localize in the flexural cracks that formed near the top (see Figure 4.17b) while several flexural cracks joined near the bottom end of the beam to form a horizontal through-depth crack. Once the lateral displacement approached 5.6% drift (negative direction), sliding displacements became significant. At this stage the beam had already lost more than 20% of its peak strength. Maximum estimated elongation of the beam was 0.31 in., which corresponded to an average axial strain of approximately 0.86%.

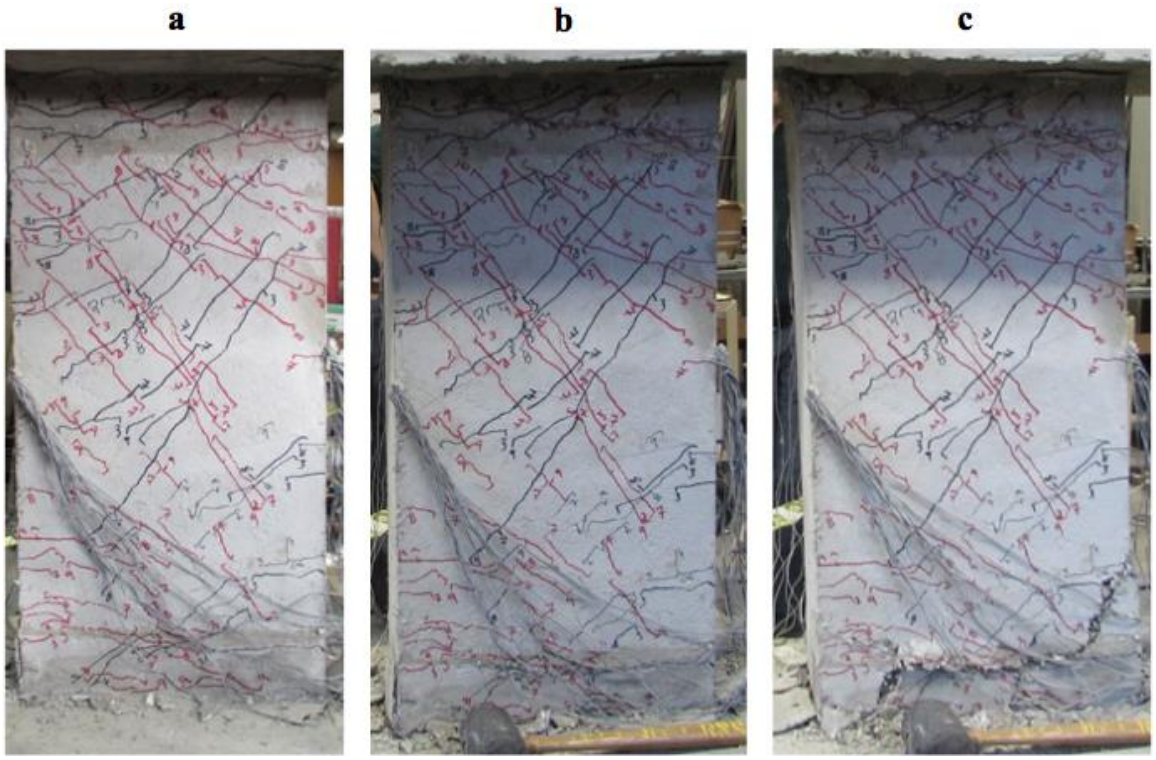


**Figure 4.17: Damage Progression in Specimen CB7, a) -2.2% Drift, b) 5.0% Drift, c) Sliding Failure at -5.7% Drift**

### 4.1.8 Coupling Beam Specimen CB8

Specimen CB8 was nominally identical to Specimen CB7. Axial forces developed throughout the test, however, were adjusted such as to limit the maximum shear stress to $8\sqrt{f'_c}$ (psi). Specimen CB8 exhibited large drift capacity with stable hysteresis, as shown in Figure 4.18. Unlike the rest of the specimens, Specimen CB8 was first loaded in the negative displacement direction. At a 1.5% drift in the positive direction, the applied shear stress was $7.2\sqrt{f'_c}$(psi). In an attempt to keep the shear stresses close to the intended shear demand ($8\sqrt{f'_c}$ [psi]), the bolts connecting the steel links were loosened before applying the 2.0% drift cycle. After the adjustment was made, a reduction in the peak shear stress during the following drift cycle occurred, as expected. However, the beam sustained a peak shear stress of $8.2\sqrt{f'_c}$ (psi) at a drift of approximately 5.1%. The peak axial force developed in the beam, 90 kips ($1.1V_u$), corresponded to an average compressive stress of approximately $0.10f'_c$ based on the gross area of the section. Maximum beam elongation was estimated as 0.27 in., which corresponded to an

average axial strain of approximately 0.75%. Specimen CB8 exhibited a large displacement capacity, approximately 6.2% drift in both directions, while maintaining approximately 90% of its peak strength. When pushed to approximately 7.0% and 8.0% drift in the negative and positive loading direction, respectively, the specimen was able to sustain a shear stress of $6\sqrt{f'_c}$ (psi).

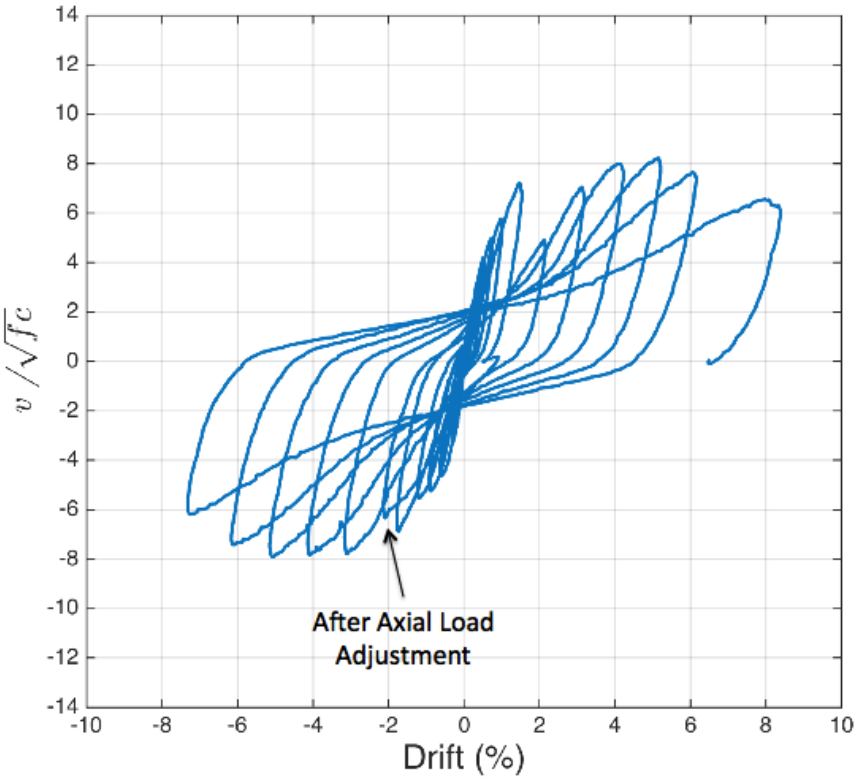


**Figure 4.18: Hysteresis Response of Specimen CB8**

Multiple flexural and diagonal cracks formed during the first few cycles of the test. Cracking continued to spread throughout the beam up to a drift of approximately 2.0%. At a drift of approximately -2.1%, considerable concentrated rotations were observed at both beam ends, as shown in Figure 4.19a. As the applied displacement continued to increase, the cracks near the ends started to grow wider, achieving widths of up to 3/16 in. at a drift of approximately 4.2%. Figure 4.19b shows the accumulated damage near the beam ends at a drift of approximately 5.1%. Notice the horizontal through-depth crack at the bottom plastic hinge and the gap opening between the coupling beam and the support. Progress of damage in Specimen CB8 is shown in Figure 4.20.

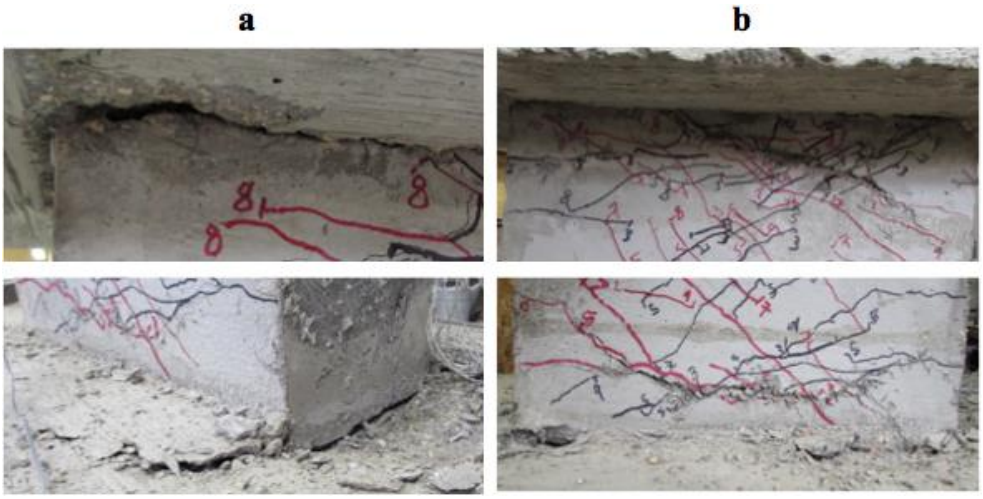


**Figure 4.19: Ends of Coupling Beam CB8, a) Rotation at the Top and Bottom Beam-to-Wall Interface (-2.1% drift), b) Damage at Top and Bottom Ends (5.1% Drift)**

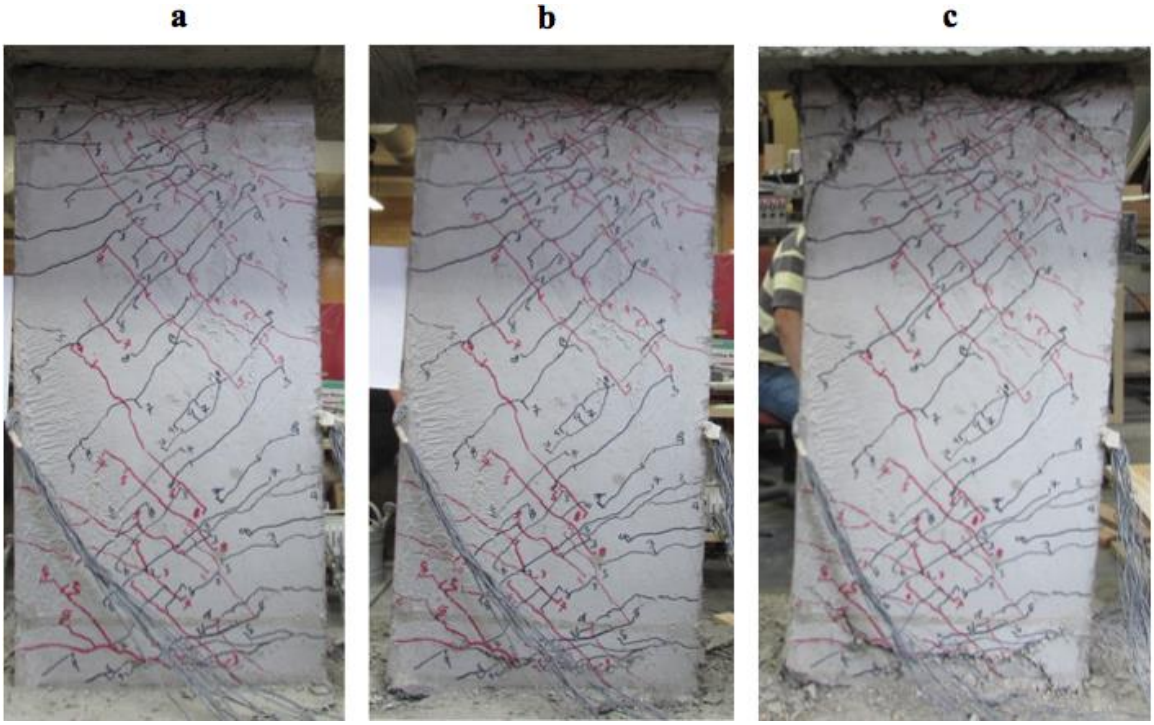


**Figure 4.20: CB8 Damage Progression, a) -2.1% Drift, b) 4.2% Drift, c) Approximately 8.2% Drift**

## 4.2 Estimation of Flexural Strength

Estimating the peak flexural strength of FRC coupling beams with reasonable accuracy is critical, as strength under-predictions would lead to an underestimation of shear demand. Two

critical sections for shear must be considered, at the wall-to-coupling beam interface and at the end of the dowel reinforcement.

The peak flexural strength for each of the test specimens at the wall-to-coupling beam interface was estimated using a plastic section analysis assuming that all reinforcement over the tension half-depth of the beam is stressed at $1.1(f_y)_{\text{measured}}$ and the main compression reinforcement is stressed at $(f_y)_{\text{measured}}$. For cases in which no information is available on actual yield strength, the use of $1.25f_y$ and $f_y$ for the tension and compression steel is recommended, respectively. The compression zone was assumed to be stressed at $0.85f'_c$ over a depth $a$ required for equilibrium of normal forces (including axial force). In the calculation of flexural strength, the peak axial force developed during the tests was used. For design purposes, however, it is recommended that strength calculations be conducted without axial force and with an axial force of $0.1f'_cA_g$. Figure 4.21 shows the assumed stress distribution at the beam ends.

For the section at the end of the dowel reinforcement, flexural strength was estimated with and without the effect of post-cracking tensile strength of FRC. In the latter, the strength calculations are the same as for the end section, except for the absence of dowel reinforcement. For the case of strength calculation including the effect of FRC post-cracking tensile strength, an average of $f_{pc}$ and $\gamma f_{pc}$, obtained from the tension notched prism tests, was used (see Figure 4.22).

Excellent agreement was obtained between the calculated and experimental flexural strength developed at the wall-to-coupling beam interface for all specimens that exhibited a flexurally-dominated response (Specimens CB2 through CB8). Except for Specimen CB4, calculated flexural strength ranged between 91% and 99% of the peak experimental moment. Calculated strength of Specimen CB4 was 108% of the peak strength.

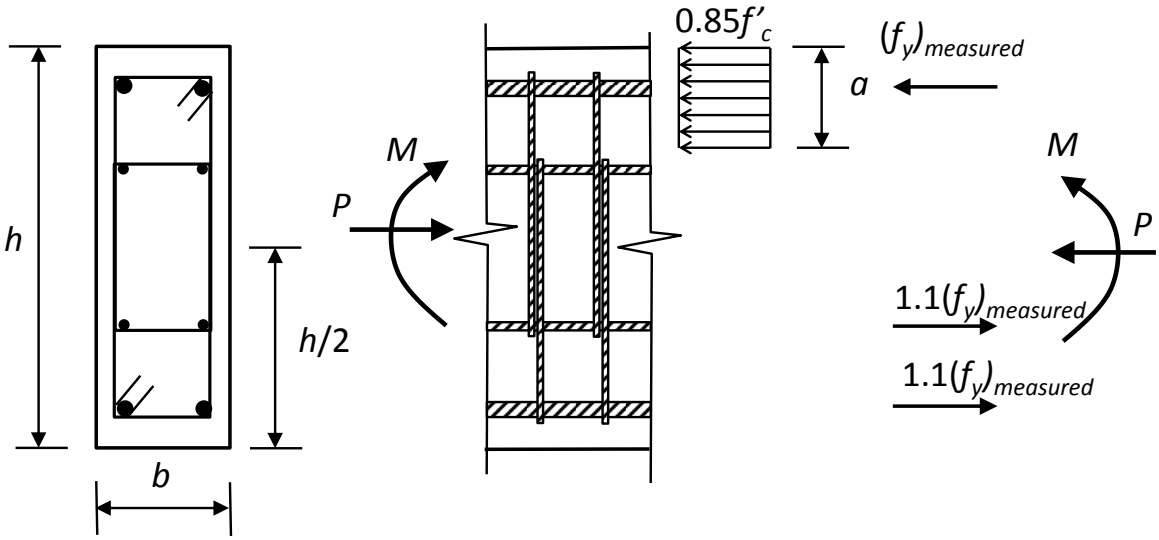


**Figure 4.21: Assumed Stress Distribution for Calculation of Peak Moment Strength (Excluding FRC Post-Cracking Tensile Strength)**

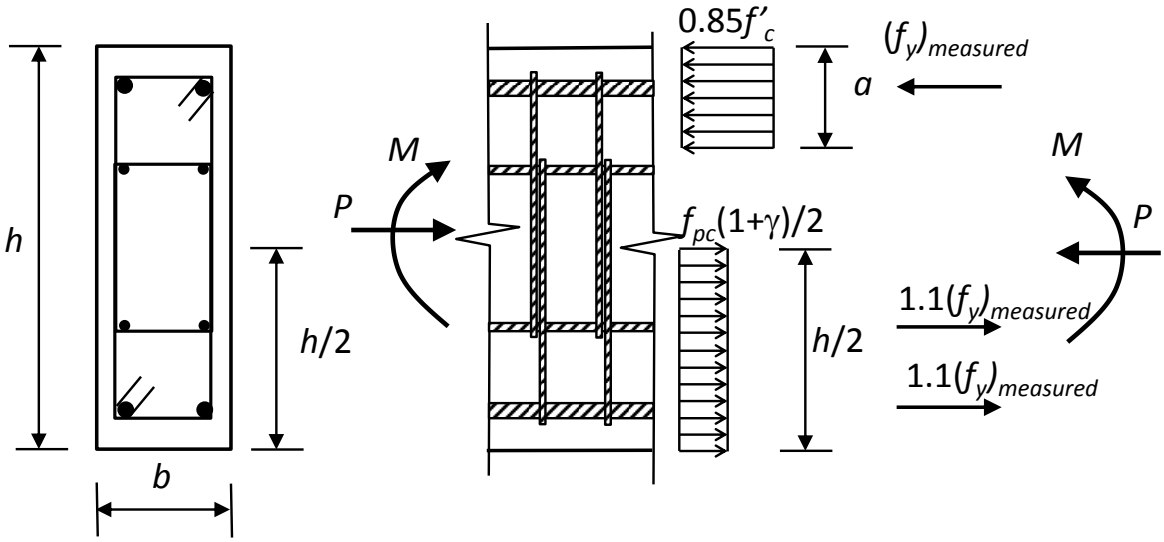


**Figure 4.22: Assumed Stress Distribution for Calculation of Peak Moment Strength (Including FRC Post-Cracking Tensile Strength)**

The calculated flexural strength at the end of the dowel reinforcement, neglecting any contribution from the post-cracking strength of FRC, also agreed very well with the experimental strengths. For Specimens CB5 through CB8, the calculated strength ranged between 97% and 102% of the experimental peak moment at that section. The flexural strength of Specimens CB2 through CB4, on the other hand, ranged between 105% and 112% of the peak experimental moment developed at the ends of the dowels. For Specimens CB2 through CB8, the shear

associated with the calculated flexural strength at the end of the dowels (without fibers) ranged between 102% and 110% of the shear corresponding to the calculated flexural strength at the beam ends. This ratio led to satisfactory spread of plasticity at the end of the coupling beams.

Including an average concrete tensile stress over the half tension depth of the section to account for the post-cracking tensile strength of FRC led in some cases to significant overestimations of flexural strength, particularly for Specimens CB6 through CB8 with a fiber volume fraction of 1.5%. This is not unexpected, however, as the disturbance created by the termination of the dowel reinforcement, combined with the presence of two sets of hoops at the end of the dowels, most likely weakened that section. Further, it is possible that the closely spaced hoop reinforcement at the coupling beam ends led to a tendency for fibers towards a vertical (perpendicular to longitudinal axis) orientation, which would have reduced the post-cracking tensile strength of the FRC in the longitudinal beam direction.

## 4.3 Rotations and Shear Distortions in Plastic Hinge Region

Flexural rotations and shear distortions in the plastic hinge regions were calculated using data from the first two strips at each end of the coupling beams (see Section 2.2.7 for marker and strip layouts). Figure 4.23 through Figure 4.26 show representative rotation and shear distortion responses for coupling beams with $l_n/h$ = 3.0 and 2.0. It should be mentioned that shear distortions include the effect of sliding displacements that developed towards the end of the tests, which substantially increased the calculated shear strain.

The plastic hinges developed a stable flexural behavior, with rotations in some cases exceeding 0.06 rad. Damage at such large rotations, however, was extensive, which included crushing of the concrete cover and even deterioration in part of the concrete core. Shear distortions, on the other hand, were relatively small prior to the initiation of sliding shear (in general, less than 0.0075 rad). As sliding occurred, the calculated shear distortions increased significantly and the hysteresis exhibited severe “pinching”, as expected given the absence of diagonal reinforcement.

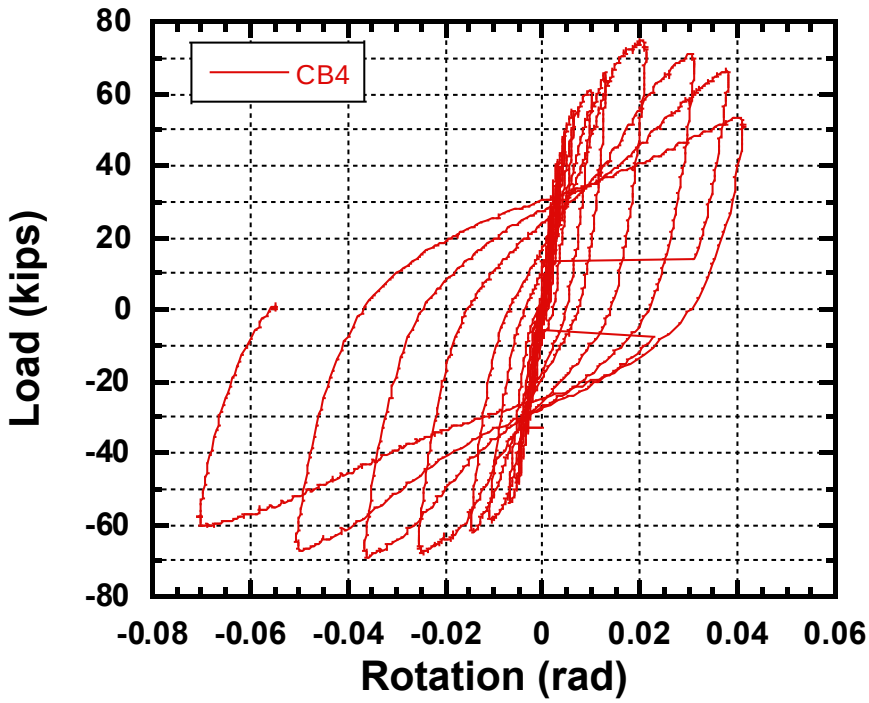


**Figure 4.23: Plastic Hinge Rotation Response (Specimen CB4)**

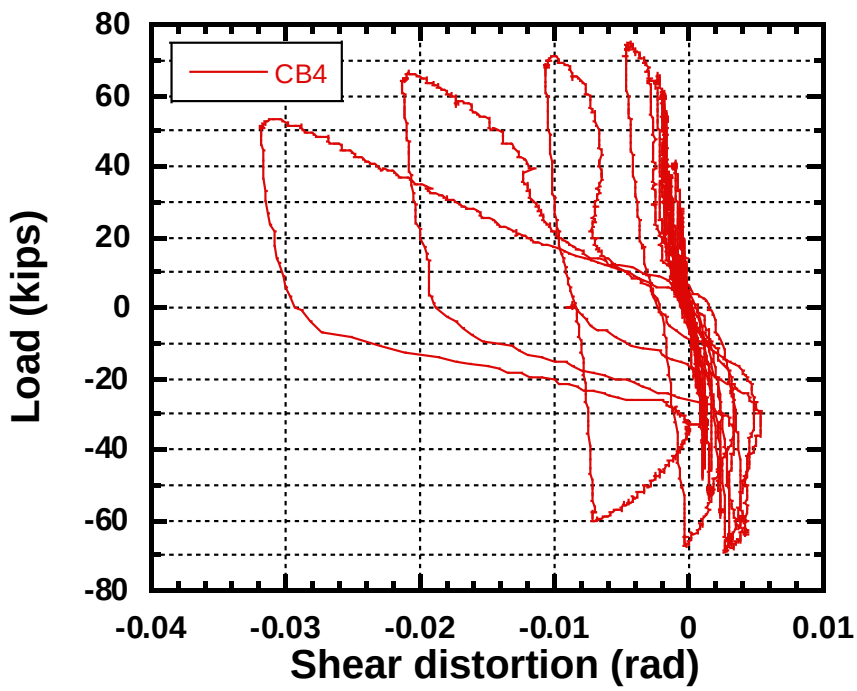


**Figure 4.24: Plastic Hinge Shear Distortion Response (Specimens CB4)**

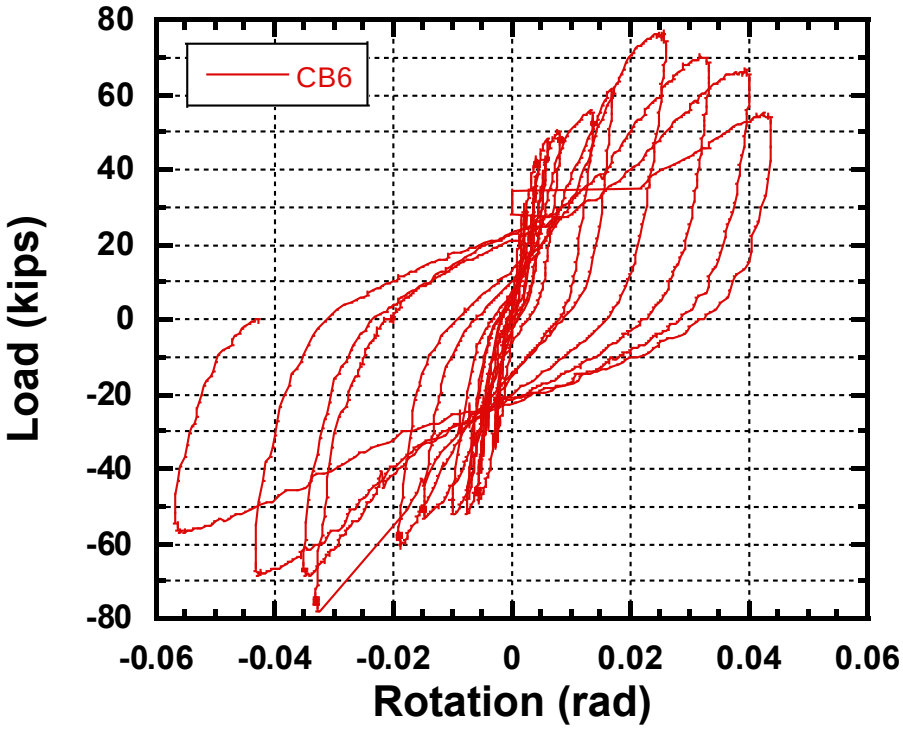


**Figure 4.25: Plastic Hinge Rotation Response (Specimens CB6)**

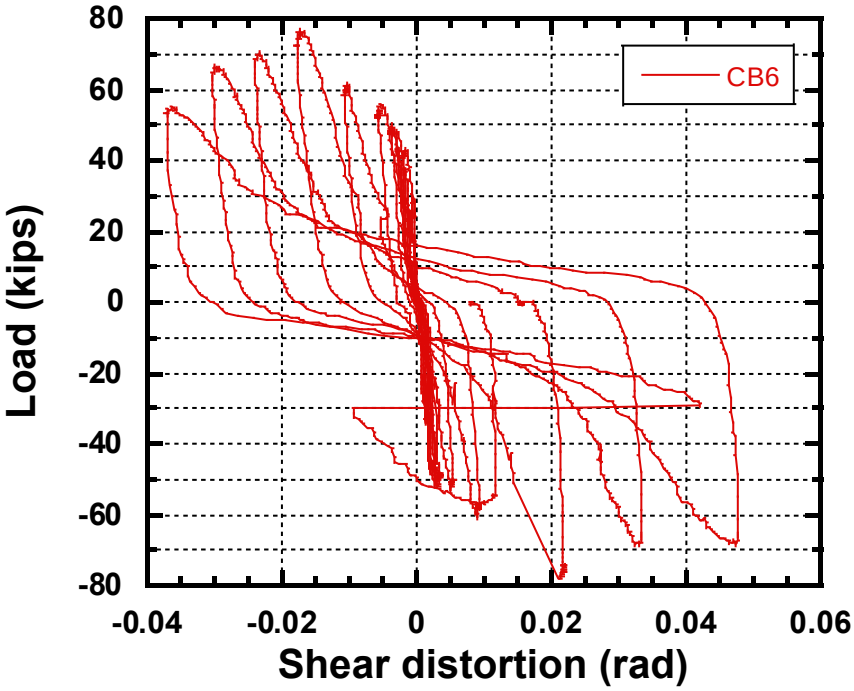


**Figure 4.26: Plastic Hinge Shear Distortion Response (Specimens CB6)**

## 4.4 Drift Components Analysis

In order to have a better understanding of the behavior of the FRC coupling beams, the relative contributions of flexural and shear deformations to the overall applied drift were investigated. Based on the curvatures and shear distortions calculated for each marker strip on the beams (see Section 2.2.7 for marker and strip layouts), the lateral displacement due to curvatures and shear distortions were estimated. The lateral displacement due to flexural deformations was calculated using the moment-area method. The first moment of the areas under the curvature diagram was calculated with respect to both beam ends and the average tangential deviation was taken as the lateral displacement resulting from the curvature distribution at the specific drift under consideration. At a given drift level, the tangential deviation $\delta_f$ was calculated as,

$$\delta_f = \sum [\phi_i \, (h_s)_i \, \bar{x}_i] \tag{18}$$

where $\phi_i$ is the curvature of the $i^{th}$ strip, $(h_s)_i$ is the average height of the $i^{th}$ strip, and $\bar{x}_i$ is the distance from the centroid of the $i^{th}$ strip to the beam end considered. It should be noted that curvatures corresponding to the last strip at each beam end include the effect of concentrated rotations at the beam-to-wall interface caused by the accumulation of strains in the steel reinforcement inside the end blocks.

Lateral displacement due to shear deformations, $\delta_v$, was estimated using the average shear distortion for each marker strip as follows,

$$\delta_v = \sum [(\gamma_s)_i \, (h_s)_i \,] \tag{19}$$

where $(\gamma_s)_i$ is the average shear distortion of the $i^{th}$ strip for the drift under consideration. No distinction was made between shear sliding and displacements due to actual shear distortions on the beam. Instead, both effects were lumped into shear distortion contributions.

Figure 4.27 through Figure 4.34 show the relative contributions to the applied drifts of flexural and shear deformations for each of the coupling beam specimens.

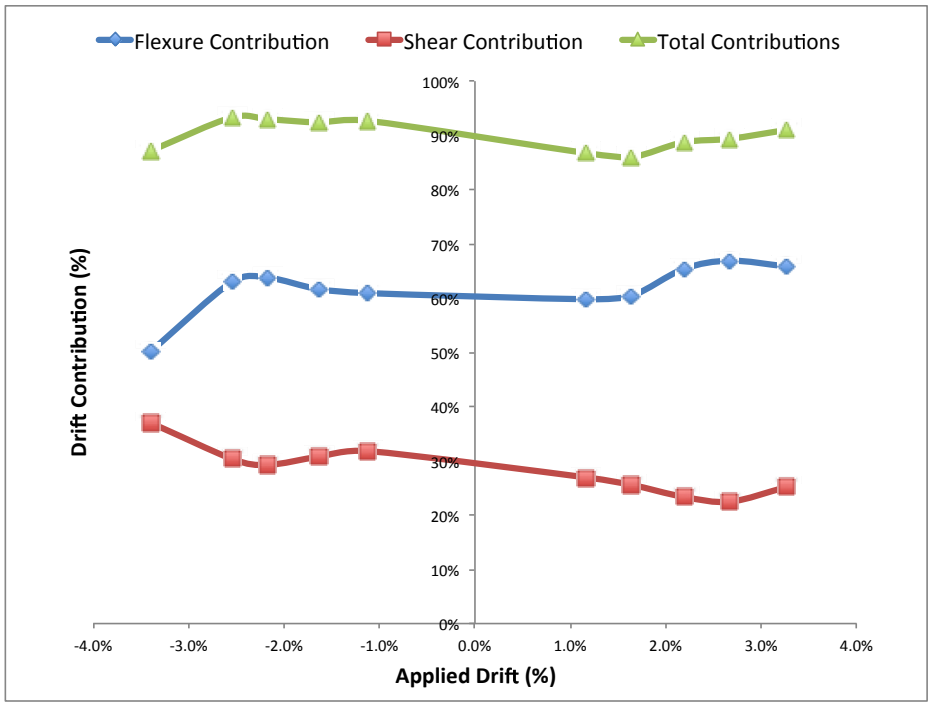


**Figure 4.27: Relative Contributions to Drift (CB1)**

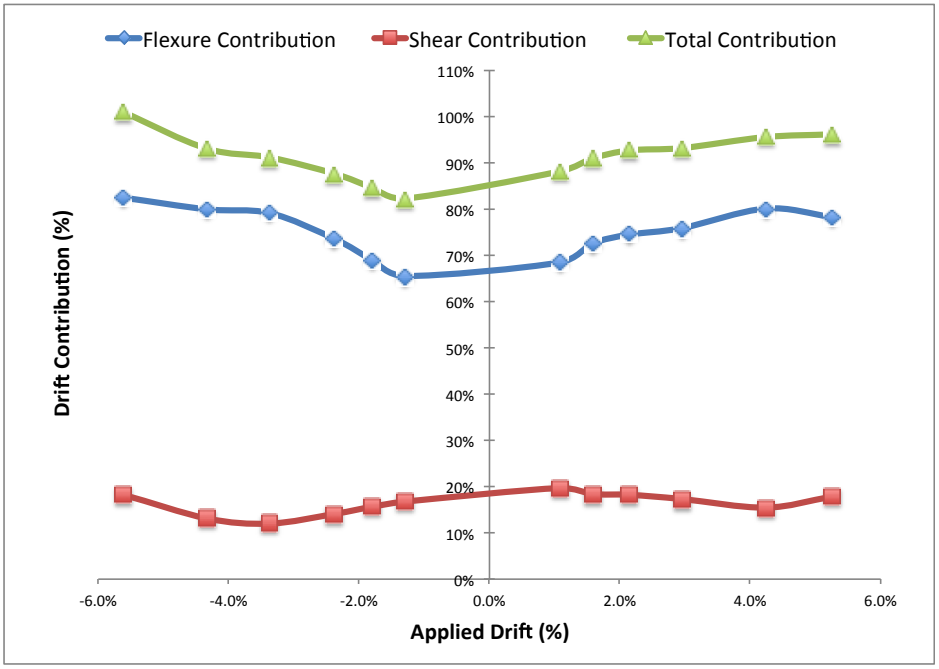


**Figure 4.28: Relative Contributions to Drift (CB2)**

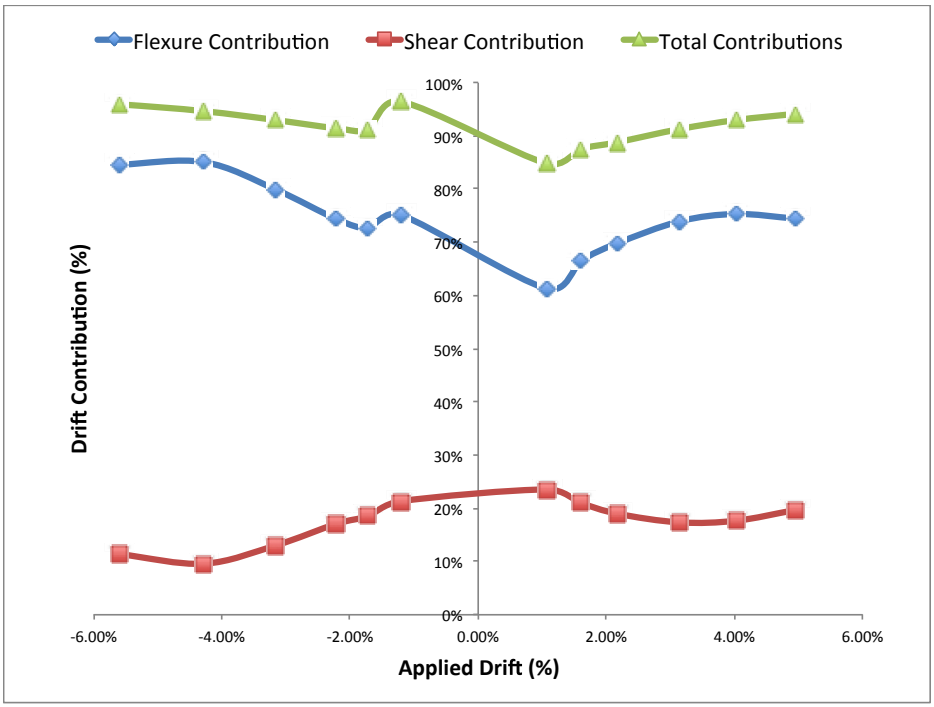


**Figure 4.29: Relative Contributions to Drift (CB3)**

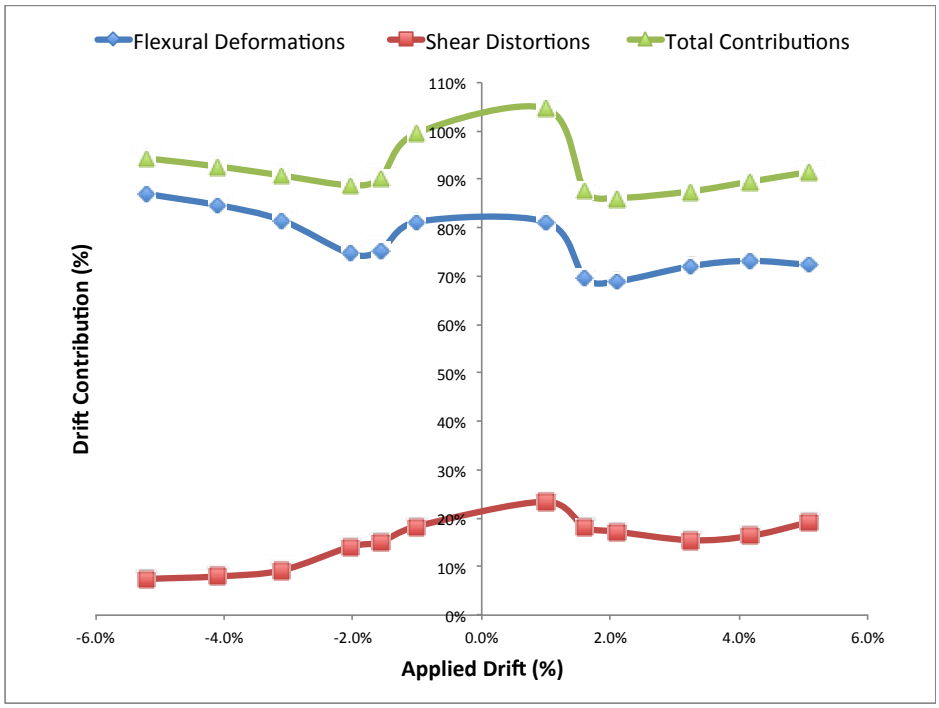


**Figure 4.30: Relative Contributions to Drift (CB4)**

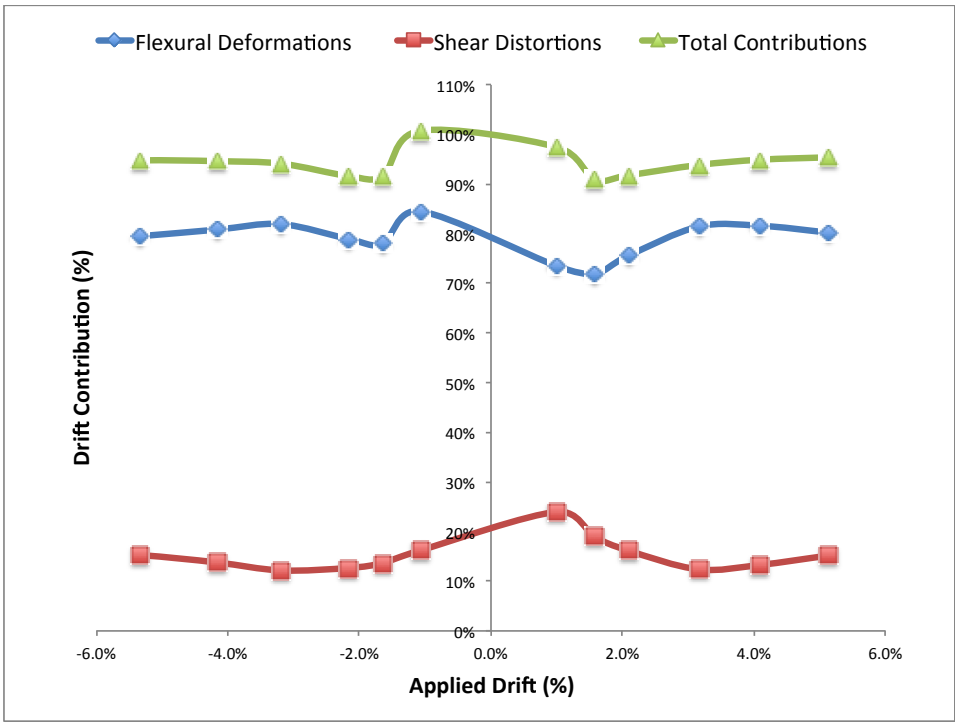


**Figure 4.31: Relative Contributions to Drift (CB5)**

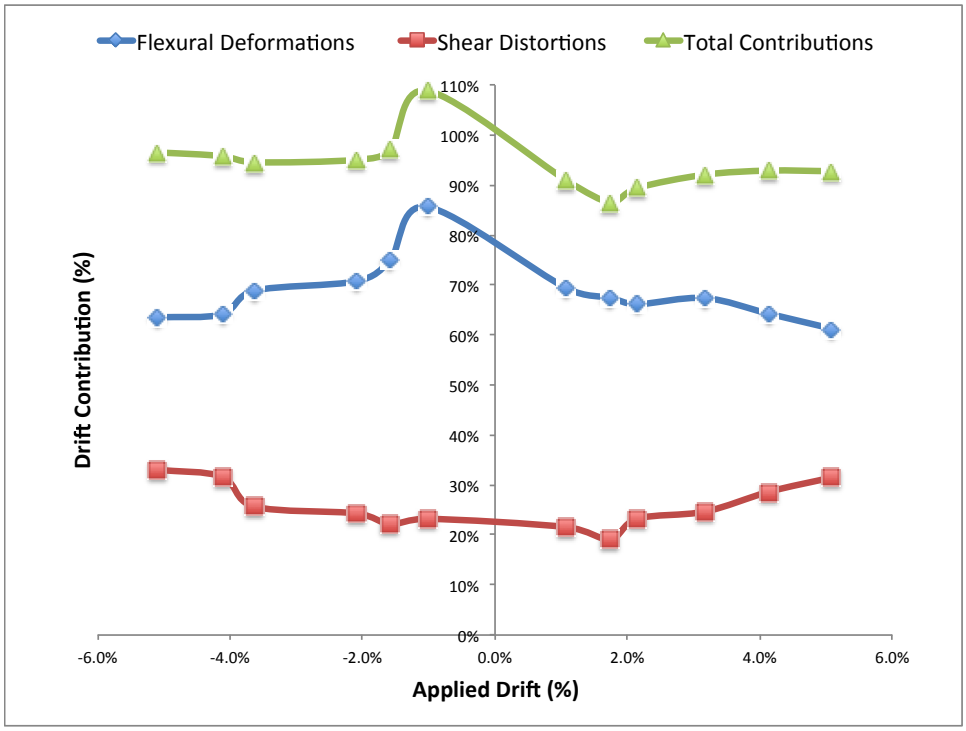


**Figure 4.32: Relative Contributions to Drift (CB6)**

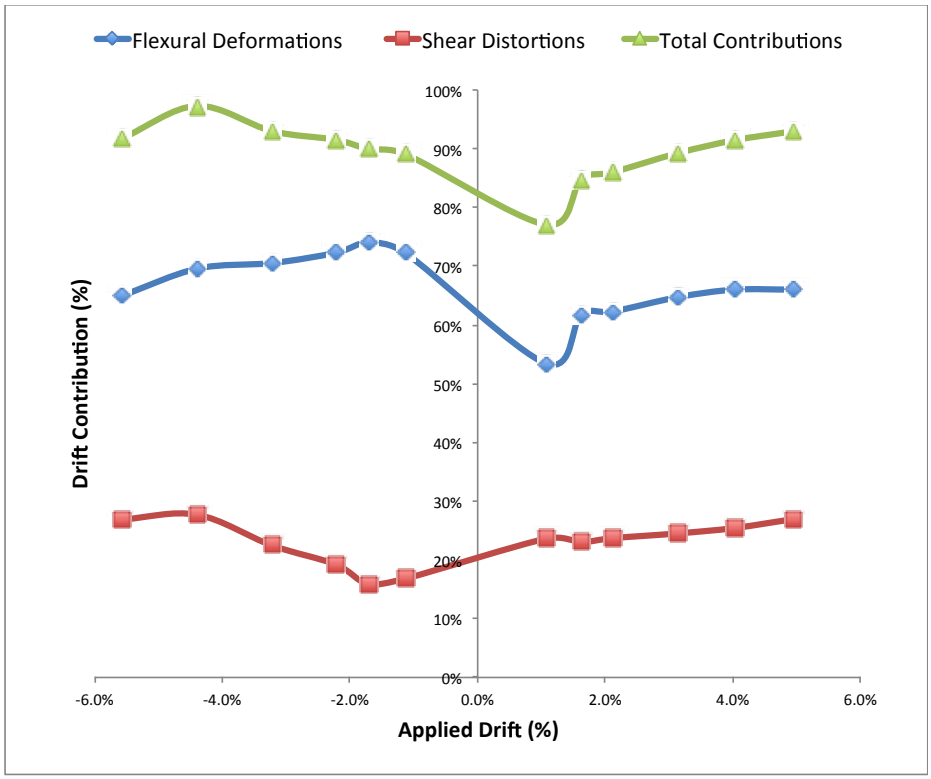


**Figure 4.33: Relative Contributions to Drift (CB7)**

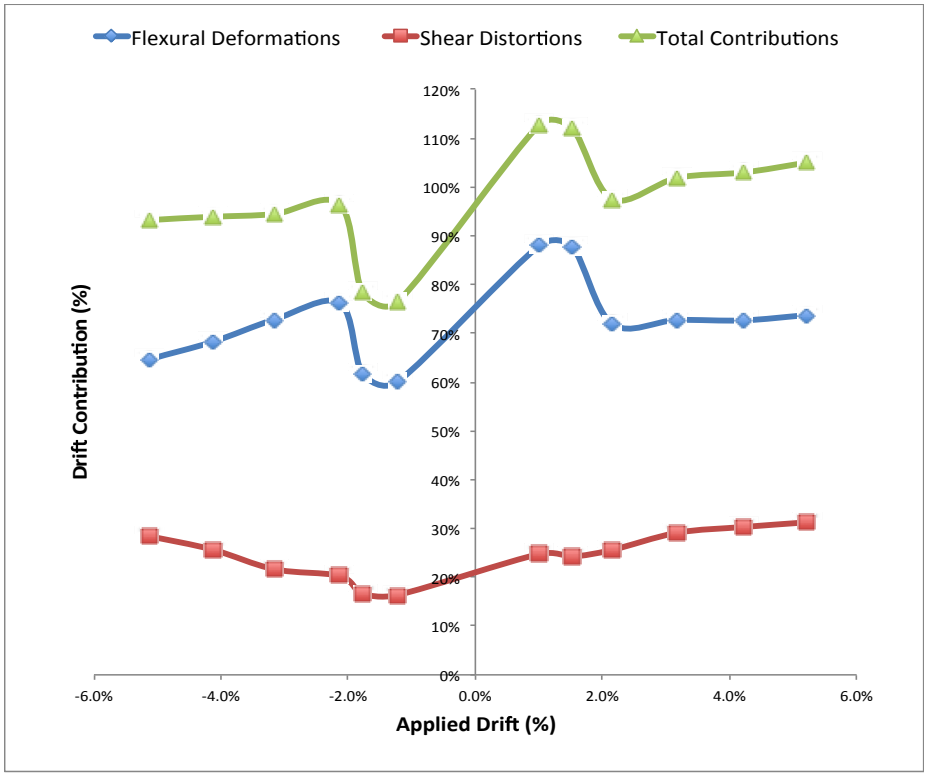


**Figure 4.34: Relative Contributions to Drift (CB8)**

Table 4.2 summarizes the relative contributions of flexural and shear deformations to the applied drift for each coupling beam specimen. The contributions shown represent the average contribution for the different drifts levels applied to the specimen. In general, calculated drifts ranged between 85% and 110% of the actual drift.

Clearly, drift contributions from flexural deformations were significantly greater than those from shear deformations, especially in specimens with $l_n/h = 3.0$ (except for Specimen CB1). Contributions from flexural deformations were largest (approximately 75-80%) in Specimens CB2 through CB5 with $l_n/h = 3.0$. Shear contribution to total drift was, as expected, greater (approximately 25-30%) in Specimens CB6 through CB8 with $l_n/h = 2.0$ compared to Specimens CB2 through CB5 with $l_n/h = 3.0$ (15-20%). The largest contribution from shear deformations to drift occurred in Specimen CB1, with $l_n/h = 3.0$ and a peak shear stress of $12.2\sqrt{f'_c}$ (psi), reaching nearly 40% at the end of the test.

The high contributions of flexural deformations to the applied drift indicate a flexurally-dominated behavior of the FRC coupling beams. Although shear deformations had a higher contribution for the coupling beams with $l_n/h = 2.0$, flexural deformations were still the major deformation mechanism.

**Table 4.2: Average Relative Contributions of Flexural and Shear Deformations to Applied Drift**

| | Contribution to Drift | | |
|---|---|---|---|
| Specimen | Flexure | Shear | Total |
| CB1 | 62% | 28% | 90% |
| CB2 | 75% | 16% | 91% |
| CB3 | 74% | 17% | 92% |
| CB4 | 77% | 15% | 92% |
| CB5 | 79% | 15% | 94% |
| CB6 | 69% | 26% | 94% |
| CB7 | 67% | 23% | 90% |
| CB8 | 73% | 25% | 98% |

## 4.5 Reinforcement Strains

### 4.5.1 Transverse Reinforcement

The behavior of the transverse reinforcement at various locations along the beam length was monitored through strain gauges. In all beams, transverse reinforcement in the middle beam region (i.e., outside of plastic hinge regions) consisted of single #3 hoops at a spacing $s$ of either 4 in. ($l_n/h$ = 3.0) or 3.25 in. ($l_n/h$ = 2.0). The shear strength contributed by these hoops, $V_s$, was estimated assuming a truss analogy with a longitudinal projection of the diagonal crack equal to 15.5 in. (approximately 85% of the overall member depth) for all specimens. Based on this, the shear force "demand" on the fiber reinforced concrete, $V_c$, was estimated for each coupling beam specimen as the difference between the peak applied shear and $V_s$ calculated assuming the hoops reached their measured yield strength. Table 4.3 shows the peak applied average shear stress for each specimen, $v_u$, along with the calculated shear stress contribution from the transverse reinforcement, $v_s$, and the calculated shear stress demand on the FRC, $v_c$. All stresses were calculated based on the gross cross-sectional area.

As shown in Table 4.3, the calculated shear stress demand in the concrete, $v_c$, for the specimens with $l_n/h$ = 3.0 did not exceed $4\sqrt{f'_c}$ (psi), except for Specimen CB1, for which the calculated $v_c$ was $6.2\sqrt{f_c'}$ (psi). Figure 4.35 and Figure 4.36 show the hoop strains measured at peak positive displacement for the cycles at 3.0% and 5.0% drifts at various locations along the span for Specimens CB2 through CB5 ($l_n/h$ = 3.0). As can be seen, strains in the middle hoops for Specimens CB2 through CB5 were below 0.003 and 0.0035 for drifts of up to 3.0% and 5.0%, respectively. This is consistent with the minor damage observed in the middle region of the coupling beams at the end of the tests. In contrast to this behavior, the hoops in Specimen CB1 started yielding during the cycle at 2.0% drift, with strains exceeding 0.02 during the cycle at 3.0% drift. As discussed earlier, this specimen exhibited a shear failure during the cycle at 4.0% drift.

The middle hoops in the specimens with $l_n/h$ = 2.0 (Specimens CB6 through CB8), exhibited lower strains compared to those in the specimens with $l_n/h$ = 3.0 with a maximum strain at 5.0% drift of 0.0018. This was expected given the lower shear stress demands imposed on the concrete

for these three specimens (Table 4.3), combined with the higher performance exhibited by the FRCs with $V_f$ = 1.5%.

Strains in the transverse reinforcement at the beam ends were generally lower than those in the middle hoops, which indicate that the amount provided of transverse confinement reinforcement was adequate. The exception was one of the end hoops in Specimens CB2 and CB3, which yielded during the cycle at 4.0% drift. Figure 4.37 shows the response for the yielding end hoop in Specimen CB2.

**Table 4.3: Calculated Shear Strength provided by Transverse Reinforcement and FRC**

| Specimen | $f'_c$ (psi) | Fibers Type - $V_f$ | $v_u$ ($\sqrt{f'_c}$, psi) | $v_s^*$ ($\sqrt{f'_c}$, psi) | $v_c$ ($\sqrt{f'_c}$, psi) |
|---|---|---|---|---|---|
| CB1 | 7930 | HE 55/35 – 1.25% | 12.2 | 6.0 | 6.2 |
| CB2 | 8840 | HE 55/35 – 1.25% | 9.9 | 5.8 | 4.1 |
| CB3 | 8630 | RC 55/30 BG – 1.25% | 9.5 | 5.9 | 3.6 |
| CB4 | 9260 | RC 55/30 BG – 1.0% | 7.2 | 5.9 | 1.3 |
| CB5* | 9750 | RC 80/30 BP – 1.0% | 7.8 | 5.4 | 2.4 |
| CB6* | 7950 | HE 55/35 – 1.5% | 8.1 | 8.1 | 0 |
| CB7 | 9330 | RC 80/30 BP – 1.5% | 10.1 | 7.0 | 3.1 |
| CB8 | 8490 | RC 80/30 BP – 1.5% | 8.2 | 7.3 | 0.9 |

* Calculated using Eq. 1 and measured yield strength

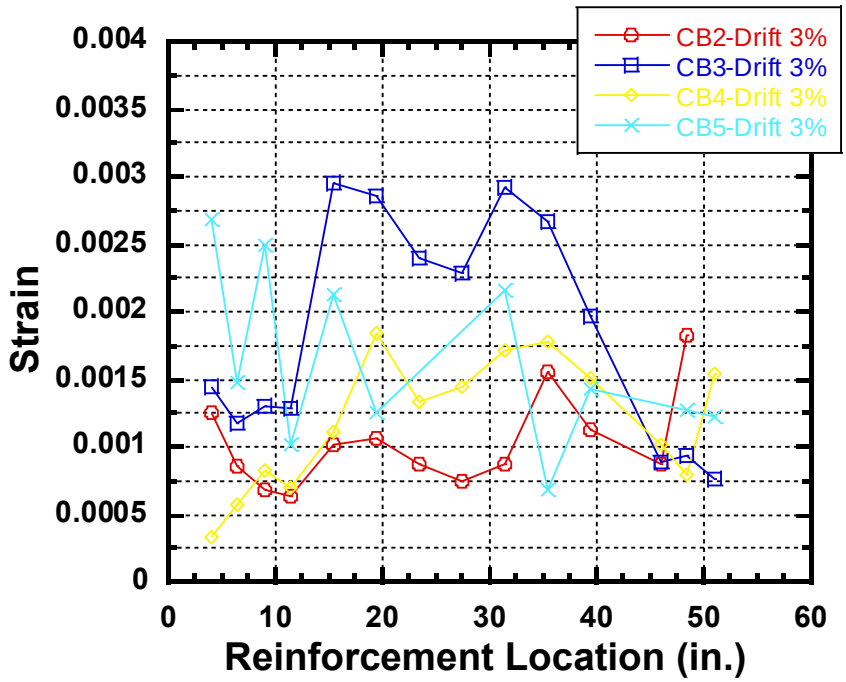


**Figure 4.35: Measured Hoop Strains at Peak Positive Displacement for 3.0% Drift Cycle**

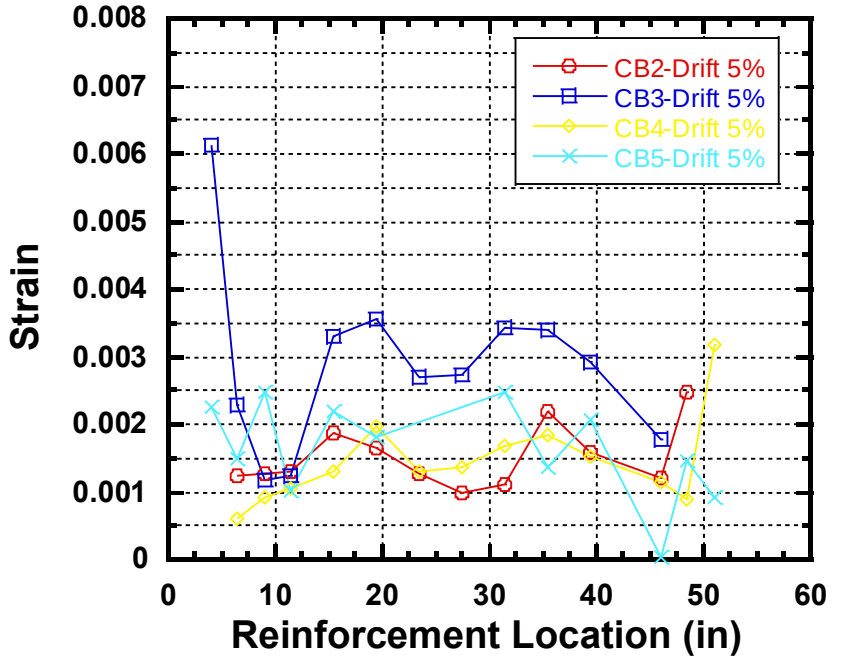


**Figure 4.36: Measured Hoop Strains at Peak Positive Displacement for 5.0% Drift Cycle**

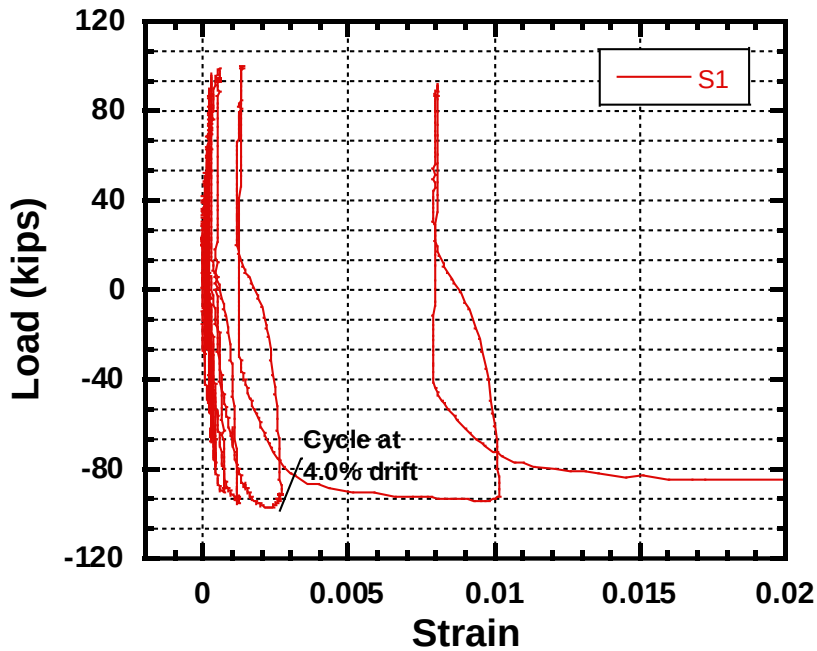


**Figure 4.37: Response of End Hoop in Specimen CB2**

### 4.5.2 Longitudinal and Dowel Reinforcement

Strain gauge measurements at the beam ends indicated that yielding of the top and bottom longitudinal reinforcement started during the cycles between 0.5% and 0.75% drift (Figure 4.38 and Figure 4.39, respectively). Soon after, yielding was also detected at approximately half the beam depth from the wall faces for Coupling Beams CB1 through CB5 with $l_n/h$ = 3.0 (Figure 4.40 and Figure 4.41) and at the end of the dowel reinforcement in Specimens CB6 through CB8 (no strain gauges were placed at half the beam depth from the wall faces for these three specimens). During the cycles to 3.0%, 4.0% and 5.0% drift, the longitudinal reinforcement reached very large strains at the beam ends, exceeding in some cases 0.04. As discussed earlier, fracture of longitudinal reinforcement was observed in Specimen CB5. It should be noted that in a few instances, as shown in Figure 4.38, the hysteresis strain response of the flexural reinforcement consisted of nearly symmetrical loops towards the very end of the test, indicating that the reinforcement had become the main source of normal force transfer in the compression zone. This was the case where a significant gap opening occurred at the beam-to-wall interface which did not close upon reversal of the displacement, severe concrete degradation took place, or both.

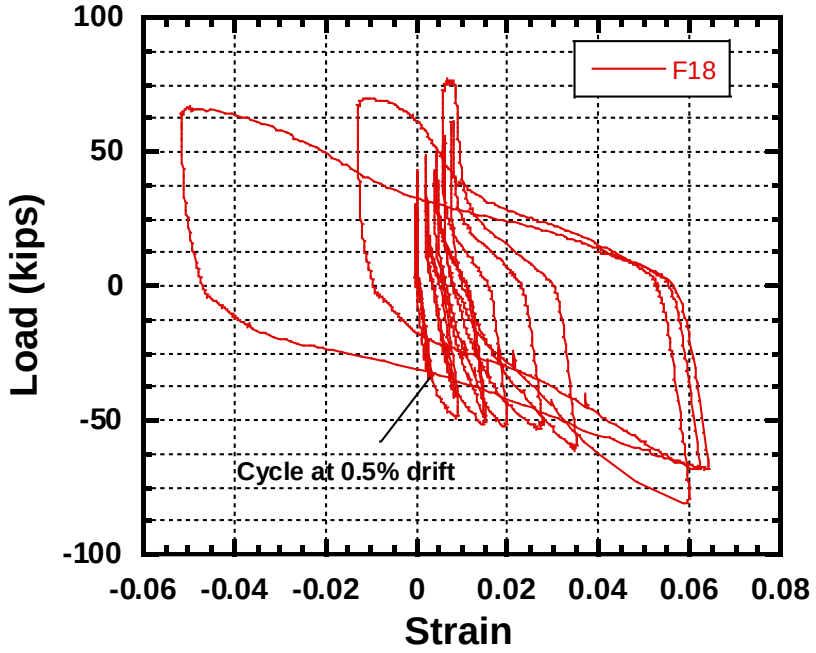


**Figure 4.38: Response of Main Flexural Reinforcement at Beam-to-Wall Connection (Specimen CB6)**

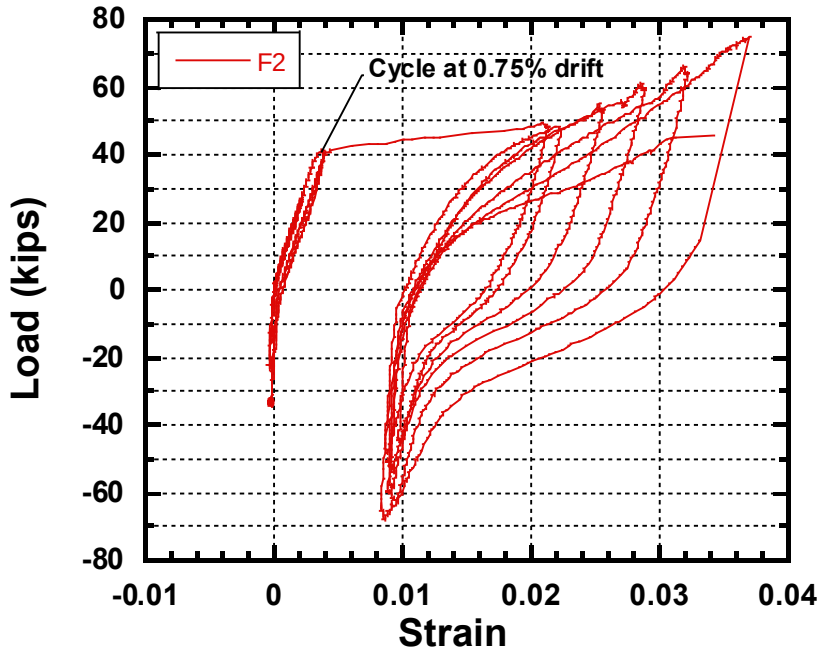


**Figure 4.39: Response of Main Flexural Reinforcement at Beam-to-Wall Connection (Specimen CB4)**

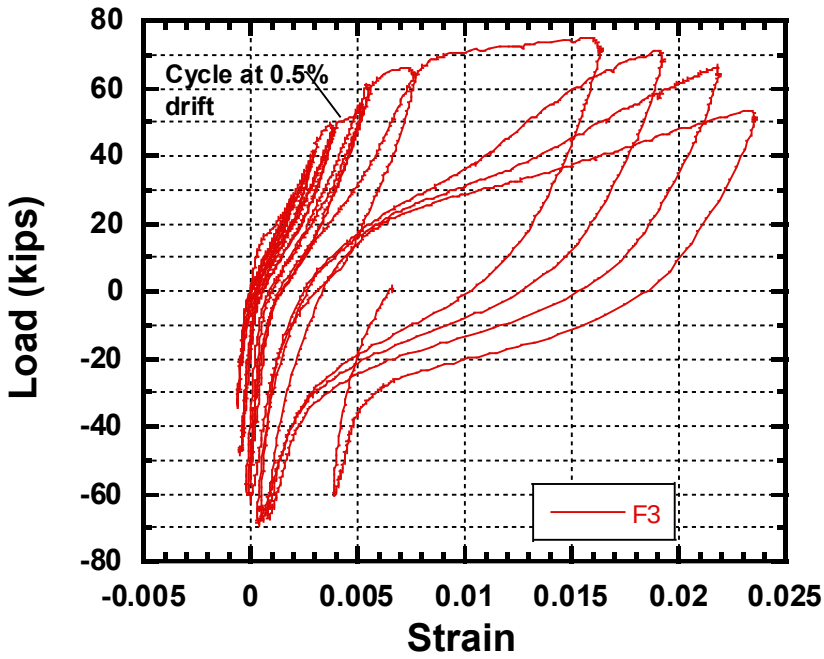


**Figure 4.40: Response of Main Flexural Reinforcement at Approximately *h*/2 from Wall Face (Specimen CB4)**

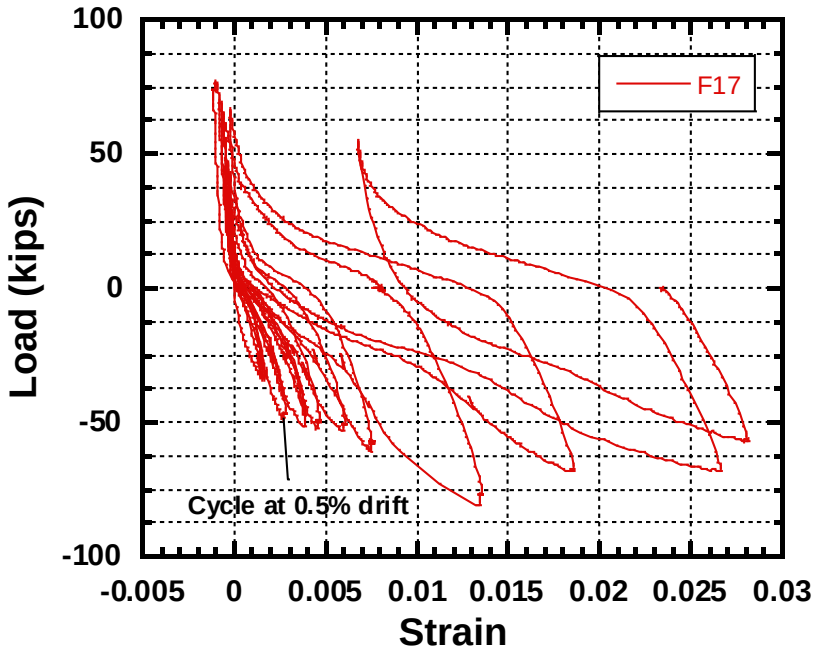


**Figure 4.41: Response of Main Flexural Reinforcement near Termination of Dowels (Specimen CB6)**

Strains gauges placed on the U-shaped dowel reinforcement at the coupling beam-to-wall interface indicated yielding of this reinforcement during displacement cycles at 2.0% drift or greater. The short extension of these dowels into the coupling beams (9 bar diameters for

Specimens CB2 through CB5, and 6 bar diameters for Specimens CB6 through CB8, measured from the wall faces) was thus adequate to strengthen this interface and contribute to the spreading of flexural yielding.

## 4.6 Link between Material Properties and Structural Performance of Coupling Beams

In order to establish a link between material behavior and coupling beam performance in terms of peak shear stress and drift capacity, the FRCs investigated in this project were lumped into three classes. Class 1 FRC represents a material with a hardening behavior under direct tension. Thus, of all the FRCs investigated, only those with a 1.5% volume fraction of RC 80/30 BP fibers would qualify as a Class 1 FRC. Class 2 and Class 3 FRCs, both strain-softening materials, are meant to represent materials such as that used in Specimen CB2 (HE 55/35 fibers at $V_f$ = 1.25%) and Specimen CB5 (RC 80/30 BP fibers at $V_f$ = 1.0%), respectively.

Given the difficulties associated with conducting direct tensile tests, and based on the good correlation between the tensile behavior obtained indirectly from the behavior of un-notched beams and that obtained from direct tensile tests (see Section 3.4), performance criteria based on the results from four-point bending tests of 6 x 6 x 18 in. un-notched beams are proposed to classify the FRCs as Class 1, Class 2 and Class 3 as shown below. In the performance criteria below, stresses correspond to equivalent bending stresses and $L$ is the span length of the un-notched beam.

- Class 1 FRC:
    - Peak post-cracking strength greater than or equal to 1.2 times the first cracking strength *and* greater than or equal to $12\sqrt{f_c}$ (psi).
    - Residual strength at mid-span deflection of $L/150$ greater than or equal to 0.4 times the peak post-cracking strength.

- Class 2 FRC:

- Peak post-cracking strength greater than or equal to the first cracking strength *and* greater than or equal to $9\sqrt{f_c}$ (psi).
- Residual strength at mid-span deflection of $L/150$ greater than or equal to 0.4 times the peak post-cracking strength.

- Class 3 FRC:
  - Peak post-cracking strength greater than or equal to 0.8 times the first cracking strength *and* greater than or equal to $7.5\sqrt{f_c}$ (psi).
  - Residual strength at mid-span deflection of $L/150$ greater than or equal to 0.4 times the peak post-cracking strength.

Based on the performance of the test coupling beams, relationships between peak shear stress and span-to-depth ratio are proposed corresponding to an estimated 6.0% drift capacity for coupling beams constructed with each of the three classes of FRC and the proposed reinforcement detailing (Figure 4.42). Class 1 FRCs can be used for coupling beams with $l_n/h \geq 2.0$. Class 2 and Class 3 FRCs, however, are only recommended for use in coupling beams with $l_n/h \geq 3.0$. Along with the peak shear stress limits, limits are also imposed on the calculated shear stress demand on the FRC in the middle portion of the beam, $v_c$, calculated as discussed in Section 4.5.1.

Data points in Figure 4.42 correspond to the test results for Specimens CB2 through CB5, and Specimens CB7 and CB8, as well as test specimens with span-to-depth ratio of 2.2, 2.75 and 3.3 reported in Parra-Montesinos et al. (2014), which were constructed with a material that qualifies as Class 1 FRC. Data for Specimen CB1 were excluded as the shear stress demand on the FRC for this specimen exceeded the specified limit of $4\sqrt{f'_c}$ (psi). On the other hand, Specimen CB6 was excluded because that specimen had an $l_n/h = 2.0$, but the material used does not qualify as a Class 1 FRC.

It should be noted that some test specimens exhibited a drift capacity less than 6.0%. In all cases but one, however, the peak shear stress in those specimens was greater than the recommended shear stress limit. An attempt was thus made to estimate the drift capacity based on the

recommended shear stress limit (i.e., a slightly higher drift capacity was assumed for cases in which the proposed shear stress limit was less than the experimental peak shear stress). The exception to this was a specimen with $l_n/h$ = 2.75 reported in Parra-Montesinos et al. (2014), which exhibited a drift capacity of 5.8% for a peak shear stress slightly less than the maximum recommended for $l_n/h$ = 2.75 ($9\sqrt{f_c}$ [psi]). Given the additional data corresponding to Specimens with $l_n/h$ < 2.75 and $l_n/h$ = 3.0, and the closeness of the shear stress-drift capacity point for this particular specimen to the proposed limit, the proposed performance criteria for Class 1 FRC are believed to be acceptable.

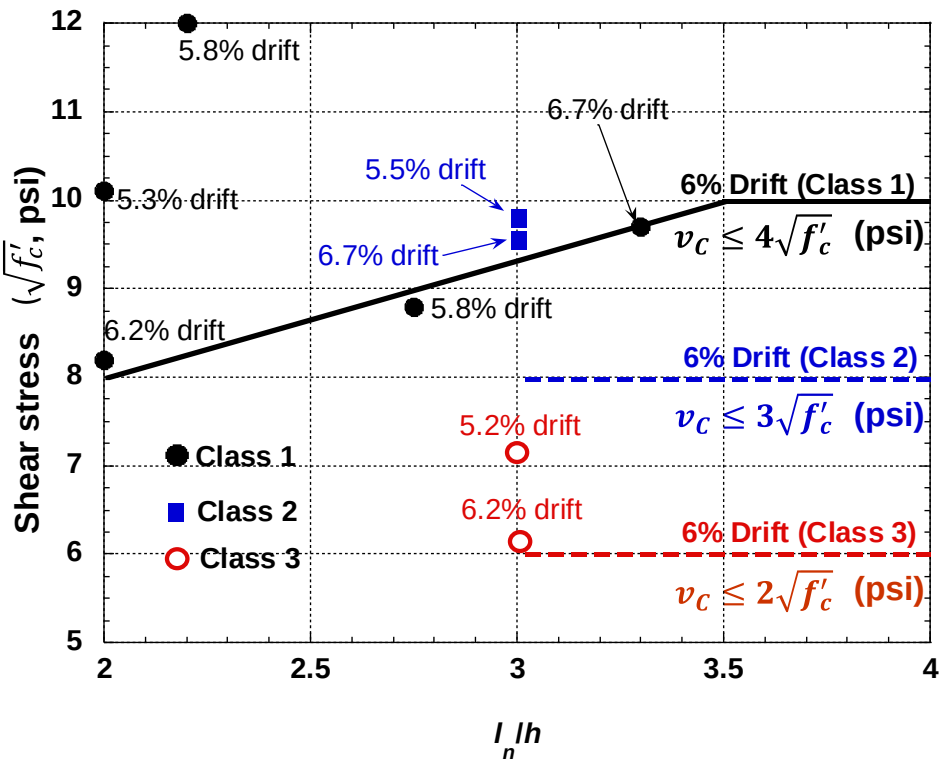


**Figure 4.42: Recommended Shear Stress-Drift Limits for Class 1, Class 2 and Class 3 FRCs**

# 5 Summary and Conclusions

## 5.1 Summary

The experimental study discussed herein was aimed at evaluating the seismic performance of fiber reinforced concrete (FRC) coupling beams without diagonal reinforcement, constructed using a simplified reinforcement detailing compared to that resulting from the application of provisions in ACI 318-14. For this purpose, eight large-scale, precast coupling beam specimens were tested under large displacement reversals. Five of the specimens had a span-to-depth ratio of 3.0 and were designed for peak average shear stresses ranging from 7 to $12\sqrt{f'_c}$ (psi). The remaining three specimens had a span-to-depth ratio of 2.0 and were designed for a target shear stress demand of approximately 8-$10\sqrt{f'_c}$ (psi).

Three types of hooked steel fibers (based on fiber geometry and tensile strength) and three different fiber volume fractions (1.0%, 1.25% and 1.5%) were considered in this study for a total of six FRC mixtures evaluated. In order to establish a link between the mechanical properties of the FRCs to the structural performance of the coupling beams, a series of material tests was also conducted. The flexural, tensile and compressive behavior of the different FRCs used in the coupling beam specimens was evaluated through bending tests of notched and un-notched beams, direct tension tests on notched prisms, and cylinder compression tests.

## 5.2 Conclusions

The following conclusions are based on the observations and results obtained from the coupling beam tests as well as the FRC material tests.

- In general, FRC coupling beams with an $l_n/h \geq 2.0$ can achieve drift capacities of at least 5.0% and exhibit stable, flexurally-dominated behavior when subjected to large displacement reversals with peak shear stresses ranging from 6 to $10\sqrt{f'_c}$ (psi). The behavior of all the FRC coupling beams but Specimen CB1 was heavily controlled by flexural deformations, which contributed approximately 70-80% to the total applied drift. At approximately 4.0% drift, flexural cracks at the beam ends corresponding to both

loading directions joined to form through-depth cracks near the termination of the dowel reinforcement. These through cracks allowed significant shear sliding to occur and led to failure of the coupling beams during subsequent drift cycles.

- The use of RC 80/30BP fibers at a 1.5% volume fraction resulted in a hardening behavior under direct tension and pronounced deflection hardening under four-point bending (in both un-notched and notched beams). A material with such behavior, classified as Class 1 FRC in Section 4.6, is required to achieve 6.0% drift capacity in coupling beams with $l_n/h$ between 2.0 and 3.0 and shear stresses not greater than 8 and 10 $\sqrt{f'_c}$ (psi), respectively.
- Coupling beams constructed with FRC materials exhibiting softening behavior under direct tension (see Class 2 and Class 3 FRCs in Section 4.6) and with $l_n/h \geq 3.0$ may achieve a drift capacity of 6.0% depending on the shear stress demand. For materials with tensile and bending behavior similar to that of the FRC used in Specimen CB2 (HE 35/55 fibers at a 1.25% volume fraction), classified as Class 2 FRC in Section 4.6, a 6.0% drift capacity can be achieved when shear stresses are limited to $8\sqrt{f'_c}$ (psi). For materials with behavior similar to that of the FRC used in Specimen CB5 (RC 80/30 BP fibers at a 1.0% volume fraction), classified as Class 3 FRC in Section 4.6, a 6.0% drift capacity can be achieved when shear stresses are limited to $6\sqrt{f'_c}$ (psi). Until further experimental data become available, these materials are not recommended for use in coupling beams without diagonal reinforcement and with $l_n/h < 3.0$.
- Transverse confinement reinforcement requirements in ACI 318-14 for potential plastic hinge regions of columns in Special Moment Frames are adequate for confinement of the end regions of FRC coupling beams, over a length of half the beam depth from the wall faces. Transverse reinforcement in the middle region of FRC coupling beams, on the other hand, must be designed such that the expected shear stresses to be resisted by the FRC material (referred to herein as $v_c$) do not exceed 4, 3 and $2\sqrt{f'_c}$ (psi) for Class 1, Class 2 and Class 3 FRC, respectively.
- Two critical sections must be considered for calculation of flexural strength, the coupling beam-to-wall interface and the section at the termination of the dowel reinforcement. Expected flexural capacity can be estimated based on the use of a plastic stress

distribution assuming all reinforcement over the tension half of the beam depth reaches a stress of 1.1 times the measured yield strength or 1.25 times the nominal yield strength (see Section 4.2). It is recommended that the contribution of the fiber reinforcement to flexural strength at the termination of the dowels be ignored. It is also recommended that strength calculations be conducted without axial force and with an axial force of $0.10f'_cA_g$.

- For adequate spread of plasticity, dowel reinforcement (in addition to intermediate longitudinal reinforcement) must be designed such that the shear associated with the expected flexural strength (calculated as discussed in previous conclusion; see Section 4.2) at the end of the dowels ranges between approximately 1.0 and 1.1 times the shear corresponding to the expected flexural strength at the beam ends. The use of U-shaped dowel reinforcement with embedded lengths of 9 and 6 bar diameters from the wall faces proved effective in contributing to flexural strength at the beam-to-wall interface and to good spread of plasticity in coupling beams with $l_n/h$ of 3.0 and 2.0, respectively.

# 6 References


ACI Committee 318 (2014).*"Building Code Requirements for Structural Concrete (ACI318-14)"*, American Concrete Institute, Farmington Hills, MI.

ASTM A370. (2014). *"Standard Test Methods and Definitions for Mechanical Testing of Steel Products,"* American Society for Testing and Materials, 1–50.

ASTM C1609. (2005). *"Standard Test Method for Flexural Performance of Fiber-Reinforced Concrete (Using Beam With Third-Point Loading),"* American Society for Testing and Materials, 1–8.

ASTM C39. (2016). *"Standard Test Method for Compressive Strength of Cylindrical Concrete Specimens,"* American Society for Testing and Materials, 1–7.

Canbolat, A., Parra-Montesinos, G., and Wight J.K., (2005). *"Experimental Study on Seismic Behavior of High-Performance Fiber-Reinforced Cement Composite Coupling Beams,"* ACI Structural Journal, 102 (1), 159-166.

Kopczynski, C., and Whiteley, M., (2016). *"Lincoln Square Expansion. Steel Fiber Reinforced Concrete Solves Seismic Design Challenge,"* Structure Magazine, March 2016, 42-44.

Lequesne, R. (2011).*"Behavior and Design of High-Performance Fiber-Reinforced Concrete Coupling Beams and Coupled-Wall Systems,"* Ph.D. dissertation, The University Of Michigan, Ann Arbor, MI.

Lequesne, R., Parra-Montesinos, G.J., and Wight, J.K. (2013). "*Seismic Behavior and Detailing of High-Performance Fiber-Reinforced Concrete Coupling Beams and Coupled Wall Systems,"* J. Struct. Eng., ASCE, 139 (8), 1362-1370.

NDI Measurement Sciences (2010). *"First Principles User Guide"*, Northern Digital Inc., Waterloo, Ontario, Canada.

NDI Measurement Sciences (2011). *"Optotrak Certus User Guide"*, Northern Digital Inc., Waterloo, Ontario, Canada.

Paulay, T. (1971). *"Coupling Beams of Reinforced Concrete Shear Walls,"* Journal of the Structural Division, Proceedings ASCE. 97 (ST3), 843-861.

Paulay, T., and Binney, J.R., (1974). *"Diagonally Reinforced Coupling Beams of Shear Walls,"* Shear in Reinforced Concrete, ACI Publication SP-42, 579- 598

Paulay, T. and Santhakumar, A.R. (1976). *"Ductile Behavior of Coupled Shear Walls,"* Journal of the Structural Division, Proceedings ASCE, 102 (ST1), 99-108.

Parra-Montesinos, G.J., Wight, J.K., Kopczynski, C., Lequesne, R., Setkit, M., Conforti, A. and Ferzli, J. (2014). *"High-Performance Fiber Reinforced Concrete Coupling Beams: From Research To Practice"*, Tenth U.S. National Conference on Earthquake Engineering, Anchorage, AK.

Setkit, M. (2012).*"Seismic Behavior of Slender Coupling Beams Constructed with High-Performance Fiber-Reinforced Concrete,"* Ph.D. dissertation, The University Of Michigan, Ann Arbor, MI.

# 7 Appendix A

## Table A1: Test dates for material samples and coupling beam specimens

| CB Test Date | Coupling Beam | Fiber Type | Fiber Volume Fract. | Tension Blocks | | | Notched Beams | | | Un-notched Beams | | | Cylinders | | |
|---|---|---|---|---|---|---|---|---|---|---|---|---|---|---|---|
| | | | | ID | Test Date | Age (days) | ID | Test Date | Age (days) | ID | Test Date | Age (days) | ID | Test Date | Age (days) |
| 3/31/2015 | CB1 | HE 55/35 | 1.25% | CB1T1 | 4/3/2015 | 51 | CB1-NB1 | 4/7/2015 | 55 | CB1B1 | 4/7/2015 | 55 | CB1CYLN1 | 3/31/2015 | 48 |
| | | HE 55/35 | 1.25% | CB1T2 | 4/3/2015 | 51 | CB1-NB2 | 4/7/2015 | 55 | CB1B2 | 4/7/2015 | 55 | CB1CYLN2 | 4/8/2015 | 56 |
| | | HE 55/36 | 1.25% | CB1T3 | 4/3/2015 | 51 | | | | CB1B3 | 4/7/2015 | 55 | CB1CYLN3 | 4/8/2015 | 56 |
| | | HE 55/35 | 1.25% | CB1T4 | 4/3/2015 | 51 | | | | | | | CB1CYLN4 | 4/8/2015 | 56 |
| 5/22/2015 | CB2 | HE 55/35 | 1.25% | CB2T1 | 6/25/2015 | 62 | CB2-NB1 | 6/2/2015 | 39 | CB2B1 | 6/1/2015 | 38 | CB2CYLN1 | 5/22/2015 | 28 |
| | | HE 55/35 | 1.25% | CB2T2 | 6/25/2015 | 62 | CB2-NB2 | 6/2/2015 | 39 | CB2B2 | 6/1/2015 | 38 | CB2CYLN2 | 5/22/2015 | 28 |
| | | HE 55/36 | 1.25% | CB2T3 | 6/25/2015 | 62 | | | | CB2B3 | 6/1/2015 | 38 | CB2CYLN3 | 5/29/2015 | 35 |
| | | HE 55/35 | 1.25% | CB2T4 | 6/25/2015 | 62 | | | | CB2B4 | 6/2/2015 | 39 | CB2CYLN4 | 5/29/2015 | 35 |
| | | HE 55/35 | 1.25% | | | | | | | | | | CB2CYLN5 | 5/29/2015 | 35 |
| 7/7/2015 | CB3 | ZP305 55/30 | 1.25% | CB3T1 | 7/14/2015 | 35 | CB3-NB1-Batch2 | 7/8/2015 | 29 | CB3-B1-Batch2 | 7/8/2015 | 29 | CB3CYLN1 | 7/7/2015 | 28 |
| | | ZP305 55/30 | 1.25% | CB3T2 | 7/14/2015 | 35 | CB3-NB2-Batch3 | 7/8/2015 | 29 | CB3-B2-Batch3 | 7/8/2015 | 29 | CB3CYLN2 | 7/7/2015 | 28 |
| | | ZP305 55/30 | 1.25% | CB3T3 | 7/14/2015 | 35 | CB3-NB3-Batch3 | 7/8/2015 | 29 | CB3-B3-Batch3 | 7/9/2015 | 30 | CB3CYLN3 | 7/7/2015 | 28 |
| | | ZP305 55/30 | 1.25% | CB3T4 | 7/14/2015 | 35 | | | | CB3-B4-Batch3 | 7/9/2015 | 30 | CB3CYLN4 | 7/7/2015 | 28 |
| | | ZP305 55/30 | 1.25% | | | | | | | CB3-B5-Batch1 | 7/9/2015 | 30 | CB3CYLN5 | 7/7/2015 | 28 |
| 8/7/2015 | CB4 | ZP305 55/30 | 1.00% | CB4T1 | 8/10/2015 | 31 | CB4-NB1-Batch2 | 8/11/2015 | 32 | CB4-B1-Batch1 | 8/11/2015 | 32 | CB4-CYLN1-B1 | 8/7/2015 | 28 |
| | | ZP305 55/30 | 1.00% | CB4T2 | 8/10/2015 | 31 | CB4-NB2-Batch3 | 8/11/2015 | 32 | CB4-B2-Batch2 | 8/11/2015 | 32 | CB4-CYLN2-B2 | 8/7/2015 | 28 |
| | | ZP305 55/30 | 1.00% | CB4T3 | 8/10/2015 | 31 | CB4-NB3-Batch3 | 8/11/2015 | 32 | CB4-B3-Batch3 | 8/11/2015 | 32 | CB4-CYLN1-B1 | 8/12/2015 | 33 |
| | | ZP305 55/30 | 1.00% | CB4T4 | 8/10/2015 | 31 | | | | CB4-B4-Batch3 | 8/11/2015 | 32 | CB4-CYLN2-B2 | 8/12/2015 | 33 |
| | | ZP305 55/30 | 1.00% | | | | | | | CB4-B5-Batch3 | 8/11/2015 | 32 | CB4-CYLN5-B3 | 8/12/2015 | 33 |
| 10/5/2015 | CB5 | 80/30BP | 1.00% | CB5T1 | 11/3/2015 | 60 | CB5-NB1-Batch2 | 10/12/2015 | 38 | CB5-B1-Batch1 | 10/9/2015 | 35 | CB5CYLN1 | 10/6/2015 | 32 |
| | | 80/30BP | 1.00% | CB5T2 | 11/4/2015 | 60 | CB5-NB2-Batch3 | 10/12/2015 | 38 | CB5-B2-Batch2 | 10/9/2015 | 35 | CB5CYLN2 | 10/6/2015 | 32 |
| | | 80/30BP | 1.00% | CB5T3 | 11/5/2015 | 60 | CB5-NB3-Batch3 | 10/12/2015 | 38 | CB5-B3-Batch3 | 10/9/2015 | 35 | CB5CYLN3 | 10/16/2015 | 42 |
| | | 80/30BP | 1.00% | CB5T4 | 11/6/2015 | 60 | CB5-NB4-Batch3 | 10/12/2015 | 38 | CB5-B4-Batch3 | 10/9/2015 | 35 | CB5CYLN4 | 10/16/2015 | 42 |
| | | 80/30BP | 1.00% | | | | | | | | | | CB5CYLN5 | 10/16/2015 | 42 |
| 11/30/2015 | CB6 | HE 55/35 | 1.50% | CB6T1 | 12/16/2015 | 47 | CB6-NB1-Batch1 | 2/17/2016 | 110 | CB6-B1-Batch1 | 6/2/2016 | 216 | CB6CYLN1 | 11/30/2015 | 31 |
| | | HE 55/35 | 1.50% | CB6T2 | 12/17/2015 | 47 | CB6-NB2-Batch2 | 2/17/2016 | 110 | CB6-B2-Batch2 | 6/2/2016 | 216 | CB6CYLN2 | 12/1/2015 | 32 |
| | | HE 55/36 | 1.50% | CB6T3 | 12/18/2015 | 47 | CB6-NB3-Batch3 | 2/17/2016 | 110 | CB6-B3-Batch3 | 6/2/2016 | 216 | CB6CYLN3 | 12/1/2015 | 32 |
| | | HE 55/35 | 1.50% | CB6T4 | 12/19/2015 | 47 | CB6-NB4-Batch3 | 2/17/2016 | 110 | CB6-B4-Batch3 | 6/2/2016 | 216 | CB6CYLN4 | 1/22/2016 | 84 |
| | | HE 55/35 | 1.50% | | | | | | | | | | CB6CYLN5 | 1/22/2016 | 84 |
| 2/12/2016 | CB7 | 80/30BP | 1.50% | CB7T1 | 2/29/2016 | 77 | CB7-NB1-Batch1 | 6/3/2016 | 172 | CB7-B1-Batch1 | 6/2/2016 | 171 | CB7CYLN1 | 2/12/2016 | 60 |
| | | 80/30BP | 1.50% | CB7T2 | 2/29/2016 | 77 | CB7-NB2-Batch2 | 6/3/2016 | 172 | CB7-B2-Batch2 | 6/2/2016 | 171 | CB7CYLN2 | 2/12/2016 | 60 |
| | | 80/30BP | 1.50% | CB7T3 | 2/29/2016 | 77 | CB7-NB3-Batch3 | 6/3/2016 | 172 | CB7-B3-Batch3 | 6/2/2016 | 171 | CB7CYLN3 | 6/8/2016 | 177 |
| | | 80/30BP | 1.50% | CB7T4 | 2/29/2016 | 77 | CB7-NB4-Batch3 | 6/3/2016 | 172 | CB7-B4-Batch3 | 6/2/2016 | 171 | CB7CYLN4 | 6/8/2016 | 177 |
| | | 80/30BP | 1.50% | | | | | | | | | | CB7CYLN5 | 6/8/2016 | 177 |
| 6/7/2016 | CB8 | 80/30BP | 1.50% | CB8T1 | 6/10/2016 | 45 | CB8-NB1-Batch1 | 6/8/2016 | 43 | CB8-B1-Batch1 | 6/9/2016 | 44 | CB8CYLN1 | 6/7/2016 | 42 |
| | | 80/30BP | 1.50% | CB8T2 | 6/10/2016 | 45 | CB8-NB2-Batch2 | 6/8/2016 | 43 | CB8-B2-Batch2 | 6/9/2016 | 44 | CB8CYLN2 | 6/7/2016 | 42 |
| | | 80/30BP | 1.50% | CB8T3 | 6/11/2016 | 45 | CB8-NB3-Batch3 | 6/8/2016 | 43 | CB8-B3-Batch3 | 6/9/2016 | 44 | CB8CYLN3 | 6/10/2016 | 45 |
| | | 80/30BP | 1.50% | CB8T4 | 6/12/2016 | 45 | CB8-NB4-Batch3 | 6/8/2016 | 43 | CB8-B4-Batch3 | 6/9/2016 | 44 | CB8CYLN4 | 6/10/2016 | 45 |
| | | 80/30BP | 1.50% | | | | | | | | | | CB8CYLN5 | 6/10/2016 | 45 |